NORTHWESTERN UNIVERSITY

Phenomenological and Numerical Studies of Helium II Dynamics in the Two-Fluid Model

A DISSERTATION

SUBMITTED TO THE GRADUATE SCHOOL
IN PARTIAL FULFILLMENT OF THE REQUIREMENTS

for the degree

DOCTOR OF PHILOSOPHY

Field of Mechanical Engineering

By

Christine Marie-Therese Darve

EVANSTON, ILLINOIS

December 2011

ABSTRACT

Phenomenological and Numerical Studies of Helium II Dynamics in the Two-Fluid Model

Christine Darve

Understanding superfluidity is of paramount importance to generate low-temperature environments capable of supporting superconductivity. Today, numerous scientific and technical fields make use of high-field superconducting magnets and superconducting RF cavities cooled by Helium II. Experimental observation of the normal component of velocity distribution in a Helium II thermal counterflow can be done using the Particle Image Velocimetry (PIV) technique. The development of our 3-D numerical model for Helium II was specifically motivated by the need to understand and model the experimental results, e.g. results obtained by PIV technique.

The *Landau-Khalatnikov* two-fluid model and the mutual friction mechanism of Gorter-Mellink are very successful phenomenological representations of the properties of Helium II. We used them as a basis to develop a set of approximate partial differential equations (PDE) for the superfluid flow. The form sought was that of a general vector PDE, where in particular pressure and temperature, the main drivers of the flow, appear as explicit state variables. In the case of interest here, i.e. heating induced flow and forced flow conditions, this interaction between two fluids has been described by simple expression of a power law dependence on their relative velocity. The numerical integration of the resulting PDE was implemented in the context of a general class of finite element approximations augmented with a finite difference algorithm with upwind scheme to stabilize the solution.

To reduce the computational complexity to a practical level, several approximations have been made, while ensuring that the resulting code is both complete and consistent. The software that we have developed can be run on a simple computer with reasonable computing time, and allows modeling a wide range of actual cryogenic situations with transient and steady-state heat transfer in Helium II. Examples are ranging from simulations of Helium II behavior as diverse as the second sound propagation, the thermal counterflow or the existence of large eddy structures based on the Gorter-Mellink mutual friction.

ACKNOWLEDGMENTS

First of all, I would like to express my deepest gratitude to my advisor, Professor N. A. Patankar for his patience and precious guidance. Without his support the completion of this work would have never been achieved. Indeed, this research work was conducted in parallel to my job assignments as a cryogenic engineer at Fermi National Accelerator Laboratory and at CERN. This research was initially intended to be an experimental work. The change of topic and my professional assignments slowed down the course of the analysis. I am honored that Professor Patankar took the time to teach me the essentials of numerical analysis and guided me throughout those years.

I would like to give thanks to Professor S. W. Van Sciver, who provided fruitful guidance with respect to the understanding of the Helium II behavior. This research was motivated by Particle Image Velocimetry measurement of Helium II velocity profiles conducted by his team at the National High Magnetic Field Laboratory.

I am grateful for the necessary support and insightful discussions that I have had over the years with Dr L. Bottura. He permitted me to use the original THEA 1-D Partial Differential Equation solver.

I would like to thank the committee members, including Professor S. Lichter, who was also my professor of fluid mechanics and Professor W. Halperin, for his expertise in the field of Helium cryogenics.

A special thanks to Dr. Lucy De Barbaro and Dr. Duncan Brown, who proof read most of this manuscript Figures 2.1 to 2.4 are the courtesy of my former department head, J. Theilacker.

Throughout my carrier and interest in superfluidity, numerous colleagues have been influential and provided exemplary role-modeling. Institutions like CERN and Fermi national Accelerator Laboratory are crucial to enhance and inspire young engineers and physicists.

Finally and essentially, I would like to thank my parents, family, and friends for their marvelous support during the course of this “super-fluid” life. In harmony with my constant interest for phenomenological physics studies, they represent the forces of nature embodied in human being and, like pressure, are the true driver of the flow …

PREFACE

Solid-state physics describes the superfluidity as a macroscopic manifestation of quantum laws. Hundred years after the first liquefaction of Helium, which lead to the discovery of superconductivity, Helium II has become the most practical fluid exhibiting superfluidity. It is nowadays in common use both for technical and for scientific applications such as the high-field superconducting magnets and superconducting radio-frequency cavities.

The research of the Phenomenological and Numerical Studies of Helium II Dynamics in the Two-Fluid Model was driven by the fascination with the fundamental understanding of helium superfluidity. Years of work dedicated to the design, construction and operation of accelerator components in the field of High Energy Physics have spiked the curiosity to better understand this non-Newtonian fluid.

Whereas the original intent of the author was to study the behavior of Helium II using Particle Image Velocimetry (PIV) techniques, it became more relevant to focus on the numerical modelization of experimental results and studies, which were conducted in world-famous laboratories. Henceforth, the core of this research work has been devoted to enhance the numerical capacity and tools used to simulate Helium II in the two-fluid model.

In other words, Fundamental Physics and its Applications feed the technological progress, e.g. Helium II, accelerators and detectors are essentials discovery tools for the future generations. International scientific collaborations and its diversity program provided a “raison d’être” for numerous young talents around the world. The present study is one of its deliverable.

LIST OF ABBREVIATIONS

$\vec{\xi}$	parent-space (local) (ξ, η, ζ)
$\vec{x}$	physical-space (x,y,z)
α	diffusivity
Φ	potential function
ϕ	Gruneisen coefficient
ρ	bulk density
μ	dynamic fluid viscosity
η	viscosity
η_n	viscosity of the normal component
ρ_p	particle density
ρ_f	fluid density
ρn	normal fluid density
ρs	superfluid density
$\overline{\overline{\tau}}$	stress tensor
τ_{slip}	relaxation time due to the slip
ω	angular frequency
A_{GM}	Gorter-Mellink coefficient
C_p	specific heat at constant pressure
C_v	specific heat at constant density
c	speed of first sound $\left(\sqrt{\frac{dp}{d\rho}}\right)$
c_2	speed of second sound
c_{art}	artificial diffusion coefficient
C_D	drag coefficient

e	energy density
$f(T)^{-1}$	thermal conductivity function
F_B	body force
F_D	drag force
$\mathbf{F}_t$	force associated with turbulence (mutual friction)
F_B	body force
FE	Finite Element
g	gravity constant
He I	classical fluid state of ^{4}He
He II (Helium II)	superfluid state of ^{4}He
h	specific enthalpy
h	mesh size
h_K	Kapitza conductance
i	internal energy density
k	thermal conductivity
Kn	Knudsen number
LHC	Large Hadron Collider
L^2	Euclidean norm
L^{inf}	uniform norm
m	mass
$\overline{\overline{\mathbf{m}}}$, M	PDE mass matrix and its discrete version
$\overline{\overline{\mathbf{a}}}$, A	PDE advection matrix and its discrete version
$\overline{\overline{\mathbf{g}}}$, G	PDE diffusion matrix and its discrete version
$\overline{\overline{\mathbf{s}}}$, S	PDE source matrix and its discrete version
q, Q	PDE forcing vector and its discrete version
u, U	PDE vector of unknown

N	shape function
P	pressure
PDE	Partial Differential Equation
Pe	Peclet number
PIV	Particle Image Velocimetry
$\dot{q}$	heat flux
Ra	Rayleigh number
s	specific entropy
t	time
T	temperature
T_w	warm temperature
T_c	cold temperature
$T\lambda$	superfluid transition temperature for ^{4}He, 2.17 K
U_p	particle velocity
v	bulk fluid velocity field (v_x, v_y, v_z)
v	bulk fluid velocity
vn	normal fluid velocity vector (v_{nx}, v_{ny}, v_{nz})
vn	normal fluid velocity
vs	superfluid velocity vector (v_{sx}, v_{sy}, v_{sz})
vs	superfluid velocity
$X(T)$	heat conductivity function
w	velocity difference, v_n-v_s

A mes parents, Suzanne et Aimé Darve, et à ma famille.

"Ideals are like stars; you will not succeed in touching them with your hands. But like the Seafaring man on the desert of waters, you choose them as your guides, and following them you will reach your destiny"

~ by Carl Schurz

TABLE OF CONTENTS

LIST OF TABLES

Chapter 3

Chapter 4

Chapter 5

LIST OF FIGURES

Chapter 2

Chapter 4

Chapter 5

Appendices

1 INTRODUCTION

1.1 Research Outline

The need to correctly understand and model experimental results in helium cryogenics and related applications motivates the development of a three-dimensional numerical model capable of, among other things, simulating spherical particles flowing in Helium II [1]. The use of such tracer particles is essential in Particle Image Velocimetry (PIV) used to measure the velocity & flow of superfluid [2][3]. Controversy over the experimental results in PIV obtained at National High Magnetic Field Laboratory (NHMFL) by Van Sciver, Zhang and Celik [4], and the discrepancy between theoretical prediction and NHMFL's measurement of the velocity distribution in Helium II thermal counterflow (zero net mass flux), inspired us to undertake this work [5]. We found current models available in the scientific community either too limited (e.g., one-dimensional) or too complex and computationally penalizing to make them viable for particle studies related to PIV.

In this thesis work we present a computational method for solving a new set of equation addressing Helium II Dynamics in the Two-Fluid Model [6][7][8].

We begin our report with the general discussion of Helium properties, starting from the historical background up to the present, where superfluid ^{4}He has become a viable coolant for many technological applications [9]. Next we focus on atomic and nuclear properties of Helium and explain how the macroscopic quantum characteristics of its superfluid state can be understood in terms of the difference in the low temperature behavior of bosons and fermions. Helium phase diagrams (illustrated in Section 0) and thermo-physical properties (discussed in Section 2.1.4) offer further insights into the extraordinary properties of this element.

In practice, cryogenic applications require heat transfer from the system while maintaining the system at cryogenic temperatures. In this process, all aspects of heat transfer take place in a chain that includes heat removal from the system to the Helium and transport in stagnant or forced flow of Helium II. The importance of a precise knowledge of the heat transfer characteristics for practical applications can be inferred from the wealth of the analytical and experimental efforts devoted to cryogenics for the superconducting magnets, e.g., at the Large Hadron Collider (LHC) [10].

In Section 2.2 we introduce the two-fluid description as a very successful phenomenological representation of the properties of Helium II [11][12][13]. The idea of this model is to associate two co-existing fluids to the two different states of Helium: a super-fluid that approximately corresponds to the Helium atoms that have undergone Bose-Einstein condensation and are in their ground energy state, and a normal-fluid that corresponds to the fraction of helium atoms that are in excited states. The two fluids can move independently of each other at very low relative velocities, but otherwise, the interaction between them takes place through a microscopically complex mechanism that involves quantum vortices. In the case of heat induced flow, this interaction can be described by a simple power law dependence on the relative velocity, characteristic of the turbulent heat transport, as found by Gorter-Mellink [14].

An internal convection of the super-fluid and normal-fluid components can take place even without experiencing macroscopic motion, i.e., the bulk Helium II flow is zero. This possibility of an internal convection associated with a) the presence of a momentum source proportional to the temperature gradient in the motion equation of the normal-fluid and with b) the temperature dependence of the density of each fluid component, makes heat and mass transfer in Helium II inseparable. The main heat transport mechanism in Helium II, which is often referred to as the counterflow heat exchange, is associated with transfer of mass among the two-fluid components. We elaborate on the validity of this representation and give ample justification for the use of this model in our approach. Inducing a flow and thus taking advantage of the energy transfer through mass convection can further augment the large heat removal capability of Helium II. It has been shown that in the case of forced flow, the Gorter-Mellink mutual friction is still present, along with the energy convection induced by the mass flow.

Chapter 3 is devoted to the formulation of a system of Partial Differential Equations (PDE) for Helium II that is suitable for our purpose. Although common numerical approaches use the conserved variables, we use pressure, temperature, normal- and super-fluid velocities as explicit variables. The use of these variables has the advantage that the forcing terms in the equations are implicitly solved. Specifically, pressure is the driver of the flow, while temperature drives the heat flux. Having them as variables achieves a large degree of stabilization in the numerical solution without resorting to special techniques, or iterations. This allows us to increase the time step by one to two orders of magnitude beyond the Courant limit, dramatically improving the computational performance of the code, while being sufficiently accurate for the case of quasi-steady-state heat transfer in Helium II.

We take a macroscopic approach to the conservation laws, assuming local thermodynamic equilibrium, so that the state of Helium II as well as that of each of the two-fluid components is described by independent state variables. Following Roberts and Donnelly [15], we also employ the conservation of total energy density of the two flows in the derivation. Our resulting equations are of parabolic-hyperbolic form and contain terms representing internal heat convection through entropy transport, transformation of superfluid to normal fluid and vice-versa, as well as the internal energy dissipation associated with turbulence. The superfluid motion is driven by the divergence of the potential function we introduced (thermodynamic and gravity potentials) and is hence irrotational, as postulated in the two-fluid model.

To simplify our PDE system we postulate that the thermodynamic state does not depend on the relative composition and motion of the two fluids, which allows us to use standard thermodynamic relations (see Section 0), even though we understand the approximate nature of this approach [16]. Further assumptions and simplifications are summarized in chapter 3.2.1. The final explicit forms of these equations as functions of pressure, velocities and temperature are given in Table 3.1.

In Chapter 4, we describe the main framework of the numerical code, called 3DHeliumSolver, developed to solve these equations [17]. We made use of parts of an existing one-dimensional code of Thermal, Hydraulic and Electric Analysis (THEA), whose PDE solver has been transformed to solve three-dimensional hydro- and thermo-dynamics problems. We based the enhanced code on the three-dimensional Lagrangian finite element (FE) in space supplemented by a type of Beam-Warming algorithm in time.

Despite our various approximations, solving our system of PDE of Helium II is a challenging task. Many numerical approaches have been developed by the research community for Helium II models and we examined several viable options. The main difficulty in the integration comes from the nonlinearity terms inside the hyperbolic equations, corresponding physically to the vanishing viscosity of the superfluid component of Helium II. These terms generate important instabilities that one has to address as part of any model. Following the common approach, we utilized an artificial diffusion and examined code behavior through the whole spectrum of the Peclet number Pe (inversely proportional to the coefficient of artificial diffusion), where “0” and “infinity” represent “pure diffusion” and “pure convection”, respectively. As expected, the solution is well behaved at low Pe, but increasing Pe values lead to worse instabilities and oscillations during the numerical approximation to the solution, as we illustrate in Section 8.2. The physical phenomenon indicating this loss of regularity is the appearance of shocks (discontinuities) in the solution, as is often encountered in inviscid fluid flow simulations. On the other hand, we show that the use of finite difference (FD) algorithm with upwinding [18] in the context of a general class of finite element approximations results in a better behaved system, which in particular steady-state cases can be solved exactly. Henceforth (in this regime) we used the FE method augmented by the FD upwinding in 3DHeliumSolver to stabilize the outcomes.

The different form of the PDE is discussed and the scaling analysis permit to simplify the complete set of PDE obtained.

In Chapter 5 we report on the results of our 3DHeliumSolver in several test conditions. Due to the complexity of modeling accurately Helium II flow behavior, a staged approach was necessary. Ultimately, we describe the results obtained using the 3DHeliumSolver for the case of Helium II. In Section 5.5, we compare our approach with the methods, assumptions and variable selections of other Helium II simulations available in the scientific community. The propagation of the second sound and the thermal counterflow in Helium II has been simulated in 1-, 2-, and 3-dimensional space.

1.2 Potential Application of 3DHeliumSolver to PIV Technique

One motivation to support the generation of the three-dimensional numerical model for Helium II is driven by the need to help interpret experimental results obtained at NHMFL. Van Sciver, Zhang and Celik successfully observed the velocity distribution in a Helium II thermal counterflow using the Particle Image Velocimetry (PIV) technique. Since the normal fluid within Helium II has finite entropy, the PIV technique is capable of tracking the trajectory of the normal velocity component. In their experimental set-up, spherical particles were immersed in a Helium II bath to track the normal velocity component associated with heat transport [3]. In theory, if the net mass flow is zero, then the normal velocity, v_n, is given by :

$$\mathrm{v_n} = \frac{\dot{q}}{\rho\, s\, T} \tag{1.1}$$

where, s, is the entropy of the normal component, *T* the temperature and ρ is the bulk density. Thus, any heat transfer is accompanied by flow of normal fluid.

Large discrepancies, however, were found between the measured particle velocity and the theoretical normal fluid velocity, v_n. A correction for the slip velocity estimated between the normal fluid and the tracer particles was not sufficient to explain their experimental results. To support their results, theoretical investigations of the motion of tracer particles in Helium II has been carried out by Poole et. al [19] and suggest that the full interpretation of their results would require a three-dimensional numerical model capable of simulating the implementation of a particle in a Helium II bath where thermal counterflow can be modeled. This topic and controversy represent an excellent future research possibility with the 3DHeliumSolver code presented in this dissertation.

2 PROPERTIES OF HELIUM II

2.1 Fundamentals of Helium II

2.1.1 Historical Background

Helium (He) was first discovered by the French astronomer Jules Janssen in a spectrum of sunlight during a total solar eclipse visible in India in 1868. He observed a yellow line in the spectrum of the sun that he attributed to the radiation of a previously unobserved chemical element. Joseph Norman Lockyer confirmed this discovery and named it “helium”, from the Greek “Helios”, meaning the Sun. Helium is the most common element in the Universe after hydrogen. In Earth’s atmosphere its concentration is only 5 ppm (parts per mil), while in natural gas from the Earth the concentration of helium varies from 0.4% to 8%.

Helium was first liquefied in 1908 by the Dutch physist H. Kamerlingh Onnes at the University of Leiden [20]. This achievement gave him the possibility to test the thermophysical properties of metals immersed in a very low temperature fluid and in particular the behavior of electrical resistance as a function of temperature. This led, three years later, to the discovery of superconductivity when he observed the vanishing resistance of mercury as the temperature dropped below 4.15 K [21]. Onnes was awarded the Nobel prize for this discovery in 1913.

In 1910 H. K. Onnes and L. Dana measured the latent heat and specific heat of liquid helium and observed that near maximum density something unexpected happens to helium, which within a small temperature range is perhaps even discontinuous. The shape of the specific-heat curve resembled the Greek letter λ, and the corresponding point was hence called the lambda transition. The lambda transition was identified as a discontinuity, and the transition temperature 2.17 K was named T_λ. Twenty-seven years after the discovery of superconductivity, in 1938, it was recognized that the most common helium isotope with atomic mass 4, ^{4}He, undergoes a second order phase change when crossing the λ transition [22]. For temperatures above T_λ, ^{4}He is in the “normal” state, also called He I, and behaves as a Newtonian fluid. Below T_λ helium has remarkably different properties, behaving as a macroscopic quantum fluid with non-Newtonian characteristics, highly increased fluidity and extraordinary heat transport capability. This state of helium is commonly called Helium II.

In 1938, Kapitza and Allen and Misener independently reported no measurable resistance to the flow of Helium II through small capillaries with diameters of the order of 10^{-4} cm [23]. On the other hand, experiments using oscillating disks performed by Keesom and MacWood (1938) demonstrated the existence of a viscous drag, consistent with a viscosity coefficient not much less than that of helium gas. Therefore, it appeared as if Helium II were capable of being both viscous and non-viscous at the same time. A second example of the unique thermo-mechanical properties of Helium II is the fountain effect, consisting of a positive pressure head across a porous media induced by the heating of Helium II [24]. The two-fluid model described later in this chapter explains the apparent contradiction. Kapitza and Landau were awarded the Nobel prize for their work on Helium II. Since then, numerous experiments and studies on Helium II properties have driven our knowledge to where presently superfluid ^{4}He has become a viable coolant for technological applications, in particular for high field magnets.

Numerous fields including High Energy Physics (HEP), medical imaging, and energy storage today make use of high field, superconducting magnets cooled using superfluid ^{4}He. In 1980’s, Tore Supra was the first large physics instrument to use a Helium II cryogenic system at 1.8 K [25]. In the 1990’s, CEBAF was the first accelerator project using Helium II technology to cool superconducting RF cavities [26]. A yet more widespread use of Helium II for cooling high field laboratory magnets was built with Nb_3Sn or NbTi and operated at 1.8 K.

The Large Hadron Collider (LHC) at CERN (European Organization for Nuclear Research), Geneva, Switzerland, makes use of a large cryogenic capacity at 1.9 K for cooling the majority of its superconducting magnets around their accelerator ring [27]. Similar technology is planned for superconducting RF cavities used in future projects such as Project X at the Fermi National Accelerator Laboratory [28] or the European Spallation Source [29]. Finally, next generation NMR spectrometers, aiming at 25 Tesla fields and a resonating frequency above 1 GHz, will make use of low-temperature superconducting materials (Nb_3Sn and Nb_3Al) and will need to cool to Helium II temperatures to achieve their operating field.

2.1.2 Atomic and Nuclear Properties of Helium

Two stable isotopes of helium exist in nature, with atomic mass 3 and 4, indicated by ^{3}He and ^{4}He, respectively [30]. Gaseous ^{4}He is extracted from natural gas wells and represents 5.3×10^{-6} of the atmospheric air. The lighter isotope, ^{3}He composes less than 10^{-11} of atmospheric air and is mainly available as a by-product in the manufacture of nuclear devices. The two isotopes ^{3}He and ^{4}He have very different properties, both in their normal states (e.g. ^{3}He has a lower boiling point and higher vapor pressure than ^{4}He) as well as in their quantum, superfluid states described below. Unlike all other fluids, both helium isotopes remain liquid down to absolute zero, except under very high-pressure conditions (greater than 25×10^5 Pa). The persistence of the liquid phase can be explained by a combination of the weak inter-atomic forces and low atomic masses [31]. Only the isotope ^{4}He undergoes the phase change from He I to Helium II as the temperature is lowered below the lambda temperature. This change of phase is not shared by the ^{3}He isotope providing a conspicuous hint as to the reason of the appearance of the new ^{4}He state.

Indeed, the macroscopic quantum characteristics of Helium II can be understood in terms of the difference in the low temperature behavior of bosons and fermions. Bosons are particles with zero or integer values of spin, whereas fermions have half-spin values [32]. Pauli's exclusion principle states that a given energy level, defined by energy, angular momentum and spin, can be occupied by only one net fermion. The exclusion principle does not apply to bosons, so that an arbitrary number of bosons can occupy a given energy level. Because of this property, a gas of non-interacting bosons can *condense* below a transition temperature T_B, when thermal energy becomes sufficiently small. In this condition a substantial fraction of the total number of particles in the system occupies the state of lowest energy, called the *ground orbital*. This effect is called Bose-Einstein condensation.

The atom of ^{4}He is composed of 2 neutrons, 2 electrons and 2 protons, each of spin ½, so it has an even number of particles of spin ½, and is therefore a boson. As such, it can condense, forming an *ordered liquid*. The condensation temperature T_B for liquid ^{4}He can be estimated from theoretical considerations and is of the order of 3 K, i.e. close to the experimentally measured value for T_λ [12].

Hence, below $T_\lambda = 2.17$ K, a substantial fraction of the atoms of ^{4}He are in the condensed state, resulting in the visible, macroscopic quantum properties of Helium II.

The atom of ^{3}He, on the other hand, is composed of 1 neutron, 2 electrons and 2 protons, so it has a half-integer spin and is a fermion. In this case the Bose-Einstein condensation cannot take place, which explains why ^{3}He does not become a superfluid below 2.17 K. Nevertheless, at low temperatures (below 1 K), ^{3}He has unique behavior because its properties are governed by Fermi statistics. In fact, in contradiction with expectations, it has been found that ^{3}He also becomes a superfluid when cooled below about 3 mK. The quantum behaviour in this case has a different origin, which is similar to the mechanism that leads to a pairing of electrons into Cooper pairs below the critical temperature in electrical superconductors. The dilution and magnetic properties of ^{3}He have been used to attain temperatures in the mK range which are instrumental for applications like the Cryogenic Dark Matter experiment (CDMS) for which the germanium detector must be cooled to 10 mK [33]. The isotope ^{3}He is much more costly, and less commonly used, and is more difficult to handle than ^{4}He. Hence, in spite of the interesting properties and applications for ^{3}He, this thesis focuses exclusively on the superfluid properties of ^{4}He.

2.1.3 Helium Phase Diagram

As for any other fluid, helium is best characterized by examining its pressure-temperature (p,T) state diagram [3]. The phase diagram of ^{4}He is shown in Fig. 2.1. This diagram shows remarkable differences compared to common fluids. A peculiarity of helium is that it has no triple point for the coexistence of solid, liquid and vapor, as found for most substances. As mentioned previously, the liquid-vapor curve can be followed from the critical point ($T = 5.2$ K, $p = 2.23\text{x}10^5$ Pa) down to the absolute zero without any appearance of a solid. The solid phase appears only at a pressure larger than 25 10^5 Pa. This makes ^{4}He the ideal, and only, coolant for low-temperature superconducting applications. The lambda point ($T_\lambda = 2.172$ K, $p = 5{,}039$ Pa) is a triple point at which the liquid He I, liquid Helium II, and vapor coexist. A second triple point exists where the solid is in equilibrium with the He I and Helium II ($T = 1.76$ K. $p = 29.7\text{x}10^5$ Pa). The curve connecting the two triple points, the so called lambda line, separates the two forms of liquid ^{4}He, normal-fluid (He I) and super-fluid (Helium II).

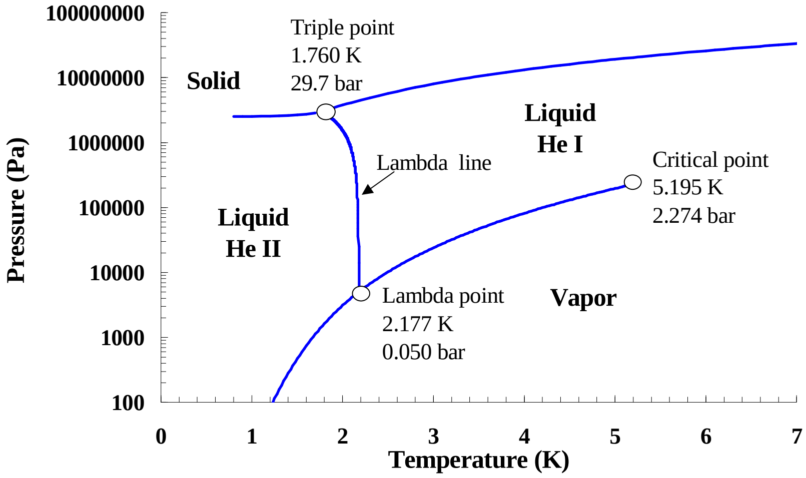

Figure 2.1: Phase diagram of ^{4}He

The distinction between liquid, vapor and mixed (liquid + vapor) phases is best examined in the temperature-entropy diagram of Fig. 2.2. Isenthalps and isobars in this diagram are used to analyze thermodynamic processes in cryogenic systems, e.g liquefaction of cryogenic fluids or refrigeration thermo-cycles. Two isobars for ^{4}He are shown at 0.1 MPa (normal conditions) and 2,000 Pa (a common working point for the production of saturated Helium II). The lambda and critical points are indicated in the plot. The saturation curve, the dome passing through the critical point, separates the one-phase from the two-phase domain of the fluid. The region on the left of the dome is the pure liquid region. Vapor is found on the right of the dome, while the liquid and vapor coexist in the region underneath the dome.

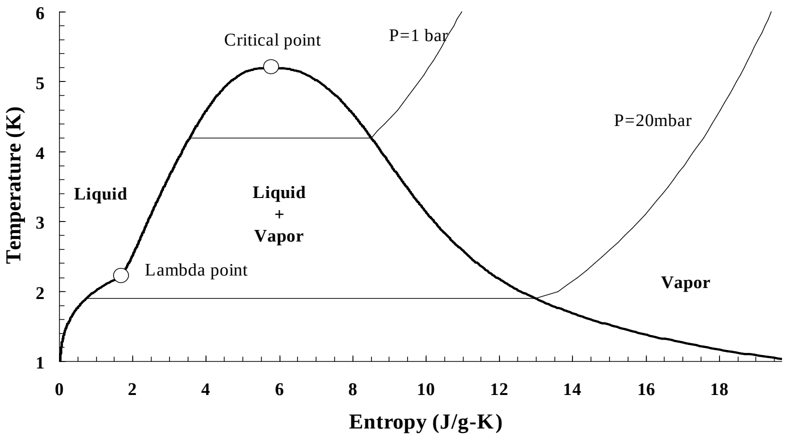

Figure 2.2: ^{4}He temperature-entropy diagram

2.1.4 Thermo-physical Properties of Helium II

In phase changes from He I to Helium II across the lambda transition most thermo-physical properties show strong variations or discontinuities. Fig. 2.3 shows the viscosity, η, of ^{4}He at 0.1 MPa, in units of micro-Poise. The viscosity change of the normal component is the primary parameter that marks the transition from normal to superfluid ^{4}He. The viscosity of helium in the normal state, i.e. with temperatures and pressures to the right of the λ line, is small compared to normal liquids but does not show anomalies in its temperature dependence. Conversely, the viscosity of Helium II II, i.e. at temperatures and pressures to the left of the λ line, is less than 10^{-7} of that of a normal gas.

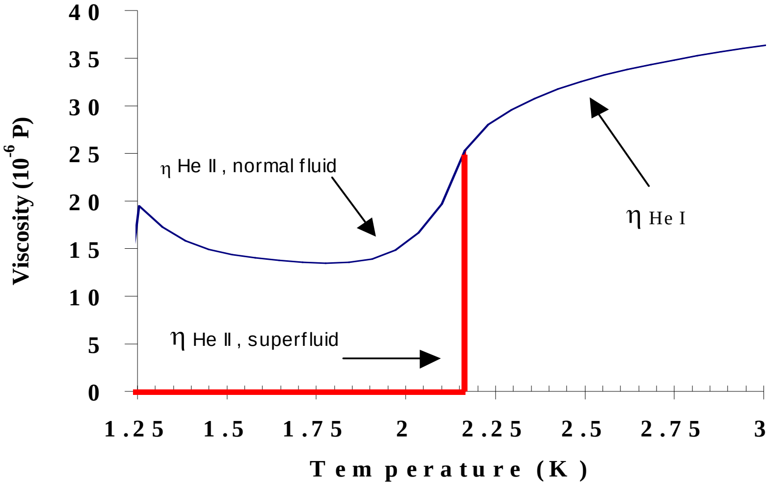

Figure 2.3: Viscosity of ^{4}He at 0.1 MPa versus temperature. The viscosity of the superfluid component drops ideally to zero below T_λ (2.17 K)

An interesting feature of the viscosity drop obtained by cooling is the possibility to reach high Reynolds number at moderate flow velocities and mass-flows. For this reason the use of very low temperatures is of interest in aerodynamics because it allows the design of wind tunnels with high Reynolds numbers and Mach numbers that cannot be achieved at ambient temperature. For example, the Cryogenic Helium Experiment Facility (CHEF) at National High Magnetic Field Laboratory (NHMFL) is used to study the influence of the friction factor for Reynolds number exceeding 10^7[34]

The amount of energy needed to raise the temperature of a kilogram of helium by one degree (the specific heat, C_p) shown in Fig. 2.4 is very large for both He I and Helium II. At the lambda transition, the heat capacity is strongly dependent on temperature having a peak the lambda transition. Compared to other materials in the same temperature range, the helium C_p is higher by several orders of magnitude. As an example, Copper has a C_p of 0.03 J/kg - K at 2 K, while the C_p of Al at the same temperature is approximately 0.11 J/kg - K. The specific heat of Helium II just below T_λ at 0.1 MPa is of the order of 12,400 J/kg - K, dropping to approximately 2,900 J/kg - K in the normal state. The lambda transition, first observed by H. K. Onnes and L. Dana is the sharp peak near 2.17 K. The implication of the large heat capacity is that at the phase change from Helium II to He I a large amount of heat can be absorbed under constant temperature conditions. This feature is used to provide a heat sink at nearly constant temperature, which is often necessary to stabilize superconducting cables against unforeseen heat dissipation. Note that the heat capacity decreases significantly with temperature below the lambda transition, thus making operation at temperatures much below T_λ less effective.

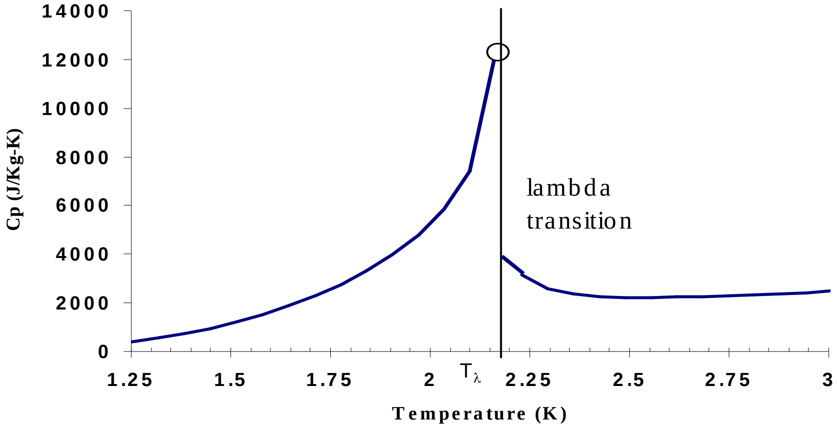

Figure 2.4: Specific heat of ^{4}He at 0.1 MPa

In addition to Helium II's specific heat being a unique property of liquid ^{4}He, its latent heat of vaporization also presents a very large advantage in cryogenic systems. The latent heat of vaporization of Helium II in the liquid phase of helium permits larger heat transport than thoughout the vapor phase at temperatures higher than 5 K. The latent heat of vaporization represents the energy required to transfer one kilogram of liquid helium to its gaseous state. It is representative of the intermolecular bonds associated with the formation of liquid. Helium II's latent heat of vaporization at 1.9 K is 23 kJ/kg and decreases rapidly to zero around 4 K. Although this value seems low compared to the latent heat of vaporization of classical fluids (used as coolants at room or higher temperatures, e.g., for water the latent heat of evaporation is 2,258 kJ/kg) it must be noted that only helium has a liquid phase in the temperature region compatible with the superconducting state of technical materials. The low absolute value for liquid helium is in any case appropriate for the operation of cryogenic systems that are optimized by nature to minimize heat loads at the cold end. As He I and Helium II have similar latent heats, it is possible to use either for cooling based on vaporization.

2.1.5 Heat Transfer in Helium II

Helium II is of technical interest for the practical applications discussed in the introduction mainly because of its superior heat transfer characteristics. For this reason the helium flow conditions considered in this research are those associated with the typical operation of Helium II as a coolant. Three aspects must be considered when examining the properties of the flow of Helium II in relation to heat transfer [35]. As for any other fluid, the flow field in Helium II is influenced by heat flow, especially when the thermo-physical properties have a strong non-linear dependence with temperature as discussed above. In addition, in the case of Helium II the picture is complicated by the fact that heat transfer, both in steady-state and transient conditions, has unusual characteristics originating from the mutual interaction of the normal- and super-fluid components. Finally, heat transfer from a heated wall to Helium II is not governed by classical thermal boundary layer theory and heat transfer correlations, as described below.

In practice, cryogenic applications require heat transfer from the system while maintaining cryogenic temperatures. In this process, all aspects of heat transfer take place in a chain that includes heat removal from the system to the helium and transport in stagnant or forced flow Helium II. The importance of a precise knowledge of the heat transfer characteristics for practical applications can be inferred from the analytical and experimental efforts devoted to cryogenics for superconducting magnets in the Interaction Regions (IR) of the Large Hadron Collider (LHC) [36]. The magnets in the IR regions are cooled by means of a heat exchanger made of a corrugated copper tube. Saturated Helium II flows inside of the exchanger tube, vaporizing along its length and absorbing the energy deposited in the static bath of Helium II that surrounds the rest of the magnet at 0.1 MPa. The heat transfer from the helium bath, which maintains the superconducting magnet at operating temperature, to the saturated helium in the heat exchanger tube is a key element in the design of the cryogenic system.

2.1.5.1 Stagnant Helium II – An early expression

In the domain of interest for the work presented here, the heat transfer in Helium II is accurately described by the Gorter-Mellink Eq. 2.9 of Section 2.2. This relation was experimentally verified by several teams of researchers during the 1970's. The early experimental approach taken by a French group at CEA/Grenoble has provided practical data useful for engineering design [37]. Their results for heat transfer in Helium II apply to a channel of length, *Length,* and cross sectional area, *Area*, filled with Helium II at 0.1 MPa and heated at one end with a total power, $\dot{q}$. The ends of the channel are maintained at cold and warm temperatures T_c and T_w. In this scenario, the steady-state heat transport in Helium II was found to be well approximated by [38] :

$$\frac{\dot{q}}{Area} = \left(\frac{X(T_c) - X(T_w)}{Lenght} \right)^{0.29} \tag{2.1}$$

where *X*(*T*) is the function shown in Fig. 2.5, obtained fitting experimental data. This function is related to the *f*(T) used in Eq. 2.13 of Section 2.2, and can be expressed by :

$$X(T) = 520\left\{1 - e^{-\left[3\cdot(2.16-T)^{2.5}\right]}\right\} \tag{2.2}$$

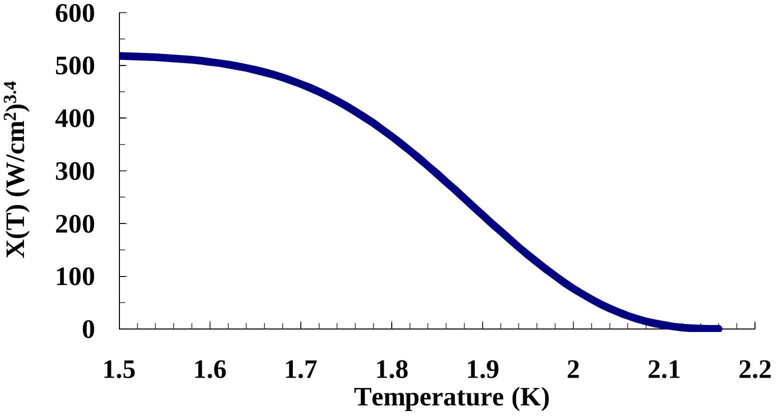

Figure 2.5: Heat conductivity function *X*(T) as obtained from experimental results of heat transfer in Helium II at 1 atmosphere [37].

It is interesting to compare heat transport in Helium II and other conducting materials used in cryogenic applications. To do this we compute the thermal conductivity equivalent to the heat transported in Helium II under the same temperature gradient. Based on equations (2.7) and (2.8), a 1-m long Helium II channel at 2 K is capable of transporting heat with an equivalent thermal conductivity of 2 kW/m - K. Copper and Aluminum, two of the best conducting materials, have a thermal conductivity in the range of 0.2 to 0.3 kW/m - K at 2 K. Thus the conductivity of Helium II is an order of magnitude better.

The large heat transport capability of Helium II is responsible for a drastic change in the macroscopic behavior of a helium bath cooled by pumping along the saturation curve of the temperature entropy diagram (see Fig. 2.2) once the temperature descends below the lambda point. Above T_λ, the heat is transported directly by mass convection and the He I bath is agitated by the production of large bubbles as He I boils-off. A sudden cessation of boiling occurs below T_λ, owing to the fact that heat is carried by internal convection without the need of the formation of helium bubbles at the heated surface.

2.1.5.2 Forced Flow of Helium II

Inducing a flow and thus taking advantage of the energy transfer through mass convection can further augment the large heat removal capability of Helium II. It has been shown that in the case of forced flow, the Gorter-Mellink mechanism is still present, along with the energy convection induced by the mass flow [3][39]. In a simple one-dimensional channel of length, cross-sectional area, and heated along its length with a total power $\dot{q}(x)$, the steady-state temperature profile is given by [30] :

$$\rho C_p \mathbf{v} \frac{dT}{dx} - \frac{d}{dx}\left(\frac{1}{f(T)} \frac{dT}{dx} \right)^{1/3} = \frac{\dot{q}(x)}{Area.Lenght} \tag{2.3}$$

This differs from the equation for a normal fluid by the presence of the additional term due to turbulence-modified internal convection [40]. The presence of this term causes a strong deviation of the temperature profiles from those expected for forced convection in normal fluids.

An example of the temperature profiles obtained at different forced flow rates in a channel of Helium II under constant heating power are shown in Fig. 2.6. In this measurement the pipe was heated in its center by a short heater. At zero flow velocity the temperature profile would resemble the one expected for pure conduction, i.e. perfectly symmetric and linear. The lack of symmetry visible in Fig. 2.6 for the case v=0 is due to an experimental difference in the inlet and outlet temperature conditions in the channel. In the presence of a forced flow the temperature profile is displaced in the downstream direction of the flow, approaching the ideal temperature distribution for a normal fluid (a step in temperature located at the heater) for large flow velocity. The reason is that the energy transport through mass convection (the first term in Eq. 2.9 increases with the forced flow velocity, while the internal convection (the second term in Eq. 2.9) does not depend on the flow velocity. At high enough velocity, the first mechanism mass convection and internal convection offset each other upstream of the heater, while they add to one another downstream of the heater as shown in Fig. 2.8 by the increasing asymmetry of the temperature profiles as the velocity increases. Thus, for the case of forced flow, the direct measurement of the velocity field could be used to determine the relative importance of the two heat transfer mechanisms.

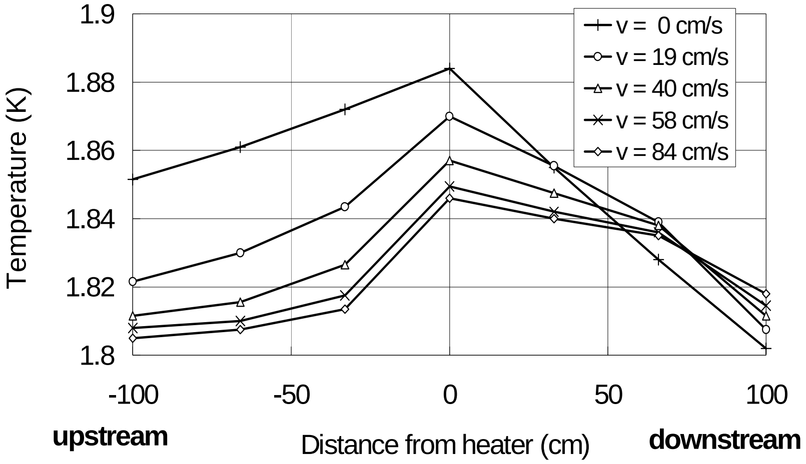

Figure 2.6: Temperature profiles as measured in a forced flow of Helium II at different velocities, redrawn from [39]

2.1.5.3 Kapitza Resistance

In Helium II the thermal resistance at the solid-fluid interface dominates heat transfer from a solid boundary to the bulk fluid. At cryogenic temperatures, and for small temperature differences, ΔT, the thermal resistance at the solid-fluid interface is due to the acoustic mismatch in the phonons at the transition between the two media [3]. Kapitza noted the phenomenon in 1941 during an experimental investigation of Helium II [22]. While studying the influence of heat transfer in capillaries, he first observed a temperature jump between Helium II and wall, which depended on the thermal heat flux across the interface. The corresponding thermal conductance was observed to vary as T^3, between T_λ and less than 1 K. It is experimentally determined from the ratio of the temperature difference across the interface, ΔT, and the heat flux at the interface. The Kapitza conductance, h_K, is defined as : $h_K = \frac{\dot{q}}{\mathbf{Area}\ \Delta T} = \alpha T^3$

(2.4)

One of the materials for which heat transfer to Helium II has been studied is copper. This is because of the high thermal conductivity of copper which is advantageous for electrical and thermal cryogenic applications. In addition, the high thermal conductivity of copper permits the measurement of the temperature of the solid side of the interface accurately and rapidly. Typical values of α for copper in contact with Helium II (in W/m^2-K) are between 400 and 900, depending on the surface morphology and cleaning [3]. Note that even though T is quite small, h_K can reach values one order of magnitude larger than typical heat transfer coefficients found for normal fluids. As an example, the value of the Kapitza heat transfer coefficient for copper in contact with Helium II at the lambda temperature are around 8,000 W/m^2-K, compared with 500 to 1,000 W/m^2-K for a forced flow of normal liquid He I and range to values of a few 1,000 to a few 10,000 W/m^2-K for boiling water and liquid metals.

Detailed knowledge of heat transfer from the solid wall to Helium II is of primary importance for stability and design of the cooling system for superconducting magnets, e.g. the Kapitza resistance was a key parameter determining the maximum heat transfer capability of the Inner Triplet - Heat Exchanger Test Unit (IT-HXTU) noted earlier [41].

2.2 Characteristics of the Two-fluid Model

The two-fluid model, introduced by Tisza in 1938 and completed by Landau, is presently the most effective phenomenological theory for predicting the behavior of Helium II [11]. This empirical model makes the assumption that Helium II consists of two interpenetrating fluid components. One component, called normal-fluid, has density ρ_n , finite viscosity η, entropy *s,* and behaves like a conventional viscous fluid. The other component, called superfluid, has density ρ_s , no viscosity, behaves like an ideal inviscid liquid and carries no entropy. In the framework of the two-fluid model, Helium II is a mixture of the normal-fluid and the superfluid components. At the lambda transition the mixture consists of the normal component only, while at absolute zero the mixture consists of the superfluid component only [42].

The development of this model was initially stimulated by the observation that Helium II can behave as if it were viscous and non-viscous at the same time. It was further thought that the presence of the two separate components could be associated with Bose condensation, the superfluid fraction being the condensed atoms, and the normal-fluid fraction identified with the excited atoms at energies above the ground orbital. This view however proved to be an oversimplification, as it can be shown theoretically that the fraction of atoms that can condense in a liquid such as Helium II is at most 10 % of the total. This means that the condensed fraction cannot be directly identified with the superfluid component of the two-fluid model.

In fact, although the two-fluid model postulates that Helium II behaves as a mixture of two fluids, the fluids themselves are physically indistinguishable and cannot be separated. In this respect the name of the two-fluid model is shorthand for describing the complex quantum interactions among the He atoms and lattice vibrations (phonons and protons) governing the macroscopic behavior of Helium II. More correctly, each of the two components in the two-fluid model should be regarded as different quantum states of the same atom, all atoms in Helium II being however identical. The quantum states are superposed and coexist, such that each atom can behave at the same time as a normal- as well as a super-fluid. The link to two-fluid model is that the probability of the existence of each state corresponds to the empirical composition rules of the fluid mixtures that are detailed below. In spite of its oversimplified nature, the two-fluid model has proven to be very effective in predicting and interpreting the behavior of Helium II. For this reason in the following discussion we still use the concept of separated normal- and a super-fluid components, keeping in mind the basic limitation of this approach.

The total density of Helium II, ρ, is the sum of the densities of the two components and is given by :

$$\rho = \rho_s + \rho_n \tag{2.5}$$

Fig. 2.7 shows the normalized density changes as a function of temperature, i.e. the ratio of the normal and superfluid density to the total density [12]. This ratio can be obtained either from measurements of the speed of sound propagation in Helium II or from the Andronikashvili experiment, consisting in a measurement of the period of oscillation of a pile of disks suspended on a torsion fiber and rotating in a bath of Helium II [43].

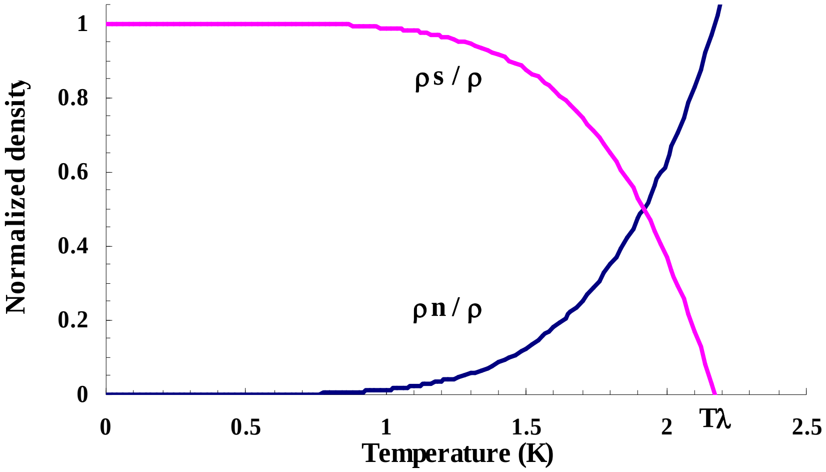

Figure 2.7: Density of Helium II – ratio of normal and superfluid densities in Helium II

Similar to the mass density, the total momentum density of Helium II, j, is the sum of the momentum densities of each component :

$$\mathrm{j} = \rho \mathrm{v} = \mathrm{v}_s \rho_s + \mathrm{v}_n \rho_n \tag{2.6}$$

where v is the bulk fluid velocity, while v_s and v_n are the velocities of the super-fluid and normal-fluid components respectively. The motion of the normal-fluid component is governed by an equation of the

Navier-Stokes type, containing however an additional momentum source term proportional to the temperature gradient and due to the interaction among the two fluid components [13]. In contrast, the motion of the superfluid component differs basically from that of any normal fluid because of its zero viscosity. A direct consequence is that stable irrotational flow patterns can exist, for which :

$$\nabla \times \mathrm{v}_s = 0 \tag{2.7}$$

resulting in the absence of classical turbulence for the superfluid [44][45].

In addition to the irrotational behavior as expected for an inviscid fluid, situations can arise when vortices can be generated in the superfluid component [46]. This is the case when Helium II flows in a multiply connected domain, i.e. containing a physical ”hole”. In this case the condition (3) does not necessarily prevent the flow around the hole. In fact, it can be shown that a persistent superfluid flow can exist if the circulation of the superfluid velocity along a path that encircles the hole has discrete values. These values are multiples of the so-called *quantum of circulation*. In practice the hole in the flow domain does not need to be provided by a physical solid boundary. For particular flow configurations, such as a rotating cylindrical bucket containing Helium II, holes appear spontaneously also in a simply connected domain [3]. The holes consist of a central normal fluid core completely surrounded by superfluid. These *quantized vortex lines* organize themselves in a regular geometric pattern. A gradient in the spatial distribution of the quantum vortices explains the possibility of observing, in spite of (3), a net circulation in Helium II.

If we consider Helium II at rest, i.e. when j = 0 and v = 0, one of the most striking consequences of the momentum addition rule (2) is that the velocities of the normal- and superfluid component v_n and v_s can still be different from zero provided that they are related by :

$$\mathrm{v}_s = -\frac{\rho_n \mathrm{v}_n}{\rho_s} \tag{2.8}$$

In other words, an internal convection of the superfluid and normal-fluid components can take place even if the bulk Helium II flow is zero.

The possibility of internal fluid convection (associated with the presence of a momentum source proportional to the temperature gradient in the motion equation of the normal-fluid and with the temperature dependence of the density of each fluid component) makes heat and mass transfer in Helium II inseparable. This is indeed the reason for the thermo-mechanical effects (e.g.,. the fountain effect mentioned earlier). The main heat transport mechanism in Helium II, which is often referred as the *counterflow heat exchange*, is also associated with the transfer of mass among the two fluid components and is particularly important for the later discussion. We consider a channel of stagnant Helium II, shown schematically in Fig. 2.4, in which one end is heated (the *warm* end) and the other end is kept at constant temperature by a heat sink (the *cold* end). Normal-fluid flows from the warm end to the cold end of the channel with a velocity v_n driven by temperature gradient [3]. Since the normal fluid has finite entropy, the displacement of the normal fluid component is associated with heat transport. If the net mass flow is zero, then the heat transported, $\dot{q}$ [W/m^2] is given by [47][48] :

$$\dot{q} = \rho\, s\, T\, \mathbf{v_n} \tag{2.9}$$

where, s, is the entropy of the normal component. Thus, any heat transfer is accompanied by flow of normal fluid.

Under very small heat fluxes, the relative motion of the two fluids takes place without interaction, in the so-called laminar regime (parallel flow lines). Of course by Poiseuille’s formula for flow of a viscous fluid in a channel, we expect :

$$\mathrm{v}_n = \frac{\beta}{\eta_n}\frac{\Delta P}{\Delta X} \tag{2.10}$$

where ΔX is the length of the channel, η_n is the viscosity of the normal fluid, and β is the constant depending on the geometry of the channel. Substituting into (5) leads to :

$$\dot{q} = \frac{\rho\, s\, T\, \beta}{\eta_n}\frac{\Delta P}{\Delta X} \tag{2.11}$$

Finally, using the two-fluid model and the internal energy for the mass of liquid helium, it can be shown that $\Delta p = \rho\, s\, \Delta T$, which is known as the thermo-mechanical effect, or fountain effect. Substituting this into (7) results in :

$$\dot{q} = \frac{(\rho\, s)^2 T\, \beta}{\eta_n} \frac{\Delta T}{\Delta X} \tag{2.12}$$

Thus, the heat flux is proportional to the temperature gradient, or equivalent to the pressure gradient. Note also that in this regime the temperature gradient is governed by the interaction of the normal-fluid with the walls of the tube through the parameter β.

The normal-fluid component transports heat from the warm end to the cold end. By extrapolation, we can picture this phenomenon as natural convection, albeit without gravity.

Under the constraint of zero bulk motion, no net mass displacement can take place and the total density must remain the same everywhere in the channel. The only way to achieve this is to have a flow of superfluid from the cold end to the warm end, with a velocity v_s given by (2.4), that guarantees at the same time that the momentum density is zero everywhere (i.e. the helium remains stagnant). At the warm end the superfluid component is converted to the normal state by the fact that the extra excitation due to the heat gives the superfluid enough energy to change the phase. At the cold end the normal-fluid component is converted to the superfluid state at the same time, while exchanging heat with the heat sink.

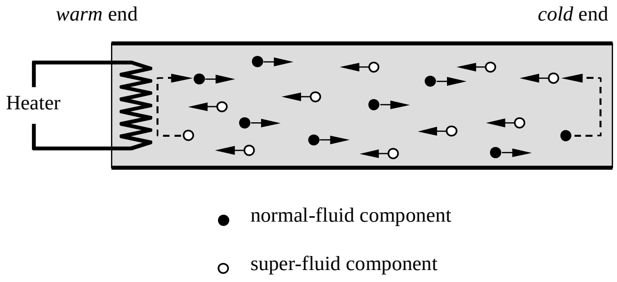

Figure 2.8: Helium II counterflow heat exchange schematically represented as internal convection of the normal- and superfluid components

In summary, heat transport in stagnant Helium II can be described within the frame of the two-fluid model by a dynamic flow of entropy carriers, as opposed to heat conduction as it is the case for normal substances for which little heat can be transported by a static fluid. For this reason the *counterflow heat exchange* is also often referred to as *internal convection*. It is finally important to stress the fact that the *internal convection* mechanism in a Helium II bath takes place in the presence of a heat flux even without experiencing macroscopic motion.

At heat fluxes of technical interest (above 1 kW/m^2) and for most practical channel geometries the normal-fluid becomes turbulent and the interaction between the two moving components causes an internal viscous drag between the normal-fluid and the superfluid. This interaction is also known as the Gorter-Mellink mutual friction mechanism [13]. In this case the motion of the normal component is no longer governed by equation 2.6. The Gorter-Mellink mutual friction term in the momentum balance for the superfluid component leads to a strongly non-linear energy transport, in contrast to the linear dependence implied by equation 2.8. A complete derivation of the normal fluid velocity in the turbulent regime, taking into account the Gorter-Mellink mutual friction, is rather long and details can be found in [39]. It is customary to write the associated heat flux (in one dimension) as follows :

$$\dot{q}^m = \frac{1}{f(T)}\frac{dT}{dx} \tag{2.13}$$

where the coefficient, m, and the function $f(T)^{-1}$ are in practice determined empirically from heat transfer measurements. Typically we use m=3. The function $f(T)^{-1}$ behaves like a thermal conductivity, meaning that the fluid property controls the temperature gradient in the presence of a heat flux. We has been shown that :

$$f(T) = \frac{A_{GM}\rho_n}{\rho_s^3 s^4 T^3} \tag{2.14}$$

The main difference between classical heat conduction and counterflow heat exchange is in the functional dependence of the heat flux on the temperature gradient. Classical conduction heat flux and laminar flow Helium II heat flux (8) are proportional to the temperature gradient, while for turbulent counterflow heat exchange in Helium II the heat flux depends on the temperature gradient raised to the power 1/3 (2.9).

Similarly, we could express this quantify as a function of the temperature and pressure :

$$\frac{1}{f(T,p)}=\frac{\rho^{2}s_{\lambda}^{4}T_{\lambda}^{3}}{A_{GM\,\lambda}}\left\{\left(\frac{T}{T_{\lambda}}\right)^{.5.7}\left[1-\left(\frac{T}{T_{\lambda}}\right)\right]^{5.7}\right\}^{3} \tag{2.15}$$

The function $f(T)^{-1}$ represents the effective thermal conductivity function and was fitted by Kashani et al. [39] . Fig. 2.8 displays $f(T)^{-1}$ for the atmospheric condition and for the temperature range of interest.

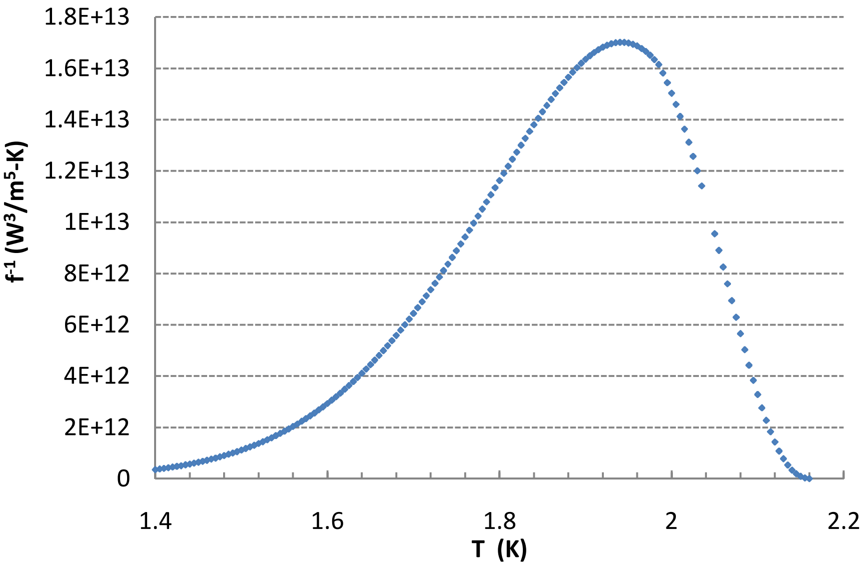

Figure 2.9: Effective conductivity function $f(T)^{-1}$

Practically speaking, if T_c is the cold temperature applied to the inlet surface and T_w is the warm temperature applied to the outlet surface of the channel, we can now approximate the heat transported by the Helium II in a steady-state by :

$$\dot{q}=\frac{1}{L}\int_{Tc}^{Tw}\left(\frac{1}{f(T)}\frac{dT}{dx}\right)^{\frac{1}{3}} \tag{2.16}$$

From the above equation and Eq. 1, we can estimate the normal component velocity, v_n. as follows :

$$\mathrm{v_n} = \frac{q^{\cdot}}{\rho\, s\, T} \qquad (2.17)$$

Knowing the total fluid density, ρ, we can also estimate the normal component density, ρ_n, as follows [3] :

$$\frac{\rho_n}{\rho} = \left(\frac{T}{T_\lambda}\right)^{5.6} \qquad (2.18)$$

Finally, we consider the thermal counterflow phenomena, where a temperature difference, caused by the application of a heat flux, drives the motion of the superfluid velocity component against the normal velocity component. Since the bulk velocity is zero, the expression for the superfluid velocity component, v_s, is :

$$\mathbf{v}_s = -\frac{\rho_n \mathbf{v}_n}{\rho_s} \qquad (2.19)$$

These expressions make it possible to estimate the main quantities used to monitor the behavior of He II.

3 MATHEMATICAL FORMULATIONS FOR HELIUM II

In this Chapter we derive a system of partial differential equations that is as complete and consistent as practical, and which is used for a 3-D solution of the flow of Helium II. In this process we necessarily make approximations, and justify them as we proceed. The solution has the form a general vector PDE, where in particular pressure and temperature, the main drivers of the flow, appear as explicit state variables.

3.1 System of Partial Differential Equations for the Two-Fluid Model

We base our discussion of the equations governing the hydrodynamics of He II on the two-fluid model discussed extensively in Section 2.2. Here we take a macroscopic approach to the conservation equations, assuming local thermodynamic equilibrium, so that the state of He II as well as that of each of the two fluid components can be described by two independent state variables (e.g. pressure p and temperature T). This assumption is not necessarily verified in all conditions, and we will discuss later the applicability of the assumptions made.

The mass, momentum and heat transfer of He II is interpreted in terms of the motion of two independent fluids, a normal and a superfluid. The superfluid component is non-viscous, and carries no entropy, while the normal component is viscous, with dynamic viscosity η, and carries a specific entropy S.

The total mass density of the fluid is given by the sum of the densities of each component :

$$\rho = \rho_n + \rho_s \tag{3.1}$$

The ratio of the mass densities of each fluid component to the total density of He II is a function of temperature and pressure. At zero temperature the density of the normal fluid is zero, while the superfluid density is equal to the total density. At the lambda point the normal density equals the total density, and the superfluid density is zero.

Similarly the momentum density of the He II can be divided in two parts, one part due to normal fluid motion and the second due to superfluid motion :

$$\rho \mathbf{v} = \rho_n \mathbf{v}_n + \rho_s \mathbf{v}_s \tag{3.2}$$

Finally we define the total energy density *e* of the mixture of the two fluids as follows :

$$e = i + \frac{\rho_n}{2\rho}\mathbf{v}_n^2 + \frac{\rho_s}{2\rho}\mathbf{v}_s^2 \tag{3.3}$$

where *i* is the internal energy density and the second and third term are the kinetic energy density associated with the normal and superfluid motions, respectively. The equations of motion for the two-fluid mixture are obtained from conservation balances which are applied to each component.

3.1.1 Mass Balance

We consider the mass balance first. The mass conservation for each fluid is given by [15]:

$$\frac{\partial \rho_n}{\partial t} + \nabla \cdot (\rho_n \mathbf{v}_n) = m \tag{3.4}$$

$$\frac{\partial \rho_s}{\partial t} + \nabla \cdot (\rho_s \mathbf{v}_s) = -m \tag{3.5}$$

where the *m* is the rate of generation of normal fluid mass in a differential volume, while –*m* is the rate of loss of superfluid mass in the same differential volume. In other words *m* is the rate at which normal fluid is created from superfluid. The conservation equation for the total mass is obtained by adding equations 3.4 and 3.5, and using the definitions of equations. 3.1 and 3.2 :

$$\boxed{\frac{\partial \rho}{\partial t} + \nabla \cdot (\rho \mathbf{v}) = 0 \qquad (3.6)}$$

3.1.2 Momentum Balance

To derive equations of motion for the superfluid and normal components we start by postulating the conservation of total momentum carried by the two components, i.e. :

$$\frac{\partial(\rho_n\mathbf{v}_n+\rho_s\mathbf{v}_s)}{\partial t}+\nabla\cdot(\rho_n\mathbf{v}_n\mathbf{v}_n+\rho_s\mathbf{v}_s\mathbf{v}_s)+\nabla p=-\nabla\cdot\overline{\overline{\tau}}+\rho\mathbf{g} \qquad (3.7)$$

where **g** is the acceleration of the gravity field and $\overline{\overline{\tau}}$ is a stress tensor, that depends only on the normal fluid and can be written as follows :

$$\nabla\cdot\overline{\overline{\tau}}=-\eta\left\{\nabla^2\mathbf{v}_n+\frac{1}{3}\nabla(\nabla\cdot\mathbf{v}_n)\right\} \qquad (3.8)$$

The momentum equation for the superfluid is [15] :

$$\rho_s\frac{\partial\mathbf{v}_s}{\partial t}+\rho_s\mathbf{v}_s\cdot\nabla\mathbf{v}_s+\nabla\Phi=\mathbf{F}_t+\rho_s\mathbf{g} \qquad (3.9)$$

where Φ is a potential function, defined in equation 3.12, and $\mathbf{F}_t$ is the force associated with turbulence (e.g., mutual friction), and appears only when the relative velocity between the superfluid and normal fluid components is larger than a critical value. Although the above balance is apparently in non-conservative form, and would hence seem inappropriate to describe the motion of the superfluid, Khalatnikov [13] and Roberts and Donnelly [15] argue that this equation is fundamental because in the absence of turbulence (i.e. when $\mathbf{F}_t = 0$) superfluid motion is driven by the divergence of potential functions (thermodynamic potential Φ and the gravity potential) and is hence irrotational. This is no longer the case in the presence of turbulence.

The equation for the motion of the normal-fluid component is derived by subtracting equation 3.9 from the conservation of total momentum (see Eq. 3.7). Using the continuity equations for each component (Eqs. 4 and 5) we easily obtain,

$$\rho_n\frac{\partial\mathbf{v}_n}{\partial t}+\rho_n(\mathbf{v}_n\cdot\nabla\mathbf{v}_n)+\nabla p-\rho_s\nabla\Phi=-\nabla\cdot\overline{\overline{\tau}}-\mathbf{F}_t+\rho_n\mathbf{g}-m\mathbf{w} \qquad (3.10)$$

where we have introduced the difference of normal and superfluid velocity **w** :

$$\mathbf{w}=\mathbf{v}_n-\mathbf{v}_s \qquad (3.11)$$

The thermodynamic potential Φ is derived by Roberts and Donnelly [15] in the general case, and is given by

$$\Phi = i + \frac{p}{\rho} - sT - \left(\frac{\rho_n}{2\rho}\right) w^2 \tag{3.12}$$

It is important to note that this depends not only on the usual thermodynamic state variables (internal energy *i*, pressure *p*, density ρ, entropy *s* and temperature *T*), but also on the relative velocity of the normal and superfluid components, as well as the normal fluid density. Furthermore, Roberts and Donnelly derive differentials of the internal energy and the potential Φ, given by [15] :

$$di = \frac{p}{\rho^2} d\rho + T ds + \frac{w^2}{2} d\left(\frac{\rho_n}{\rho}\right) \tag{3.13}$$

$$d\Phi = \frac{1}{\rho} dp - s dT - \left(\frac{\rho_n}{2\rho}\right) dw^2 \tag{3.14}$$

Using now Eq. 3.14 in the momentum balances for the superfluid and normal fluid components we arrive, after simple algebra, with the following equations :

$$\boxed{\rho_n \frac{\partial \mathbf{v}_n}{\partial t} + \rho_n \left(\mathbf{v}_n \cdot \nabla \mathbf{v}_n\right) + \frac{\rho_n}{\rho} \nabla p + \rho_s s \nabla T + \frac{\rho_s \rho_n}{2\rho} \nabla w^2 = -\nabla \cdot \overline{\overline{\tau}} - \mathbf{F}_t + \rho_n \mathbf{g} - m\mathbf{w} \quad (3.15)}$$

$$\boxed{\rho_s \frac{\partial \mathbf{v}_s}{\partial t} + \rho_s \left(\mathbf{v}_s \cdot \nabla \mathbf{v}_s\right) + \frac{\rho_s}{\rho} \nabla p - \rho_s s \nabla T - \frac{\rho_s \rho_n}{2\rho} \nabla w^2 = \mathbf{F}_t + \rho_s \mathbf{g} \quad (3.16)}$$

For convenience, we can use the continuity Eqs. 3.4 and 3.5 and write a conservation balance for the momentum of each component :

$$\frac{\partial (\rho_n \mathbf{v}_n)}{\partial t} + \nabla \cdot \left(\rho_n \mathbf{v}_n \mathbf{v}_n\right) + \frac{\rho_n}{\rho} \nabla p + \rho_s s \nabla T + \frac{\rho_s \rho_n}{2\rho} \nabla w^2 = -\nabla \cdot \overline{\overline{\tau}} - \mathbf{F}_t + \rho_n \mathbf{g} + m\mathbf{v}_s \tag{3.17}$$

$$\frac{\partial (\rho_s \mathbf{v}_s)}{\partial t} + \nabla \cdot \left(\rho_s \mathbf{v}_s \mathbf{v}_s\right) + \frac{\rho_s}{\rho} \nabla p - \rho_s s \nabla T - \frac{\rho_s \rho_n}{2\rho} \nabla w^2 = \mathbf{F}_t + \rho_s \mathbf{g} - m\mathbf{v}_s \tag{3.18}$$

In the two sets of equations above the first and second terms on the left hand side are the acceleration terms. The third term is the force due to the pressure gradient. The fourth term is the pressure originated by the thermo-mechanical effect, which demonstrates how a temperature gradient can cause a counterflow in the mixture. The fifth term originates from mass exchange among the two fluids in He II. It is important to note that the terms can differ by orders of magnitude. For small accelerations, and modest Mach numbers, the thermomechanical and the turbulent force terms tend to dominate the balance in Eqs. 3.15 and 3.16 (or Eqs. 3.17 and 3.18).

At this point it is also interesting to note that the effect of the transformation of superfluid into normal fluid, and *vice versa*, produces a term (*m* **w)** in the normal fluid equation Eq. 3.15, but not in the superfluid equation Eq. 3.16. This is a consequence of the assumption of conservation of total momentum Eq. 3.7 and of irrotational superfluid flow Eq. 3.9. Indeed, the form presented here is different from the one obtained by Ramadan and Witt [49]. The reason is that their starting assumption was of momentum conservation in each species, which resulted in the appearance of mass exchange term both for the normal as well as the superfluid non-conservative equations.

3.1.3 Energy Balance

We turn now to the equation of energy conservation. Khalatnikov [13] uses the fact that for irreversible motion the entropy is conserved to write a balance that can be used in place of the energy conservation equation :

$$\frac{\partial(\rho\, s)}{\partial t} + \nabla\cdot\left(\rho\, s\, \mathbf{v}_n\right) = 0 \tag{3.19}$$

This balance must be modified in case of internal dissipation and external heat sources. In fact, the direct use of entropy is not convenient in the solution of the equation of motion. A different form, derived from the conservation of total energy density, is given by Roberts and Donnelly [15] :

$$\begin{gathered}\frac{\partial}{\partial t}\left(\rho i + \frac{\rho_n \mathbf{v}_n^2}{2} + \frac{\rho_s \mathbf{v}_s^2}{2}\right) + \nabla\cdot\left(\rho i \mathbf{v} + \frac{\rho_n \mathbf{v}_n^2}{2}\mathbf{v}_n + \frac{\rho_s \mathbf{v}_s^2}{2}\mathbf{v}_s\right) \\ + \nabla\cdot\left(p\mathbf{v}\right) + \nabla\cdot\left(\rho_s s T \mathbf{w}\right) + \nabla\cdot\left(\frac{\rho_s \rho_n}{2\rho} w^2 \mathbf{w}\right) - \nabla\cdot\left(k\nabla T\right) = -\nabla\cdot\left(\bar{\bar{\tau}}\mathbf{v}_n\right) + \rho\mathbf{g}\cdot\mathbf{v} + q\end{gathered} \tag{3.20}$$

The first two terms on the left hand side of Eq. 3.20 represent the change in total energy density, i.e. the sum of the internal energy density and the specific kinetic energy of the two flows. It is possible to simplify the energy balance by subtracting the kinetic energy balance from Eq. 3.20. This is obtained taking Eqs. 3.17 and 3.18, multiplying each by $\mathbf{v}_n$ and $\mathbf{v}_s$, respectively, and by applying the property :

$$\mathbf{v} d(\rho \mathbf{v}) = d\left(\frac{\rho \mathbf{v}^2}{2}\right) \tag{3.21}$$

The kinetic energy balance resulting from the addition of the energies of each component is:

$$\begin{aligned} &\frac{\partial}{\partial t}\left(\frac{\rho_n \mathbf{v}_n^2}{2} + \frac{\rho_s \mathbf{v}_s^2}{2}\right) + \nabla \cdot \left(\frac{\rho_n \mathbf{v}_n^2}{2}\mathbf{v}_n + \frac{\rho_s \mathbf{v}_s^2}{2}\mathbf{v}_s\right) + \\ &\mathbf{v} \cdot \nabla p + \rho_s s \mathbf{w} \cdot \nabla T + \frac{\rho_s \rho_n}{2\rho}\mathbf{w} \cdot \nabla w^2 + \mathbf{F}_t \cdot \mathbf{w} = -\mathbf{v}_n \cdot \nabla \cdot \bar{\bar{\tau}} + \rho \mathbf{g} \cdot \mathbf{v} - \frac{m}{2} w^2 \end{aligned} \tag{3.22}$$

Subtracting the above balance of mechanical energy from the total energy balance (Eq. 3.20) we obtain the following equation :

$$\frac{\partial(\rho i)}{\partial t} + \nabla \cdot (\rho i \mathbf{v}) + p \nabla \cdot \mathbf{v} + T \nabla \cdot (\rho_s s \mathbf{w}) + w^2 \nabla \cdot \left(\frac{\rho_s \rho_n}{2\rho}\mathbf{w}\right) - \mathbf{F}_t \cdot \mathbf{w} - \nabla \cdot (k \nabla T) = -\bar{\bar{\tau}} \cdot \nabla \mathbf{v}_n + q + \frac{m}{2} w^2 \tag{3.23}$$

A final modification is to subtract the total continuity equation. Eq. 3.6 multiplied by *i*, leading to the final form for the conservation of internal energy :

$$\rho \frac{\partial i}{\partial t} + \rho \mathbf{v} \cdot \nabla i + p \nabla \cdot \mathbf{v} + T \nabla \cdot (\rho_s s \mathbf{w}) + w^2 \left(\nabla \cdot \left(\frac{\rho_s \rho_n}{2\rho}\mathbf{w}\right) - \frac{m}{2}\right) - \mathbf{F}_t \cdot \mathbf{w} - \nabla \cdot (k \nabla T) = -\bar{\bar{\tau}} \cdot \nabla \cdot \mathbf{v}_n + q \tag{3.24}$$

We note that several terms in Eq. 24 are non-standard. The term $T \nabla \cdot (\rho_s s \mathbf{w})$ represents an internal heat convection through entropy transport. The term(s) $w^2 \left(\nabla \cdot \left(\frac{\rho_s \rho_n}{2\rho}\mathbf{w}\right) - \frac{m}{2}\right)$ originate from the transformation of a superfluid into normal fluid and vice *versa*. Finally, the term $-\mathbf{F}_t \cdot \mathbf{w}$ represents the internal energy dissipation associated with turbulence.

3.1.4 Closure of the PDE System

In summary, the two-fluid model is completely described by Eq. 3.6 (total mass balance), Eq. 3.15 (normal fluid momentum balance), Eq. 3.16 (superfluid momentum balance), and Eq 3.24 (internal energy balance). In addition we require a suitable state equation, providing all thermodynamic quantities as a function of two state variables. As indicated already, we choose pressure and temperature as the state variables, and the state equation required is therefore in the form :

$$\rho = \rho(p,T) \tag{3.25}$$

from which the other state variables are derived, and in particular :

$$\rho_n = \rho_n(p,T) \tag{3.26}$$

$$i = i(p,T) \tag{3.27}$$

$$s = s(p,T) \tag{3.28}$$

Constitutive relations are also needed for all thermophysical quantities (e.g. viscosity or thermal conductivity). We assume that these are similarly available as a function of pressure and temperature, i.e. ;

$$\eta = \eta(p,T) \tag{3.29}$$

$$k = k(p,T) \tag{3.30}$$

Additionally, suitable initial and also boundary conditions are needed for a unique flow field to exist. We note finally that the form of the turbulent force has also not yet been specified. Although in principle any form is viable at this stage, a suitable approximation was found by Gorter and Mellink for the case of counterflow [14].

3.2 Expressing Partial Differential Equations in (p, v_n, v_s, T) Variables

The numerical solution of the equations derived in the previous section is by no means trivial. The equations are complex, involve terms that are non-standard, and also contain terms that largely dominate the balances, e.g. the thermomechanical force or the mutual friction in the momentum balances. For this reason it is convenient to rearrange them and write them in a simplified form where pressure, velocities and temperature appear explicitly as variables in the derivatives. We refer to this choice as the (p, $\mathbf{v}_n$, $\mathbf{v}_s$, T) form of the PDE system.

The main advantage of this is that these variables are leading order in all dominating terms of the balances, and treating them implicitly in the solution algorithm will largely improve the stability of the integration. To modify the equations as desired, however, we make the assumption that the thermodynamic state is independent of the composition and relative motion of the mixture of the two fluids. As shown by Roberts and Donnelly [15], this is not exact. Indeed, for the two-fluid system the internal energy i and thermodynamic potential Φ depend on the relative motion of the two fluids, as is apparent from the differentials of Eqs. 3.13 and 3.14. Making the assumption that the thermodynamic state does not depend on the relative composition and motion of the two fluids we introduce an error of the order of $\frac{\rho_n}{\rho}\frac{w^2}{2}$. The advantage however is that standard thermodynamic relations can be used, and in particular the following relations hold :

$$h = i + \frac{p}{\rho} \qquad (3.31)$$

$$di = \left(\frac{p}{\rho} - \phi C_v T\right)\frac{d\rho}{\rho} + C_v dT \qquad (3.32)$$

$$d\rho = \frac{1+\phi}{c^2}dp - \frac{\phi\rho}{c^2}dh \qquad (3.33)$$

where ϕ is the Gruneisen parameter, C_v is the specific heat at constant density, c is the speed of (first) sound and h is the specific enthalpy.

We outline here how the equations are transformed, based on standard algebra and calculus. We start by writing the continuity and energy balances in the following form :

$$\frac{\partial\rho}{\partial t} + \mathbf{v}\cdot\nabla\rho + \rho(\nabla\cdot\mathbf{v}) = 0 \qquad (3.34)$$

$$\rho\frac{\partial i}{\partial t}+\rho\mathbf{v}\cdot\nabla i+p\left(\nabla\cdot\mathbf{v}\right)=\dot{q}+\nabla\cdot\left(k\nabla T\right)+\mathbf{F}_t\cdot\mathbf{w}-\bar{\bar{\tau}}\cdot\nabla\cdot\mathbf{v}_n-T\nabla\cdot\left(\rho_s s\mathbf{w}\right)-w^2\left(\nabla\frac{\rho_s\rho_n}{2\rho}\mathbf{w}-\frac{m}{2}\right)$$

(3.35)

To simplify the notation we group the whole right hand side of Eq. 3.35 into a single quantity *Q*, i.e. we write,

$$\rho\frac{\partial i}{\partial t}+\rho\left(\mathbf{v}\cdot\nabla i\right)+p\left(\nabla\cdot\mathbf{v}\right)=Q \tag{3.36}$$

where we have defined :

$$Q=\dot{q}+\nabla\cdot\left(k\nabla T\right)+\mathbf{F}_t\cdot\mathbf{w}-\bar{\bar{\tau}}\cdot\nabla\cdot\mathbf{v}_n-T\nabla\cdot\left(\rho_s s\mathbf{w}\right)-w^2\left(\nabla\cdot\left(\frac{\rho_s\rho_n}{2\rho}\mathbf{w}\right)-\frac{m}{2}\right) \tag{3.37}$$

We modify the energy equation using the definition of the internal energy differential of Eq. 3.32. Substitution into Eq. 3.36 yields the following result,

$$\rho C_v\frac{\partial T}{\partial t}+\rho C_v\mathbf{v}\cdot\nabla T+\rho\left(\frac{p}{\rho}-\phi C_v T\right)\frac{\partial\rho}{\partial t}+\rho\left(\frac{p}{\rho}-\phi C_v T\right)\mathbf{v}\cdot\nabla\rho+p\left(\nabla\cdot\mathbf{v}\right)=Q \tag{3.38}$$

which can also be written in the following alternative form :

$$\rho C_v\frac{\partial T}{\partial t}+\rho C_v\mathbf{v}\cdot\nabla T+\rho\phi C_v T\nabla\cdot\mathbf{v}+\rho\left(\frac{p}{\rho}-\phi C_v T\right)\left(\frac{\partial\rho}{\partial t}+\mathbf{v}\cdot\nabla\rho+\rho\nabla\cdot\mathbf{v}\right)=Q \tag{3.39}$$

We recognize readily that the last term on the left hand side is zero by virtue of Eq. 3.34, and finally

obtain an equation for the temperature (one of the desired results) :

$$\boxed{\rho C_v\frac{\partial T}{\partial t}+\rho C_v\mathbf{v}\cdot\nabla T+\rho\phi C_v T\left(\nabla\cdot\mathbf{v}\right)=Q} \tag{3.40}$$

To obtain an equation for pressure we substitute the definition of the density differential of Eq. 3.33 into the continuity equation 3.34, and obtain the following equation that contains pressure and enthalpy :

$$\frac{1+\phi}{c^2}\left(\frac{\partial p}{\partial t}+\mathbf{v}\cdot\nabla p\right)-\frac{\rho\phi}{c^2}\left(\frac{\partial h}{\partial t}+\mathbf{v}\cdot\nabla h\right)+\rho(\nabla\cdot\mathbf{v})=0 \tag{3.41}$$

To remove the dependence on enthalpy we modify again the energy balance of Eq. 3.36, using this time the definition of the enthalpy (see Eq. 3.31), and obtain the following equation for enthalpy and pressure :

$$\rho\frac{\partial h}{\partial t}+\rho\mathbf{v}\cdot\nabla h-\frac{\partial p}{\partial t}-\mathbf{v}\cdot\nabla p+\frac{p}{\rho}\left(\frac{\partial\rho}{\partial t}+\mathbf{v}\cdot\nabla\rho+\rho(\nabla\cdot\mathbf{v})\right)=Q \tag{3.42}$$

As observed previously, we note that the last term on the left hand side is zero due to Eq. 3.34, and hence the relation between enthalpy and pressure is :

$$\rho\frac{\partial h}{\partial t}+\rho\mathbf{v}\cdot\nabla h=\frac{\partial p}{\partial t}+\mathbf{v}\cdot\nabla p+Q \tag{3.43}$$

This can be written in the following alternative form :

$$\frac{\rho\phi}{c^2}\left(\frac{\partial h}{\partial t}+\mathbf{v}\cdot\nabla h\right)=\frac{\phi}{c^2}\left(\frac{\partial p}{\partial t}+\mathbf{v}\cdot\nabla p\right)+\frac{\phi}{c^2}Q \tag{3.44}$$

The result of Eq. 3.44 can be used directly and substituted into Eq. 3.41 to obtain the equation for pressure :

$$\boxed{\frac{\partial p}{\partial t}+\mathbf{v}\cdot\nabla p+\rho c^2(\nabla\cdot\mathbf{v})=\phi Q} \tag{3.45}$$

Equations 3.40 and 3.45 are general results, which are exact for classical hydrodynamics. In our case we recall that this result has been necessarily approximated, and is subject to the validity of Eqs. 3.31, 3.32, and 3.33.

A complete set of partial differential equations is now obtained for Helium II in the p, v_s, v_n ,T form, consisting of a pressure Eq. 3.45, equations of motion for the superfluid and normal fluid components, (Eqs. 15 and 16), a temperature equation (Eq. 3.40), together with the definition of *Q* of Eq. 3.37.

3.2.1 Model Assumptions Taken During Derivation

In the course of the derivation, we used the assumption of local thermodynamic equilibrium such that the state of Helium II as well as each of its two fluid components were described by independent state variables and not dependent on the composition and relative motion of the mixture. We now make some additional substitutions and assumptions that further simplify the form obtained;

1) The friction force, given by the following empirical expression proposed by Gorter and Mellink [15] :

$$\mathbf{F}_t = A\rho_s\rho_n w^2\mathbf{w} \tag{3.46}$$

Here *A* is a function of *T* and could also depend on *w*; A=A_{GM}

2) The divergence of the total velocity is computed using Eqs. 3.1 and 3.2 through the chain relation ;

$$\nabla\cdot\mathbf{v} = \nabla\cdot\left(\frac{\rho_n}{\rho}\mathbf{v}_n + \frac{\rho_s}{\rho}\mathbf{v}_s\right) = \frac{\rho_n}{\rho}(\nabla\cdot\mathbf{v}_n) + \frac{\rho_s}{\rho}\nabla\cdot\mathbf{v}_s + \mathbf{v}_n\cdot\nabla\frac{\rho_n}{\rho} + \mathbf{v}_s\cdot\nabla\frac{\rho_s}{\rho} \tag{3.47}$$

Here the normal and superfluid velocities appear explicitly. We make use in addition of Eq. 3.11 defining the velocity difference.

3) The contributions related explicitly to mass exchange *m* are small in comparison to other terms, and we drop these from the balances.

4) The energy dissipated by viscous dissipation is also small when compared to other sources of heat transport (e.g. mutual friction). This term may therefore be treated as a source perturbation.

5) All terms containing differentials of quantities other than variables *p*, $\mathbf{v}_n$, $\mathbf{v}_s$, *T* are small compared to the terms containing the differentials of the variables themselves. In other words we can regard them as perturbations with respect to the leading terms in the equations.

6) We assume that variations of the Gruneisen parameter are small, such that :

$$\phi\nabla(k\nabla T) \approx \nabla(\phi k\nabla T) \tag{3.48}$$

3.2.2 Final Partial Differential Equation System

We now consider the final PDE system for the thermodynamic state and the 3-D flow simulation of the normal and super-fluid components of helium II. With the assumptions of Sections 0 and 0 it is now possible to come to a set of approximate equations that were sought. These are reported in Table 3.I and we observe a time derivative term, the convective flux terms (gradient of the system variables), the diffusive terms (Laplacian of the system variables), the non-linear source terms (proportional to the system variables), the linear source terms and perturbations. Eq. 3.49 governs the evolution of pressure, whereas Eqs. 3.50 and 3.51 give the flow field in 3-D, while Eq. 3.52 governs the evolution of temperature. The notation for the various differential operators, for the case of application to scalars, vectors or matrices, is reported in Appendix 8.1

$$\begin{gathered}\frac{\partial p}{\partial t}+\left(\frac{\rho_n\mathbf{v}_n+\rho_s\mathbf{v}_s}{\rho}\right)\cdot\nabla p+\rho_n c^2\left(\nabla\cdot\mathbf{v}_n\right)+\phi w^2\frac{\rho_s\rho_n}{2\rho}\left(\nabla\cdot\mathbf{v}_n\right)+\phi T\rho_s s\left(\nabla\cdot\mathbf{v}_n\right)+\rho_s c^2\left(\nabla\cdot\mathbf{v}_s\right)-\phi w^2\frac{\rho_s\rho_n}{2\rho}\left(\nabla\cdot\mathbf{v}_s\right)-\phi T\rho_s s\left(\nabla\cdot\mathbf{v}_s\right)-\\-\nabla\cdot\left(\phi k\nabla T\right)-\phi A\rho_s\rho_n w^2\left(\mathbf{w}\cdot\mathbf{v}_n\right)+\phi A\rho_s\rho_n w^2\left(\mathbf{w}\cdot\mathbf{v}_s\right)=\\\phi q-\phi\overline{\overline{\tau}}\cdot\nabla\cdot\mathbf{v}_n-\rho c^2\left(\mathbf{v}_n\cdot\nabla\frac{\rho_n}{\rho}\right)-\rho c^2\left(\mathbf{v}_s\cdot\nabla\frac{\rho_s}{\rho}\right)-\phi T\left(\mathbf{w}\cdot\nabla\rho_s s\right)-\phi w^2\left(\mathbf{w}\cdot\nabla\frac{\rho_s\rho_n}{2\rho}\right)\end{gathered}\tag{3.49}$$

$$\rho_n\frac{\partial\mathbf{v}_n}{\partial t}+\frac{\rho_n}{\rho}\nabla p+\rho_n\mathbf{v}_n\cdot\nabla\mathbf{v}_n+\frac{\rho_s\rho_n}{\rho}\mathbf{w}\cdot\nabla\mathbf{v}_n-\frac{\rho_s\rho_n}{\rho}\mathbf{w}\cdot\nabla\mathbf{v}_s+\rho_s s\nabla T+\left(A\rho_s\rho_n w^2\right)\mathbf{v}_n-\left(A\rho_s\rho_n w^2\right)\mathbf{v}_s=-\nabla\cdot\overline{\overline{\tau}}+\rho_n\mathbf{g}\tag{3.50}$$

$$\rho_s\frac{\partial\mathbf{v}_s}{\partial t}+\frac{\rho_s}{\rho}\nabla p-\frac{\rho_s\rho_n}{\rho}\mathbf{w}\cdot\nabla\mathbf{v}_n+\rho_s\cdot\mathbf{v}_s\nabla\cdot\mathbf{v}_s+\frac{\rho_s\rho_n}{\rho}\mathbf{w}\cdot\nabla\mathbf{v}_s-\rho_s s\nabla T-\left(A\rho_s\rho_n w^2\right)\mathbf{v}_n+\left(A\rho_s\rho_n w^2\right)\mathbf{v}_s=\rho_s\mathbf{g}\tag{3.51}$$

$$\begin{gathered}\rho C_v\frac{\partial T}{\partial t}+\rho_n\phi C_v T\left(\nabla\cdot\mathbf{v}_n\right)+w^2\frac{\rho_s\rho_n}{2\rho}\left(\nabla\cdot\mathbf{v}_n\right)+T\rho_s s\left(\nabla\cdot\mathbf{v}_n\right)+\rho_s\phi C_v T\left(\nabla\cdot\mathbf{v}_s\right)-w^2\frac{\rho_s\rho_n}{2\rho}\left(\nabla\cdot\mathbf{v}_s\right)-T\rho_s s\left(\nabla\cdot\mathbf{v}_s\right)\nabla T-\\+\rho C_v\left(\frac{\rho_n\mathbf{v}_n+\rho_s\mathbf{v}_s}{\rho}\right)-\nabla\cdot\left(k\nabla T\right)-A\rho_s\rho_n w^2\left(\mathbf{w}\cdot\mathbf{v}_n\right)+A\rho_s\rho_n w^2\left(\mathbf{w}\cdot\mathbf{v}_s\right)=\\q-\overline{\overline{\tau}}\cdot\nabla\cdot\mathbf{v}-\rho\phi C_v T\left(\mathbf{v}_n\cdot\nabla\frac{\rho_n}{\rho}\right)-\rho\phi C_v T\left(\mathbf{v}_s\cdot\nabla\frac{\rho_s}{\rho}\right)-T\left(\mathbf{w}\cdot\nabla\rho_s s\right)-w^2\left(\mathbf{w}\cdot\nabla\frac{\rho_s\rho_n}{2\rho}\right)\end{gathered}\tag{3.52}$$

Table 3.1: Final system of PDE for the thermodynamic state and the 3-D flow of the normal- and superfluid components in Helium II

4 NUMERICAL TECHNIQUES

4.1 Existing Numerical Simulations for Helium II

To support the development of superconductor and large-scale Helium cooling, a detailed and accurate modeling of Helium properties is required. The relevant properties of Helium II (such as viscosity, density, enthalpy, entropy, specific heat, Gorter-Mellink mutual friction etc.,) can be expressed as polynomial functions of pressure and temperature. Arp and McCarty generated a fundamental database, HEPAK, whose numerical output is consistent with observed Helium properties [69]. Numerical models frequently refer to this database.

An instructive example is a one-dimensional numerical model presented by Rao et al. to simulate a vertical, micron-wide, 15 cm long duct, referred to as the Gorter-Mellink duct [50]. The duct was heated at its bottom surface in order to simulate various transient internal-convection heat transfers, including forced convection [53]. The numerical approach relied on the finite element method, with the governing equations derived from the two-fluid model including the mutual-friction dissipation term in the energy equation. This approach differs from the simplified model in which the energy equation is based on the 1/3 power law dependence of the heat flux on temperature balance as introduced above and used by Dresner et al. [51]. Rao et al. used an explicit Adams-Bashforth scheme for the time integration of the convective term, while the Euler scheme was used for the other terms [52].

The relevant variables of the model are the normal and superfluid velocities and temperatures; pressure is assumed to be constant over the short vertical height. The interesting results obtained in this model included the illustration that Helium II velocities depend on second sound propagation and on thermal diffusion when the heat flux is lower or greater than 6 W/cm^2, respectively. Another study by Rao et al. compares numerical results obtained with the simplified model to the two-fluid model for both steady-state and forced convection heat transfer in Helium II [53]. In this second study, Rao et al. solved the governing equations with a fourth-order Runge-Kutta method and a control-volume-based finite difference method. The variables used were pressure, temperature and normal velocity. Here the convection term is utilized with the upwind scheme. The numerical results are in very good agreement with experimental results of Srinivasan and Hofmann [54].

Bottura et al. generated a one-dimensional package capable of simulating quench propagation in superconducting cables cooled by Helium II or normal Helium, using a single-fluid approximation [55][56]. Although the primary goal of this code was not to precisely apply the two-fluid model, it tested successfully against the experimental results of Srinivasan et al., for steady-state and for transient conditions in Helium II [52]. The variables chosen for this simulation were pressure, temperature and velocity. In this single-fluid approach, the counterflow heat transport term was added into the energy conservation balance. The governing equations were made discrete using a Taylor-Galerkin finite element algorithm and solved explicitly in time. The convenient formulation of this model has provided a base to our numerical formulation.

Xiang et al. presented a one-dimensional numerical model, developed as part of the design of the proposed TESLA accelerator, which is in support of simulating RF cavities cooled by the 2-phase flow of Helium II at 2K [57][58][59][60]. Although a rigorous geometrically correct model was developed and presented, taking into account the unique character of Helium II, the friction between the liquid and vapor phases was neglected. Pressure, temperature, and mass flow rates were obtained from the differential form for the one-dimensional energy and the conservation equations. Numerical results were validated against experimental results [61].

Ramadan et al. compared two-dimensional results obtained by simulation using a single-fluid model to a simulation using a two-fluid model, illustrating the effects of the counterflow between the two fluids [62][63]. In this earlier work, the momentum equations for the superfluid and the normal-fluid components were simplified by dropping the two largest terms, i.e. the thermo-mechanical effect and the Gorter-Mellink mutual friction term. Despite this seemingly drastic simplification, these results have shown the advantage of using a two-fluid model to treat the anomalous transport properties of Helium II. Using a similar approach Kitamura et al. addressed the two-dimensional problem by making the assumption that the thermo-mechanical effect was approximately equal to the Gorter-Mellink mutual friction term [64][65].

Finally, Tatsumoto et al., evaluated the heat transport phenomena for Helium II in a two-dimensional model by using the two-fluid model and energy dissipation based on the mutual friction between the superfluid and normal-fluid components [66][67]. A three-dimensional version was developed on the same principle [68]. The resulting computer code, SUPER-3D, uses the finite difference method with a staged grid system and the explicit integration of time. The pressure distribution is given by derivation of the continuity and the momentum equations using the first order upwind scheme. Afterwards, the temperature profile is obtained by solving the entropy equation using a modified Lax method. The code was tested against experimental data and also predicted the steady-state critical heat flux to a precision of about 9 % [66]. Although SUPER-3D is a very promising tool, the use of its algorithm is extremely demanding in terms of computing capacity. In contrast, 3DHeliumSolver, developed in this dissertation project, uses a more simplified approach and several carefully chosen approximations which allow much faster integrations and simulation.

4.2 The Finite Element (FE) Method

The numerical treatment of partial differential equation is, by itself, a vast subject. PDEs are the engine of computer analyses or simulations of continuous physical systems, and many different integration methods exist. In our research we have identified the finite element (FE) method, augmented with finite difference (FD) and upwinding, to improve the stability of the solution, and as a preferred approach to solving our two-fluid flow approximation.

1. Discrete domain Ω with simple preselected finite element-grid generations,
2. Derive the element equation from the governing equation using the variation formulation and the element interpolation function,
3. Obtain the matrix using numerical integration,

4. Assemble element equations to obtain an algebraic system,
5. Impose boundary conditions,
6. Solve the resulting system of equations.

More specifically, we also describe three-dimensional Helium II flow by implementing the numerical scheme outlined above.

The implementation as a software program which we call 3DHeliumSolver, consists of several Fortran procedures structured for solving a three-dimensional fluid flow problem, and is capable of integrating a set of partial differential equations applied to a sample geometry. The time integration implemented is based on the Beam-Warming finite difference algorithm [18]. For a given physical problem, space discretization and time integration necessarily lead to a non-linear algebraic system, which is then linearized. This permits us to trace the time evolution of each variable, corresponding to relevant degrees of freedom.

3DHeliumSolver makes use of parts of an existing one-dimensional code, THEA, whose PDE solver has been transformed to solve three-dimensional hydro- and thermo-dynamics problems. THEA is a commercial code, which provides one-dimensional Thermal, Hydraulic and Electric Analysis of superconducting cables [17]. For instance, THEA allows the calculation of the propagation of a quench on superconductor cables immersed in a Helium bath. The reason for choosing this existing 1-D solver was driven by the general form of the PDE considered. The architecture of THEA subroutines support the form of the general PDE that we aim to integrate. We only used the parts of the routines which solve partial differential equations in a one-dimensional system, rewriting them to handle three-dimensional finite elements. Then, we implemented partial differential equations for Helium II as derived in Chapter 3. The resulting 3DHeliumSolver is based on a three-dimensional Lagrangian finite element in space supplemented by Beam-Warming algorithm types in time.

Within this software framework, the PDE vector of unknowns (**u**) depends on the phenomena to be simulated. The PDEs are defined for the variable U, which contains parameters of the vector of unknowns. The PDEs are described by the element mesh, nodes, order of the elements and the nodes, initial and boundary conditions, time step and computing capacity. The number of unknowns in the system of equations defines the number of degrees of freedom in the problem.

4.3 Space Discretization in $\vec{\xi}$-space and $\vec{x}$-space

A modification of the space discretization was necessary to transform the one-dimensional solver into a 2-D, and then a 3-D, solver complying with our requirements. Interpolation functions and their derivatives are used to discretize the nodal variables and allow a conversion from parent (local) $\vec{\xi}$-space (ξ, η, ζ) to the physical space $\vec{x}$-space (x,y,z), with $\vec{x} = \sum_I \vec{x}_I N_I(\vec{\xi})$

Let us first consider a structure divided into finite elements. Let u_I designate a generic degree of freedom at the point I, and let $\tilde{u}(\vec{x},t)$ be an approximate solution of $u(\vec{x},t)$. The expansion series can then be written :

$$\tilde{u}(\vec{x},t) = \sum_I u_I N_I(\vec{x},t) \tag{4.1}$$

$$\tilde{u}(\vec{x}_I,t) = u_I \ . \tag{4.2}$$

The functions $N_I(\vec{x},t)$ are chosen as locally defined polynomials within each element and are equal to zero outside the element. Therefore, a shape function and its derivatives can be defined in both spaces using the associated Jacobian, $\overline{\overline{J}}$ defined by :

$$\overline{\overline{J}} = \begin{vmatrix} \frac{\partial \xi}{\partial x} & \frac{\partial \eta}{\partial x} & \frac{\partial \zeta}{\partial x} \\ \frac{\partial \xi}{\partial y} & \frac{\partial \eta}{\partial y} & \frac{\partial \zeta}{\partial y} \\ \frac{\partial \xi}{\partial z} & \frac{\partial \eta}{\partial z} & \frac{\partial \zeta}{\partial z} \end{vmatrix} \text{ and } \overline{\overline{J}}^{-1} = \begin{vmatrix} \frac{\partial x}{\partial \xi} & \frac{\partial y}{\partial \xi} & \frac{\partial z}{\partial \xi} \\ \frac{\partial x}{\partial \eta} & \frac{\partial y}{\partial \eta} & \frac{\partial z}{\partial \eta} \\ \frac{\partial x}{\partial \zeta} & \frac{\partial y}{\partial \zeta} & \frac{\partial z}{\partial \zeta} \end{vmatrix},$$

where ;

$$\frac{\partial x}{\partial \xi} = \sum x_I \frac{\partial N_I}{\partial \xi}$$

$$\frac{\partial y}{\partial \zeta} = \sum y_I \frac{\partial N_I}{\partial \zeta}......$$

As in standard iso-parametric element theory, the gradient of the interpolation functions in the physical $\vec{x}$-space is derived from the gradient in the parent $\vec{\xi}$-space as follows :

$$\overrightarrow{\nabla_x} N_I(\vec{x}) = \overline{\overline{J}}\,\overrightarrow{\nabla_\xi} N_I(\vec{\xi}) \qquad (4.3)$$

An frequently-used method to solve PDE systems based on the weak formulation (or method of weighted residual, W) is Green's theorem :

$$\int_\Omega W\vec{\nabla}\cdot\left(\vec{\nabla} k u\right) d\Omega = -k\int_\Omega \left(\vec{\nabla} u\cdot\vec{\nabla} W\right) d\Omega + \oint_\Gamma k\frac{\partial u}{\partial n} W d\Gamma \qquad (4.4)$$

Using Gaussian quadrature for a three-dimensional space with cubic volumes or rectangular shapes, numerical integration yields :

$$\int_{-1}^{1}\int_{-1}^{1}\int_{-1}^{1} f(\xi,\eta,\zeta) d\xi\cdot d\eta\cdot d\zeta = \sum_{i=1}^{n}\sum_{j=1}^{n}\sum_{k=1}^{n} H_i H_j H_k f(\xi_i,\eta_j,\zeta_k) \qquad (4.5)$$

In practice, we implemented “hard-coded” Gauss and Keast points for the quadrilateral and tetrahedral finite element definitions, respectively.

4.4 Space Discretization Method for 3DHeliumSolver

For discretization in space we subdivide the domain into an arbitrary number of finite elements. Each node of the mesh has a number of degrees of freedom (DOF's) equal to the total number of variables in the system.

We approximate the system variables using shape functions **N** :

$$\mathbf{u} \approx \mathbf{NU} \qquad (4.6)$$

where **U** is the vector formed by the values of the variables at the nodes of the finite element mesh. The space discretization is obtained by weighted integration, using weight functions equal to the shape functions. As a result the system of PDE's gives origin to the following system of ODE's :

$$\mathbf{M}\frac{\partial \mathbf{U}}{\partial t} + [\mathbf{A} + \mathbf{G} + \mathbf{S}]\mathbf{U} = \mathbf{Q} \tag{4.7}$$

where the matrices appearing above are obtained by assembling the element contributions of the following integrals :

$$\mathbf{M} = \int \mathbf{N}^T \mathbf{m} \mathbf{N}\, dx \tag{4.8}$$

$$\mathbf{A} = \int \mathbf{N}^T \mathbf{a} \frac{\partial \mathbf{N}}{\partial x} dx \tag{4.9}$$

$$\mathbf{G} = \int \frac{\partial \mathbf{N}^T}{\partial x} \mathbf{g} \frac{\partial \mathbf{N}}{\partial x}\, dx \tag{4.10}$$

$$\mathbf{S} = \int \mathbf{N}^T \mathbf{s} \mathbf{N}\; dx \tag{4.11}$$

$$\mathbf{Q} = \int \mathbf{N}^T \mathbf{q}\, dx \tag{4.12}$$

The integrals are performed using Gaussian integration, which is necessary to deal with the non-linearities in the matrices of coefficients, as well as variable order interpolation in the mesh.

4.5 Time Integration Method for 3DHeliumSolver

The system of ODE's listed in Chapter 3, Table 3.1 is solved with a modified multi-step algorithm of the Beam and Warming (BW) family [18]. We wrote the system in the following simpler form :

$$\mathbf{M}\frac{\partial \mathbf{U}}{\partial t} + \mathbf{H}\mathbf{U} = \mathbf{Q} \tag{4.13}$$

Here we have introduced the matrix **H,** equal to the sum of the matrices **A**, **G** and **S**. The time discretization is performed as follows ;

$$(1+\xi)\mathbf{M}\frac{\mathbf{U}^{n+1}-\mathbf{U}^{n}}{\Delta t^{n}}-\xi\mathbf{M}\frac{\mathbf{U}^{n}-\mathbf{U}^{n-1}}{\Delta t^{n-1}}+\theta\mathbf{H}\left(\mathbf{U}^{n+1}-\mathbf{U}^{n}\right)+\mathbf{H}\mathbf{U}^{n}+\phi\mathbf{H}\left(\mathbf{U}^{n}-\mathbf{U}^{n-1}\right)=\mathbf{Q} \quad (4.14)$$

where the superscripts *n-1*, *n* and *n+1* indicate variables at corresponding time stations during integration, and Δt^{n-1} and Δt^{n} are the time steps from time stations *n-1* to *n* and *n* to *n+1,* respectively. To linearize the solution of Eq. 4.14 all matrices and loads are evaluated from the known value of $\mathbf{U}^{n}$ at time t^{*}:

$$t^{*}=t^{n}+\theta\Delta t^{n}-\phi\Delta t^{n-1} \quad (4.15)$$

The increments of the variable **U** between the time stations are :

$$\Delta\mathbf{U}^{n-1}=\mathbf{U}^{n}-\mathbf{U}^{n-1} \quad (4.16)$$

$$\Delta\mathbf{U}^{n}=\mathbf{U}^{n+1}-\mathbf{U}^{n} \quad (4.17)$$

and we rewrite the system of algebraic equations of Eq. 4.14 as follows :

$$\left[(1+\xi)\mathbf{M}+\theta\Delta t^{n}\mathbf{H}\right]\Delta\mathbf{U}^{n}=\left[\xi\frac{\Delta t^{n}}{\Delta t^{n-1}}\mathbf{M}-\phi\Delta t^{n}\mathbf{H}\right]\Delta\mathbf{U}^{n-1}-\Delta t^{n}\mathbf{H}\mathbf{U}^{n}+\Delta t^{n}\mathbf{Q} \quad (4.18).$$

Alternatively, we can write:

$$(1+\xi)U^{n+2}-(1+2\xi)U^{n+1}+\xi U^{n}=\Delta t(\theta H^{n+2}+(1-\theta-\phi)H^{n+1}-\phi H^{n}) \quad (4.19)$$

where H^{n} is the weight coefficient at time *n* [18].

The given algorithm is modified from the typical BW one, because we consider an approximate matrix as being equivalent to the matrix at the previous time, whereas the time step is progressing in space. This technique can be referred to as a “pseudo-implicit” method, which has the advantage that the solutions are unconditionally stable. Every degree of freedom is listed at any time t and the matrices are full. Implicit methods

The parameters θ, ξ and ϕ, must be chosen so that the method referring to the modified two-step BW-type algorithms is consistent and achieves the desired accuracy [18]. Depending on the choice of the set of parameters, several known numerical schemes can be obtained. A list of possible choices is given in Table 4.1, together with the order of numerical accuracy achieved.

Table 4.1: Choice of numerical parameters for the time integration scheme and corresponding time accuracy

Method #	Algorithm		Order	θ	ξ	ϕ
1	Euler Backward	Implicit	1	1	0	0
2	Backward Euler (Galerkin)	Implicit	2			
3	Crank-Nicholson (one-step trapezoidal)	Implicit	2	1/2	0	0
4	Backward differencing	Implicit	2	1	1/2	
5	3rd order	Implicit	3	1/3	-1/6	
6	Adams-Moulton	Implicit	3	5/12	0	1/12
7	Milne	Implicit	4	1/6	-1/2	-1/6

All matrix and vector operations called by the time integration routine reside in a set of mathematical libraries available in the one-dimensional THEA code. We defined a relative error by computing the difference between the solution for the time integration over the step $t \rightarrow t + \Delta t$ to the step $t \rightarrow t+\Delta t/2 \rightarrow t + \Delta t$.

The main task was to modify the given THEA routines, according to the methods described above, to implement shape functions for three-dimensional finite elements, their local and global derivatives, the associated Jacobian and its determinant.

4.6 Vector Form for the PDE System

At this stage of the development of 3DHeliumSolver, we have defined our problem in general terms using a matrix and operator formulation. This allowed us to simplify the formalism at the level of the implementation of the code. The conservation laws that have been chosen to model the two-fluid flow were put in the general matrix representation for the partial differential equation system.

The first three-dimensional mesh generated considered tetrahedral finite elements. The Jacobian of the associated interpolation functions was calculated using Eq. 4.3. Its determinant and matrix operations were then implemented in the three-dimensional code. Gaussian points for tetrahedral finite elements were “hard-coded” and used in order to obtain integrations and expansion series as listed in Eq. 4.5.

With all equations now in an appropriate form for numerical treatment, we proceed to express these equations in a compact vector form, which is symmetric and convenient for simplifying computer code.

The problem is to solve the two-fluid approximation equations of Table 3.1 for which the PDE form is :

$$\overline{\overline{\mathbf{m}}}\frac{\partial \mathbf{u}}{\partial t} + \overline{\overline{\mathbf{a}}}\nabla \cdot \mathbf{u} + \nabla \cdot \left(\overline{\overline{\mathbf{g}}}\nabla \cdot \mathbf{u}\right) + \overline{\overline{\mathbf{s}}}\mathbf{u} = \mathbf{q} \qquad (4.20)$$

where $\overline{\overline{\mathbf{m}}}$ is a mass matrix, $\overline{\overline{\mathbf{a}}}$ is the advection matrix (with components $\overline{\overline{\mathbf{a}}}_x$, $\overline{\overline{\mathbf{a}}}_y$, and $\overline{\overline{\mathbf{a}}}_z$), $\overline{\overline{\mathbf{g}}}$ is the diffusion matrix, $\overline{\overline{\mathbf{s}}}$ the source matrix and **q** the forcing vector. The source term associated with the matrix $\overline{\overline{\mathbf{s}}}$ introduces non-linearity into the problem that usually requires implicit treatment to achieve numerical stability. The vector of unknowns (**u)** is defined here in general term and can be specifically written to contain terms describing the motion and the state of the superfluid flow, as described below.

Eq. 4.20 is a generic, parabolic-hyperbolic system of partial differential equations for the vector-of -unknown’s **u**. In the specific case of Eqs. 3.49 through 3.52, the vector **u** is given by :

$$\mathbf{u} = \begin{bmatrix} p \\ \mathbf{v}_n \\ \mathbf{v}_s \\ T \end{bmatrix} \qquad (4.21)$$

Matrices and vectors are found by identifying terms with the final PDE system in Table 3.1. Specifically:

$$\overline{\overline{\mathbf{m}}} = \begin{bmatrix} 1 & 0 & 0 & 0 \\ 0 & \rho_n & 0 & 0 \\ 0 & 0 & \rho_s & 0 \\ 0 & 0 & 0 & \rho C_v \end{bmatrix} \tag{4.22}$$

$$\overline{\overline{\mathbf{a}}} = \begin{bmatrix} \dfrac{\rho_n \mathbf{v}_n + \rho_s \mathbf{v}_s}{\rho} & \rho_n c^2 + \phi T \rho_s s + \phi w^2 \dfrac{\rho_s \rho_n}{2\rho} & \rho_s c^2 - \phi T \rho_s s - \phi w^2 \dfrac{\rho_s \rho_n}{2\rho} & 0 \\ \dfrac{\rho_n}{\rho} & \rho_n \mathbf{v}_n + \dfrac{\rho_s \rho_n}{\rho} \mathbf{w} & -\dfrac{\rho_s \rho_n}{\rho} \mathbf{w} & \rho_s s \\ \dfrac{\rho_s}{\rho} & -\dfrac{\rho_s \rho_n}{\rho} \mathbf{w} & \rho_s \mathbf{v}_s + \dfrac{\rho_s \rho_n}{\rho} \mathbf{w} & -\rho_s s \\ 0 & \rho_n \phi C_v T + T \rho_s s + w^2 \dfrac{\rho_s \rho_n}{2\rho} & \rho_s \phi C_v T - T \rho_s s - w^2 \dfrac{\rho_s \rho_n}{2\rho} & (\rho_n \mathbf{v}_n + \rho_s \mathbf{v}_s) C_v \end{bmatrix} \tag{4.23}$$

$$\overline{\overline{\mathbf{g}}} = \begin{bmatrix} 0 & 0 & 0 & \phi k \\ 0 & 0 & 0 & 0 \\ 0 & 0 & 0 & 0 \\ 0 & 0 & 0 & k \end{bmatrix} \tag{4.24}$$

$$\overline{\overline{\mathbf{s}}} = \begin{bmatrix} 0 & -\phi A \rho_s \rho_n w^2 \mathbf{w} & \phi A \rho_s \rho_n w^2 \mathbf{w} & 0 \\ 0 & A \rho_s \rho_n w^2 & -A \rho_s \rho_n w^2 & 0 \\ 0 & -A \rho_s \rho_n w^2 & A \rho_s \rho_n w^2 & 0 \\ 0 & -A \rho_s \rho_n w^2 \mathbf{w} & A \rho_s \rho_n w^2 \mathbf{w} & 0 \end{bmatrix} \tag{4.25}$$

$$\mathbf{q} = \begin{bmatrix} \phi q - \phi \overline{\overline{\tau}} \cdot \nabla \cdot \mathbf{v}_n - \rho c^2 \left(\mathbf{v}_n \cdot \nabla \dfrac{\rho_n}{\rho} \right) - \rho c^2 \left(\mathbf{v}_s \cdot \nabla \dfrac{\rho_s}{\rho} \right) - \phi T (\mathbf{w} \cdot \nabla \rho_s s) - \phi w^2 \left(\mathbf{w} \cdot \nabla \dfrac{\rho_s \rho_n}{2\rho} \right) \\ -\nabla \cdot \overline{\overline{\tau}} + \rho_n \mathbf{g} \\ \rho_s \mathbf{g} \\ q - \overline{\overline{\tau}} \cdot \nabla \cdot \mathbf{v} - \rho \phi C_v T \left(\mathbf{v}_n \cdot \nabla \dfrac{\rho_n}{\rho} \right) - \rho \phi C_v T \left(\mathbf{v}_s \cdot \nabla \dfrac{\rho_s}{\rho} \right) - T (\mathbf{w} \cdot \nabla \rho_s s) - w^2 \left(\mathbf{w} \cdot \nabla \dfrac{\rho_s \rho_n}{2\rho} \right) \end{bmatrix} \tag{4.26}$$

The system of Eq. 4.20 is written using a weighted residual at the nodes. If the weight functions are equivalent to the shape functions, then we obtain the following set of ordinary differential equations in time ;

$$M \frac{\partial U}{\partial t} + (A + G - S) U = Q \tag{4.27}$$

Here the matrices are the discrete versions of the PDE system matrices, obtained by integration over the finite elements (weak formulation of the problem). The vector of unknowns U contains values of pressure, normal velocities, superfluid velocities and temperature at each node of the finite element mesh. These matrices are obtained by integration over each finite element and assembly over the mesh. The matrices are defined by

$$\mathrm{M}_{\mathrm{IJ}} = \int_{\Omega \mathrm{J}} \mathrm{N}_{\mathrm{I}} \mathrm{m}_{\mathrm{IJ}} \mathrm{N}_{\mathrm{J}} \mathrm{d}\Omega \tag{4.28}$$

$$\mathrm{A}_{\mathrm{IJ}} = \int_{\Omega \mathrm{J}} \mathrm{N}_{\mathrm{I}} \mathrm{a}_{\mathrm{IJ}} \nabla \mathrm{N}_{\mathrm{J}} \mathrm{d}\Omega \tag{4.29}$$

$$\mathrm{G}_{\mathrm{IJ}} = \int_{\Omega \mathrm{J}} \nabla \mathrm{N}_{\mathrm{I}} \mathrm{g}_{\mathrm{IJ}} \nabla \mathrm{N}_{\mathrm{J}} \mathrm{d}\Omega \tag{4.30}$$

$$\mathrm{S}_{\mathrm{IJ}} = \int_{\Omega \mathrm{J}} \mathrm{N}_{\mathrm{I}} \mathrm{s}_{\mathrm{IJ}} \mathrm{N}_{\mathrm{J}} \mathrm{d}\Omega \tag{4.31}$$

$$Q_J = \int_{\Omega J} \nabla N_J q_J \, d\Omega \tag{4.32}$$

4.7 Expression of Thermo-Physical Properties

The thermo-physical properties of He II, have a strong non-linear dependence on temperature. The handling of these quantities is primordial to controlling numerical instabilities. Every property value is called by 3DHeliumSolver from an existing library [69].

Due to the importance of the Gorter-Mellink coefficient (A_{GM}), we use discrete values extracted from Hepak to build a specific expression as a 12th order polynomial for $A_{GM}(T)=\sum_0^{12} a_i T^i$, where the coefficients are defined as per Table 4.2:

Table 4.2: Coefficient for the polynomial fit of the Gorter-Mellink coefficient

a0	-2.15579E+11
a1	1.2738E+12
a2	-3.32561E+12
a3	4.98305E+12
a4	-4.60071E+12

a5	2.50166E+12
a6	-5.02179E+11
a7	-3.3587E+11
a8	3.30421E+11
a9	-1.37726E+11

a10	32840174914
a11	-4365737229
a12	252790501.1

A similar expression has been used elsewhere [70]. Fig. 4.1 shows the fit of the Gorter-Mellink coefficient used in the numerical calculations.

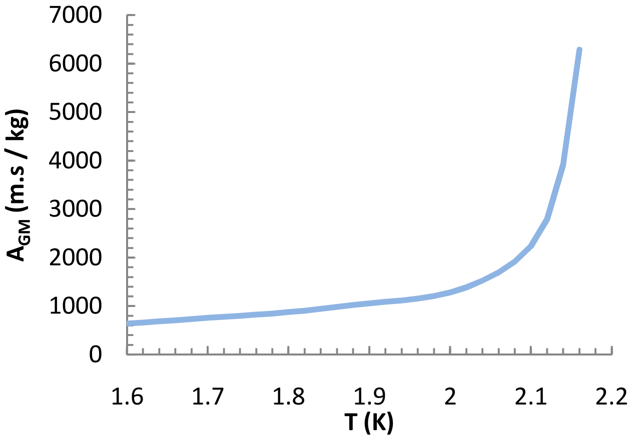

Figure 4.1: Fit of the 12th order for the Gorter-Mellink coefficient, A_{GM}

5 RESULTS USING 3DHELIUMSOLVER

We present here the results from a performing code, based on the algorithms developed in Chapter 3. This new tool, called 3DHeliumSolver, is based on the modification of an existing one-dimensional PDE solver. The current code modifications provide the possibility to look up fluid or material properties from an existing database.

In Section 5.1, we emphasize the scaling analysis w.r.t. the PDE system summarized in Table 3.1. This analysis provides us with a friendlier PDE, whose coefficient can be directly implemented in the new 3DHeliumSolver.

The following chapters show the results obtained using the friendly PDE system to simulate the Helium II in the two-fluid flow problem. It is worth noticing that a staged approach has been used to develop 3DHeliumSolver. First we evaluate the performance of the code for simple time dependent heat conduction in order to validate the new 3-D space integration algorithms and review the numerical stability of our tool. This well-behaved solution permits us to examine the convergence of the code with respect to seven different time discretization technique based on the Beam-Warming finite difference algorithm family i s. Then we studied the interesting and numerically challenging phenomena of transient convection-diffusion. The main difficulty in the integration comes from the first order terms inside the hyperbolic equations, corresponding physically to the vanishing viscosity of the super-fluid component of Helium II. These terms generate important instabilities. Following the common approach, we utilize an artificial diffusion and examine code behavior through the whole spectrum of the Peclet number Pe (inversely proportional to the coefficient of artificial diffusion), where 0 and infinity represent pure diffusion and pure convection respectively. We show that the integration outcomes and stability are improved by this technique. We studied Euler flow conditions and the influence of the viscosity, respectively. This last section directly leads to the simulation of Helium II behavior.

In the light of the scaling analysis, we can implement the simplified PDE in the 3DHeliumSolver, in order to model as accurately as possible the two-fluid model approximation. Several test cases are considered to validate the 3Dsolver and the choice of the PDE. We have benchmarked the new PDEsolver using problem, which can be directly verified by the theory. For this purpose, we have reproduced the unique property exhibited by the Helium II properties, i.e. the propagation of the second sound. The influence of the fluctuation of the entropy is imbedded in the new PDE system. 1-D and 2-D analyses were conducted and results are illustrated in chapter 5.4.

A second fundamental characteristic of Helium II behavior lays in the existence of the thermal counterflow, i.e. heat transfer with no fluid bulk velocity. 2-D and 3-D analyses are studied for a closed channel and results are illustrated in chapters 5.5 to 5.7.

5.1 Scaling Analysis

The phenomenological description of the Helium II dynamics in the two-fluid model is modeled after the set of Eqs. 3.49 to 3.52, Table 3.1. Each term has been qualified in the previous chapters. We need now to quantify each of them in order to understand which terms are predominant in this dynamics model. For this matter we have completed a scaling analysis, using the following dimensionless variable listed in Table 5.1:

Table 5.1: List of the dimensionless variables – Expressions

$T = T_o T^*$	$p = p_o p^*$	$r = r_o r^*$	$t = t_o t^* = \frac{r_o}{v_o} t^*$
$v = v_o v^*$	$v_n = v_{no} {v_n}^*$	$v_s = v_{so} {v_s}^*$	$w = (v_n - v_s) = w_o w^*$
$\rho = \rho_o \rho^*$	$\rho_n = \rho_{no} {\rho_n}^*$	$\rho_s = \rho_{so} {\rho_s}^*$	$s = s_o s^*$
$\tau = \tau_o \tau^*$			

where the index -0 indicates the fluid quantities at a temperature and pressure of 1.9 K and 0.1 MPa, respectively. The index * indicates the unit of the given quantity. After a preliminary scaling analysis, it has been shown that the orders of magnitude of the different densities ($\rho_{no}, \rho_{so}, \rho_o$) are equivalent to ρ_o. Similarly, the orders of magnitude of the fluid velocities (v_{so}, v_{no}, w_o, v_o) are equivalent to v_o.

Temperature, pressure, distance, time, densities, entropy, viscous effect, velocities are listed in Table 5.2.

Table 5.2: Helium II properties at 1.9 K, 0.1 MPa (used in scaling analysis)

Quantity	To	po	ro	to	vo	□o	So	□o
Value	1.9	0.1	0.01	0.1	0.1	100	733	10-6
Unit	K	MPa	m	sec	m/s	kg/m3	Joule/m.K	P.sec

5.1.1 Equation of Mass Conservation: *p*

The scaling analysis for the pressure equation uses Eq. 3.49 and the description of the different variables above in order to identify dimensionless numbers and seize their importance in the flow mechanism. The dimensionless pressure equation can be written as follows:

$$\frac{\partial p^*}{\partial t^*}+\left(\frac{\rho_n^*\mathbf{v}_n^*+\rho_s^*\mathbf{v}_s^*}{\rho^*}\right)\frac{\partial p^*}{\partial r^*}+CPv1\left[\rho_n^*\frac{\partial \mathbf{v}_n^*}{\partial r^*}+\rho_s^*\frac{\partial \mathbf{v}_s^*}{\partial r^*}\right]+CPv2\frac{w^{*2}\rho_s^*\rho_n^*}{2\rho^*}\left[\frac{\partial \mathbf{v}_n^*}{\partial r^*}-\frac{\partial \mathbf{v}_s^*}{\partial r^*}\right]+CPv3\cdot T^*\rho_s^*s^*\left[\frac{\partial \mathbf{v}_n^*}{\partial r^*}-\frac{\partial \mathbf{v}_s^*}{\partial r^*}\right]$$
$$-CPT\frac{\partial^2 T^*}{\partial r^{*2}}-CPv4\cdot\rho_s^*\rho_n^*w^{*2}\mathbf{w}^*\left[\mathbf{v}_n^*-\mathbf{v}_s^*\right]=C\mathbf{Pr}0-C\mathbf{Pr}1\cdot\overline{\overline{\tau}}\cdot\frac{\partial \mathbf{v}_n^*}{\partial r^*}$$
$$-CPv1\rho^*\left[v_n^*\frac{\partial\left(\frac{\rho_n^*}{\rho^*}\right)}{\partial r^*}+v_s^*\frac{\partial\left(\frac{\rho_s^*}{\rho^*}\right)}{\partial r^*}\right]-C\mathbf{Pr}2\cdot T^*\mathbf{w}^*\frac{\partial\rho_s^*s^*}{\partial r^*}-C\mathbf{Pr}3\cdot w^{*2}\mathbf{w}^*\frac{\partial\left(\frac{\rho_s^*\rho_n^*}{2\rho^*}\right)}{\partial r^*} \tag{5.1}$$

The Eq. 5.1 obtained after variables substitution has a dimension zero, supporting the initial formulation of the problem. After quantification, each dimensionless quantity is listed in Table 5.3 and the influence of each term can then be compared to the original pressure.

Table 5.3: Dimensionless quantities for the mass conservation

$CPv1=\frac{\rho_0 c^2}{p_0}$	$CPv3=\frac{\phi T_o\rho_o s_o}{P_o}$	$CPv4=\frac{\phi A\rho_o^2 w_o^3 r_o}{P_o}$	$CPv2=\frac{\phi\rho_o w_o{}^2}{P_o}$	$CPT=\frac{\phi k_o T_o}{r_o v_o P_o}$
40	-0.2	-1.5 10^{-4}	-1.5 10^{-6}	0
$C\,\mathrm{Pr}\,2=\frac{\phi T_o\rho_o s_o w_o}{P_o v_o}$	$C\,\mathrm{Pr}\,3=\frac{\phi\rho_o w_o^3}{P_o v_o}$	$C\,\mathrm{Pr}\,1=\frac{\phi\tau_o}{P_o}$	$C\,\mathrm{Pr}\,0=\frac{\phi q t_o}{P_o}$	
-0.2	-1.5 10^{-6}	-1.5 10^{-10}	0	

As expected, the main driver of the pressure wave propagation is the velocity field. The convection of the mass and the first sound decompression of the density dominate the mechanism of the Helium II flow. The pressure wave will propagate at the speed of the first sound in a Helium II channel. The fluid density can be assumed constant. Hence, we can consider that the fluid is incompressible.

For the sake of describing transient behavior, and to maintain the stability and nature of the PDE solver, we keep the derivative in time and the conduction term (which is only different from zero above T_λ). The term associated to the exchange of entropy is also kept.

The inertia term, C*Pr*1, describing the influence of the viscous effect is neglected. Surprisingly the mutual friction term can also be dropped from the equations.

According to the scaling analysis, we simplify the governing equation Eq. 3.49, as follows :

$$\rho_n c^2 \nabla \cdot \mathbf{v}_n + \rho_s c^2 \nabla \cdot \mathbf{v}_s + \frac{\partial p}{\partial t} + \left(\frac{\rho_n \mathbf{v}_n + \rho_s \mathbf{v}_s}{\rho} \right) \cdot \nabla p + \phi T \rho_s s \nabla \cdot \mathbf{v}_n - \phi T \rho_s s \nabla \cdot \mathbf{v}_s - \nabla \cdot \left(\phi k \nabla T \right) = \phi q \tag{5.2}$$

5.1.2 Equation of Momentum Conservation for the Normal Velocity: $\mathbf{v}_n$

We now consider the momentum conservation for the normal velocity, $\mathbf{v}_n$ as shown in Eq. 3.50. As for the mass conservation, we can identify dimensionless numbers and estimate their weight in the final equation. The dimensionless equation can be written as follows :

$$\rho_n^* \frac{\partial \mathbf{v}_n^*}{\partial t^*} + CVnp \cdot \frac{\rho_n^*}{\rho^*} \frac{\partial p^*}{\partial r^*} + \rho_n^* \mathbf{v}_n^* \frac{\partial \mathbf{v}_n^*}{\partial r^*} + CVnv1 \frac{\rho_s^* \rho_n^*}{\rho^*} \mathbf{w}^* \left(\frac{\partial \mathbf{v}_n^*}{\partial r^*} - \frac{\partial \mathbf{v}_s^*}{\partial r^*} \right) + CVnT \cdot \rho_s^* s^* \frac{\partial T^*}{\partial r^*}$$
$$+ CVnv2 \cdot \rho_s^* \rho_n^* w^{*2} (\mathbf{v}_n^* - \mathbf{v}_s^*) = CVnr1 \frac{\partial \overline{\overline{\tau}}^*}{\partial r^*} + CVnr2 \cdot \rho_n^* \tag{5.3}$$

where the dimensionless quantities are identified and listed in Table 5.4.

Table 5.4: Dimensionless quantities for the normal velocity equation

$CVnT = \frac{T_o s_o}{v_{no}^2}$	$CVnP = \frac{P_o}{\rho_o v_{no}^2}$	$CVnV2 = A\rho_o w_o^2 t_o$	$CVnV1 = \frac{w_o}{v_{no}}$
1.4 10^5	10^5	10^2	1

$CVnR2 = \frac{gt_o}{vo}$	$CVnR1 = -\frac{\tau_o}{\rho_o v_{no}^2}$
10	-10^{-6}

As expected, the main contributors to the velocity field are the pressure and the temperature gradients. The importance of the temperature gradient is symbolized by the thermo-mechanical effect or fountain effect observed in He II. In a traditional fluid, pressure would be the only driver. The inertia term, CVnR1, showing the influence of the viscous effect, is neglected. Similarly, the gravity term is not considered in the result of the following chapter.

For the sake of algorithm stability, we keep the transient terms. Terms expressing the mutual friction are also implemented in the final PDE. Hence, after scaling analysis the governing Eq. 3.50 can be simplified as follows :

$$\frac{\rho_n}{\rho}\nabla p + \rho_s s\nabla T + \rho_n \frac{\partial \mathbf{v}_n}{\partial t} + A\rho_s\rho_n w^2 \mathbf{v}_n - A\rho_s\rho_n w^2 \mathbf{v}_s = \rho_n \mathbf{g} \tag{5.4}$$

5.1.3 Equation of Momentum Conservation for the Superfluid Component: $\mathbf{v}_s$

The identical approach is taken when we consider the momentum conservation for the superfluid velocity component, and the observations are similar. Using Eq. 3.51 and the description of the different variables above, we identify dimensionless numbers by writing the following Eq. 5.5 and Table 5.5 :

$$\rho_s^* \frac{\partial \mathbf{v}_s^*}{\partial t^*} + CVsp\frac{\rho_s^*}{\rho^*}\frac{\partial P^*}{\partial r^*} - CVsv1\frac{\rho_s^*\rho_n^*}{\rho^*}\mathbf{w}^*\left[\frac{\partial \mathbf{v}_n^*}{\partial r^*} - \frac{\partial \mathbf{v}_s^*}{\partial r^*}\right] + \rho_s^*\mathbf{v}_s^*\frac{\partial \mathbf{v}_s^*}{\partial r^*} - CVsT\cdot\rho_s^* s^*\frac{\partial T^*}{\partial r^*}$$
$$- CVsv2\cdot\rho_s^*\rho_n w^{*2}\left(\mathbf{v}_n^* - \mathbf{v}_s^*\right) = CVsr1 \tag{5.5}$$

Table 5.5: Dimensionless quantities for the momentum conservation for the superfluid velocity

$CVsP=\dfrac{P_o}{\rho_o v_{so}^2}$	$CVsT=\dfrac{T_o s_o}{v_{so}^2}$	$CVsV2=A\rho_o w_o^2 t_o$	$CVsV1=\dfrac{w_o}{v_{so}}$
10^5	$1.4\ 10^5$	10^2	1

$CVsR1=\dfrac{\mathbf{g}t_o}{v_{so}}$
10

Here too, we observe that the contributors to the superfluid velocity field are the pressure and the temperature gradients. As for the total velocity behavior, the superfluid velocity is mainly influenced by the thermo-mechanical effect and by the pressure gradient. It is therefore acceptable to simplify Eq. 3.51 to :

$$\frac{\rho_s}{\rho}\nabla p-\rho_s s\nabla T+\rho_s\frac{\partial \mathbf{v}_s}{\partial t}-A\rho_s\rho_n w^2\mathbf{v}_n+A\rho_s\rho_n w^2\mathbf{v}_s=\rho_s\mathbf{g} \tag{5.6}$$

5.1.4 Equation of Energy Conservation: T

Finally, we consider the energy conservation of the Helium II, Eq. 3.52. If we substitute the different terms of the equation with the dimensionless variables introduced earlier, we obtain the following dimensionless equation :

$$\begin{aligned}&\rho^*\frac{\partial T^*}{\partial t^*}+\phi T^*\left(\rho_n^*\frac{\partial \mathbf{v}_n^*}{\partial r^*}+\rho_s^*\frac{\partial \mathbf{v}_s^*}{\partial r^*}\right)-CTv1\cdot w^{*2}\frac{\rho_s^*\rho_n^*}{\rho^*}\left(\frac{\partial \mathbf{v}_n^*}{\partial r^*}-\frac{\partial \mathbf{v}_s^*}{\partial r^*}\right)+CTv2\cdot T^*\rho_s^* s^*\left(\frac{\partial \mathbf{v}_n^*}{\partial r^*}-\frac{\partial \mathbf{v}_s^*}{\partial r^*}\right)\\&+\rho^*\left(\frac{\rho_n^*\mathbf{v}_n^*+\rho_s^*\mathbf{v}_s^*}{\rho^*}\right)\frac{\partial T^*}{\partial r^*}-CTT\frac{\partial^2 T^*}{\partial r^{*2}}-CTv3\cdot\rho_s^*\rho_n^* w^{*2}\mathbf{w}^*(\mathbf{v}_n^*-\mathbf{v}_s^*)=CTr1\cdot q^*\\&-CTr2\cdot\overline{\overline{\tau}}\frac{\partial \mathbf{v}^*}{\partial r^*}-\phi\rho^* T^*\left(\mathbf{v}_n^*\frac{\partial\left(\frac{\rho_n^*}{\rho^*}\right)}{\partial r^*}-\mathbf{v}_s^*\frac{\partial\left(\frac{\rho_s^*}{\rho^*}\right)}{\partial r^*}\right)-CTr3\cdot T^*\mathbf{w}^*\left(\frac{s^*\partial\rho_s^*}{\partial r^*}+\frac{\rho_s^*\partial s^*}{\partial r^*}\right)-CTr4\cdot\mathbf{w}^*\mathbf{w}^{*2}\frac{\partial\left(\frac{\rho_s^*\rho_n^*}{2\rho^*}\right)}{\partial r^*}\end{aligned} \tag{5.7}$$

This dimensionless equation includes numerous quantities. The temperature transient represents an important impact to the dynamism of the flow. As for the pressure equation, the term associated with the exchange of entropy between the normal and the superfluid components is important. The dimensionless quantities are compared in Table 5.6.

Table 5.6: Dimensionless quantities for the energy balance

$CTv2 = \frac{S_o}{Cv}$	$CTv3 = \frac{A\rho_o w_o^3 r_o}{CvT_o}$	$CTv1 = \frac{w_o^2}{2CvT_o}$	$CTT = \frac{k_o}{Cv\rho_o v_o r_o}$
0.2	$1.4\ 10^{-4}$	$7\ 10^{-7}$	0
$CTr3 = \left\{\frac{s_o \mathrm{w}_o}{v_o C_v}\right\}$	$CTr4 = \left\{\frac{w_o^3}{C_v T_o v_o}\right\}$	$CTr2 = \left\{\frac{\tau_o}{Cv\rho_o T_o}\right\}$	$CTr1 = \left\{\frac{q_o t_o}{Cv\rho_o T_o}\right\}$
0.2	$1.3\ 10^{-6}$	$1.3\ 10^{-12}$	0

We see that the temperature variation is weakly related to energy dissipation due to the Gorter-Mellink effect and is independent of the pressure gradient. The transient phenomena influence the mechanism of the Helium II mass and heat transfer. As for the pressure equation, we note that the entropy exchange, the convection term and the effect of expansion/compression are not negligible. Surprisingly, the effect of the energy exchange between the two components, CTv1, can be neglected.

Following the same guiding principle as for the pressure equation, we obtain the following simplification :

$$\rho C_v \frac{\partial T}{\partial t} + \rho_n \phi C_v T \nabla \cdot \mathbf{v}_n + \rho_s \phi C_v T \nabla \cdot \mathbf{v}_s + \rho C_v \left(\frac{\rho_n \mathbf{v}_n + \rho_s \mathbf{v}_s}{\rho} \right) \cdot \nabla T + T \rho_s s \nabla \cdot \mathbf{v}_n - T \rho_s s \nabla \cdot \mathbf{v}_s$$

$$- \nabla \cdot \left(k \nabla T \right) = q \qquad \textbf{(5.8)}$$

5.2 General PDE Used to Model Helium II Flow

For the sake of interpretation, we have substituted the variable $\mathbf{v}_n$ (v_{nx}, v_{ny}, v_{nz})by the total (bulk) velocity $\mathbf{v}$(v_x, v_y, v_z) as follows :

$$\mathbf{v_n} = \frac{\rho}{\rho_n}\mathbf{v} - \frac{\rho_s}{\rho_n}\mathbf{v_s} \tag{5.9}$$

In practice, the choice of the total (bulk) velocity, **v**, rather than the normal velocity, $\mathbf{v_n}$, permits to impose boundary conditions, which can be determined based on experimental input, e.g. simulation of forced flow conditions. Indeed, the choice of the normal and/or superfluid components of the velocity is subject to interpretation. Instead, the bulk velocity can be measured; hence its choice represents a more reliable variable to track.

Finally, according to the scaling analysis, we model the Helium II flow by the following PDE system :

$$\boxed{\left[\rho c^2\right]\nabla\cdot\mathbf{v} + \frac{\partial p}{\partial t} + \mathbf{v}\cdot\nabla p + \frac{\rho\rho_s\phi Ts}{\rho_n}\nabla\cdot\mathbf{v} - \frac{\rho\rho_s\phi Ts}{\rho_n}\nabla\cdot\mathbf{v_s} - \nabla\cdot\left(\phi k\nabla T\right) = \phi q} \tag{5.10}$$

$$\boxed{\frac{\rho_n}{\rho}\nabla p + \rho_s s\nabla T + \rho\frac{\partial\mathbf{v}}{\partial t} - \rho_s\frac{\partial\mathbf{v}_s}{\partial t} + A\rho_s\rho w^2\left(\mathbf{v} - \mathbf{v_s}\right) = \rho_n\mathbf{g}} \tag{5.11}$$

$$\boxed{\frac{1}{\rho}\nabla p - s\nabla T + \frac{\partial\mathbf{v}_s}{\partial t} - A\rho w^2\left(\mathbf{v} - \mathbf{v_s}\right) = \mathbf{g}} \tag{5.12}$$

$$\boxed{\rho C_v\frac{\partial T}{\partial t} + \rho\phi C_v T\nabla\cdot\mathbf{v} + \rho C_v\mathbf{v}\cdot\nabla T + T\frac{\rho\rho_s}{\rho_n}s\nabla\cdot\mathbf{v} - T\frac{\rho\rho_s}{\rho_n}s\nabla\cdot\mathbf{v_s} - \nabla\cdot\left(k\nabla T\right) = q} \tag{5.13}$$

Eight degrees of freedom (DOF) in a three-dimensional space are considered, namely the pressure, *p*, the velocity $\mathbf{v}(v_x,v_y,v_z)$, $\mathbf{v_s}(v_{sx},v_{sy},v_{sz})$ and the temperature, *T*. The vector of unknowns is expressed by $\mathbf{u}(p,\mathbf{v},\mathbf{v_s},T)$.

The substitution of this PDE into the general form of the PDE in time (discussed in Section 4.6), leads to the matrices :

$$\mathbf{u} = \begin{bmatrix} p \\ \mathbf{v} \\ \mathbf{v}_s \\ T \end{bmatrix} \qquad \overline{\overline{\mathbf{m}}} = \begin{bmatrix} 1 & 0 & 0 & 0 \\ 0 & \rho_n & \rho_s & 0 \\ 0 & 0 & 1 & 0 \\ 0 & 0 & 0 & \rho C_v \end{bmatrix} \qquad \overline{\overline{\mathbf{s}}} = \begin{bmatrix} 0 & 0 & 0 & 0 \\ 0 & A\rho_s \rho w^2 & -A\rho_s \rho w^2 & 0 \\ 0 & -A\rho w^2 & A\rho w^2 & 0 \\ 0 & 0 & 0 & 0 \end{bmatrix}$$

$$\overline{\overline{\mathbf{a}}} = \begin{bmatrix} \mathbf{v} & \rho c^2 + \varphi \frac{\rho_s \rho}{\rho_n} TS & -\varphi \frac{\rho_s \rho}{\rho_n} TS & 0 \\ \frac{\rho_n}{\rho} & \rho_n \mathbf{v}_n & 0 & \rho_s s \\ \frac{1}{\rho} & 0 & \mathbf{v}_s & -s \\ 0 & \rho \phi C_v T + \frac{\rho_s \rho}{\rho_n} ST & -\frac{\rho_s \rho}{\rho_n} ST & \rho \mathbf{v} C_v \end{bmatrix} \quad \overline{\overline{\mathbf{g}}} = \begin{bmatrix} 0 & 0 & 0 & 0 \\ 0 & 0 & 0 & 0 \\ 0 & 0 & 0 & 0 \\ 0 & 0 & 0 & 0 \end{bmatrix} \quad \mathbf{q} = \begin{bmatrix} \phi q \\ \rho_n g \\ g \\ q \end{bmatrix}$$

5.3 Numerical Analysis

5.3.1 Algorithm Stability

The numerical treatment of the partial differential equation is, by itself, a vast subject. PDEs are the engines of computer analysis or simulations of continuous physical systems and many different integration methods exist. A main advantage is that the (p, **v**, $\mathbf{v_s}$, T) variables are the drivers of conservation balances, and treating them implicitly in the solution algorithm largely improves the stability of the numerical integration.

We have identified the finite element (FE) method augmented with finite difference (FD) method with upwinding, to improve the stability of the solution, as a preferred approach for solving our two-fluid flow approximation.

Numerical analyses were performed using simple one-, two-, and three- dimensional models. The adaptability of the new code allows us to activate different numerical schemes of the Beam-Warming family. The time integration methods are implemented to take into account the variation of the helium properties with temperature and pressure. In particular, the Gorter-Mellink coefficient depends strongly on temperature, and tests were performed using it as a constant, linear or 12th order polynomial with temperature as a unique variable.

Artificial diffusion has been used to enhance the numerical stability. Upwind artificial diffusion was added to the pressure and temperature equations to balance the negative diffusion associated with the finite element discretization of the convection terms in these equations. Artificial viscosity is used for the momentum equations based on the Lapidus scheme, to balance the dispersion and improve the response to waves and discontinuities in the velocities.

5.3.2 Stabilizing the PDE System Using Artificial Diffusion

By comparison to the classical Navier-Stokes equations, the considered PDE system doesn’t use the viscous term. Indeed, according to the scaling analysis, this term is neglected since it is 3 order of magnitude smaller than the other terms of the governing equations. Hence the behavior of the PDE solutions is similar to solutions obtained from the Euler equation, which is well-known by numericists to be difficult to stabilize. With this in mind, we introduce different schemes of artificial diffusion techniques (overdamping). The use of predefined schemes is helpful to stabilize the solution without changing the solution too much.

The distinction between hyperbolic, elliptic and parabolic partial differential equations can be qualitatively described by the way the disturbances are propagating. A perturbation of the initial data of an elliptic or parabolic equation is felt simultaneously by every node in the domain. The PDE system developed in Chapter 3 contains several nonlinear terms and is highly hyperbolic. The use of hyperbolic partial differential equations typically generates numerical instabilities, due to the fact that a local disturbance is not felt by every node at once and an oscillation can propagate through the mesh. Large oscillations due to the local numerical instabilities can be handled by refining mesh size, tuning the time step or by adding artificial diffusion (artificial viscosity or numerical diffusion are also commonly used terms). Artificial diffusion is added to a scheme to stabilize it for dominating convection conditions, i.e. by adding a diffusive term proportional to the second space derivative of the solution to the transport equations :

$$-\alpha_{artificial}\frac{\partial^2 u}{\partial x^2} \tag{5.9}$$

where the different methods utilize different values of artificial diffusion coefficient as illustrated in Table 5.7. A detailed study of the artificial diffusion is shown in Appendix 8.4.

Table 5.7: Artificial Diffusion for different numerical schemes

Numerical scheme	Mass matrix	Artificial Diffusion
Finite Difference	lumped	0
Upwind Finite Difference	lumped	$\frac{v\Delta x}{2}$
Finite Elements	consistent	0
Lax-Friedrichs	lumped	$\frac{\Delta x^2}{2\Delta t}$
Lax-Wendroff	lumped	$\frac{v^2\Delta t}{2}$
Taylor-Galerkin	consistent	$\frac{v^2\Delta t}{2}$

Hence, the pressure and the energy equations make use of the first-order upwind upwind scheme, as defined above. The artificial viscosity is proportional to the fluid speed and the element size, resulting in optimal balancing of the hyperbolic transport term at high Peclet number. This choice is effective for velocity at fronts and large temperature gradients, but can lead to pressure oscillations during transients.

For the momentum equations, we prefer to use the second-order artificial viscosity as defined by Lapidus. The artificial viscosity is proportional to the velocity gradient and to the square of the element size through an empirical coefficient. This choice provides good smoothing for velocity and pressure at fronts, but is not effective for temperature fronts.

Table 5.8 lists the different schemes used and the characteristic parameters implemented in the matrix G (see Eq. 4.40).

Table 5.8: Summary of the different Artificial Diffusion schemes used

Pressure equation	Velocity equations (v and v_s)	Energy equation
(upwind)	(Lapidus)	(upwind)
p: $\frac{dx}{2}\lvert v+c\rvert$	$CL \cdot h^2 \cdot \left\lvert\frac{\mathrm{dv}}{\mathrm{dx}}\right\rvert$	p: $\varphi\rho C_v \frac{dx}{2}\lvert \mathrm{v}\rvert$ T: $\rho C_v \frac{dx}{2}\lvert \mathrm{v}\rvert$

5.3.3 Convergence Error

We have performed a convergence analysis in time and in space to verify the validity and the capability of the code. Simple linear geometries with different mesh sizes and different time steps were used to assess the errors.

Fig. 5.1 shows the error of convergence in time obtained using the Euler-Backward scheme as defined by the L_2 and the L^∞ norms (the two norms are described in the following chapter 5.3.4), e.g. to estimate the error of convergence in time, we use the maximum deviation:

$$L\infty\colon \|\mathrm{v_{nz}} - \mathrm{v^*_{nz}}\|_\infty = \sup_i \left|\mathrm{v_{nz}} - \mathrm{v^*_{nz}}_i\right|,$$

and the standard deviation :

$$L^2\colon \|\mathrm{v_{nz}} - \mathrm{v^*_{nz}}\|_2 = \left(\sum_i \left|\mathrm{v_{nz}} - \mathrm{v^*_{nz}}_i\right|^2\right)^{\frac{1}{2}}$$

where dt is the time step; vnz_Linf and vnz_L2, are the differences between the normal component velocity, v_{nz}, and the reference velocity, v^*_{nz}, obtained using the smallest time step. Results are comparable for both averaging techniques. As expected, the convergence rate is close to 1.

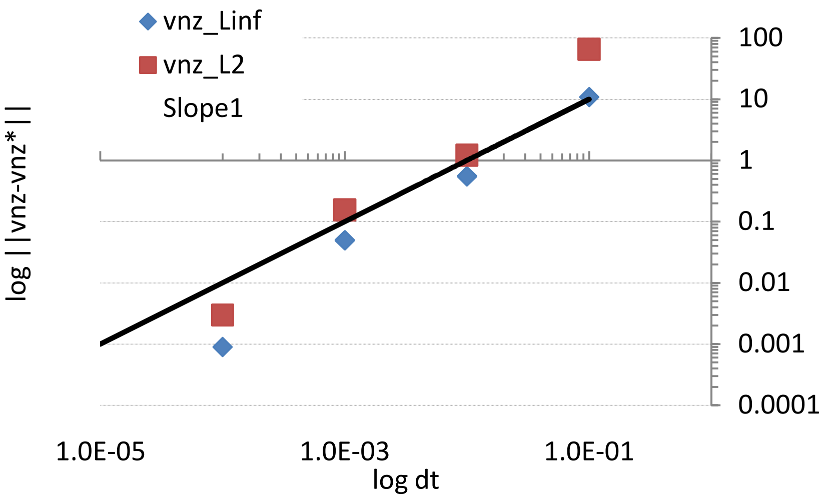

Figure 5.1: Error of convergence in time

We expect that a 1st order time integration method, such as the Euler-Backward Implicit scheme, converges monotonously toward the solution with a modest rate. On the other hand, the use of the 2nd order accurate Crank-Nicholson algorithm has a higher rate of convergence, hence reaching a desired error faster, but solutions can exhibit instabilities.

In a similar approach, we test the convergence using 1-D models composed of different node numbers for a given channel length. Fig. 5.2 shows the error of convergence in space obtained using the Euler-Backward scheme is close to 1.

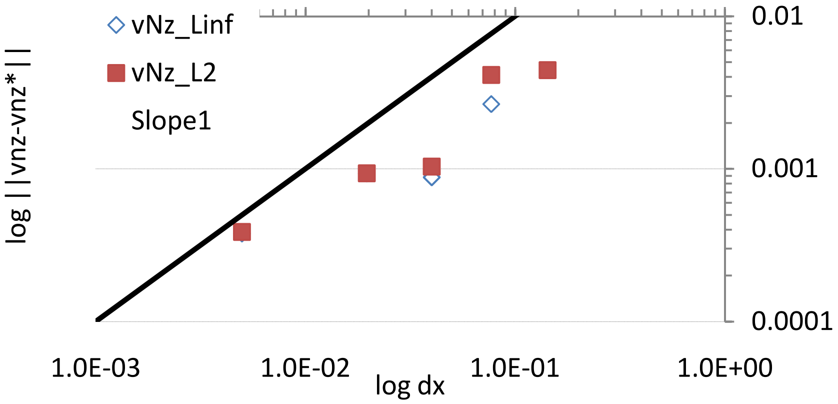

Figure 5.2: Error of convergence in space

5.3.4 Data Post-Processing and Data Dispersion

The results of the 3DHeliumSolver are stored in a text file, available for post-processing. This output file contains the coordinate of the node, the pressure, the temperature and velocities listed at every time step. The total, the normal and the superfluid velocities are available for each time step, providing the evolution of the resulting velocities fields. The data are processed by visualization of the resulting fields, using Excel® and Tecplot ®. For the objective of the numerical analysis, the dispersion on the results is defined in term of L^p metrics. We use the maximum deviation (L^∞), Eq. 5.14, and the standard deviation (L^2) Eq. 5.14 (with p=2), to estimate the normal component velocities. A similar functional analysis is applied to the different test cases considered below. The norms are defined as follows :

$$\|x\|_\infty = {}^{sup}_{\ n}|x_n| \tag{5.14}$$

$$\|x\|_p = \left(\textstyle\sum_n |x_n|^p\right)^{\frac{1}{p}} \tag{5.15}$$

5.4 Second Sound Propagation

Helium II exhibits particular properties like the fluctuation of entropy, which in turn results in the observation of a second sound. The use of second sound in a bath of Helium II is very important. For example, it provides an experimental way to detect the origin of a quench in superconducting RF cavities or magnets [71]. Whereas temperatures can easily be experimentally measured, the velocities can hardly be measured to any accuracy. Hence modeling second sound using pressure, temperature and heat flux as boundary conditions has useful applications.

The speed of the second sound (c_2) is determined by observing the temperature rises at given locations within the 1-D model. Fig. 5.3 shows a schematic view of one method of measuring this experimentally. A heat source is applied at one extremity to a channel filled with a bath of Helium II. A temperature sensor installed along the channel will measure the rise in temperature caused by the heater. Typical experimental set-ups make use of a square-shape pulse of heat flux in order to better monitor this phenomenon using thermometry techniques.

In a numerical approach, instead of using temperature sensors, we trace the evolution of the temperature and the velocities at any node of interest along the Finite-Element mesh. To illustrate this, we consider a bath of helium at 1.9 K, which can be modeled by a 1-D linear mesh and simulate applying a heat flux of 15 kW/m^2 to one extremity, while maintaining the other extremity at 1.9 K and 10^5 Pa. The channel is composed of 100 linear FEs for a total length of 1 m. Figures 5.2 and 3 illustrate the temperature and velocity profiles for example bath temperatures of 1.6 K, and 1.9 K, respectively. The amplitude of the temperature step decreases when moving away from the heated boundary, which corresponds to attenuation of the second sound wave, and is reflected in a decreasing amplitude of the normal and superfluid velocity steps. The normal and superfluid component velocities are shown for 4 nodes along the mesh for the first 0.5 sec. The selected nodes are located at the inlet, 20, 40 and 80 % of the total channel length. The time step used for this simulation is 10^{-5} sec. The speed of the second sound is estimated by determining the time of the variable rises for at least 4 nodes along the mesh. The results are averaged and reproduced for different mesh sizes and different time steps.

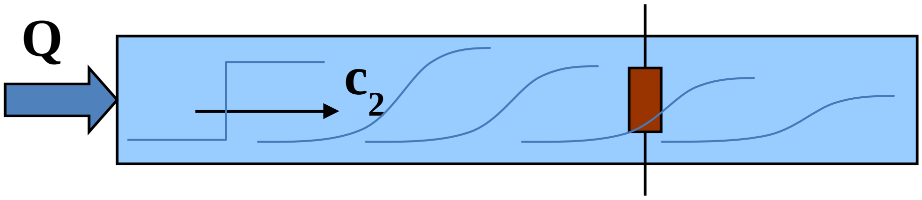

Figure 5.3: heat flux of 15 kW/m2 applied to one extremity, while maintaining the other extremity at 1.9 K and 105 Pa.

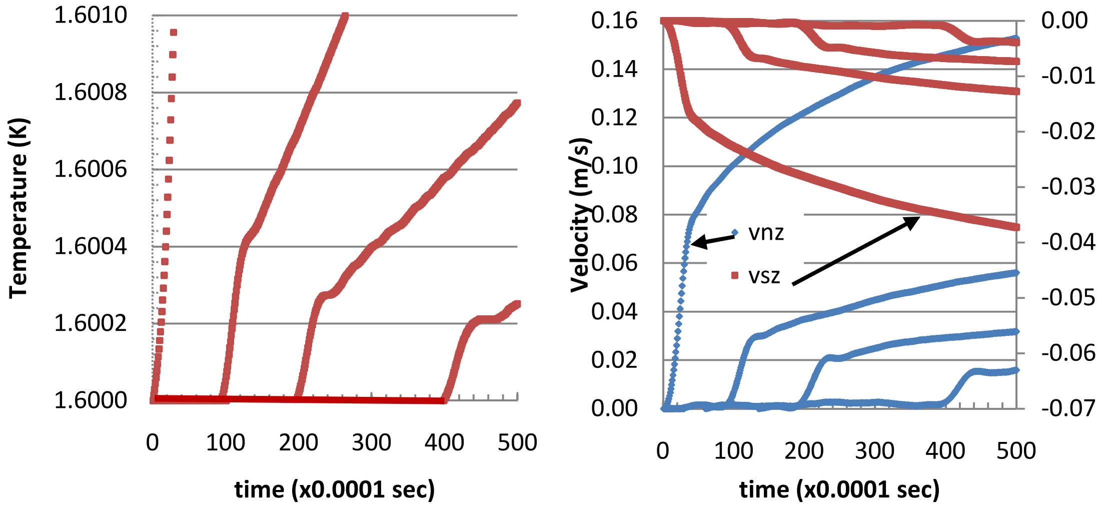

Figure 5.4a: Propagation of the temperature and velocities waves, for nodes located at the inlet, at 20 %, 40 % and 80 % of the total channel length. Bath temperature is 1.62 K. c2=21.97 m/s

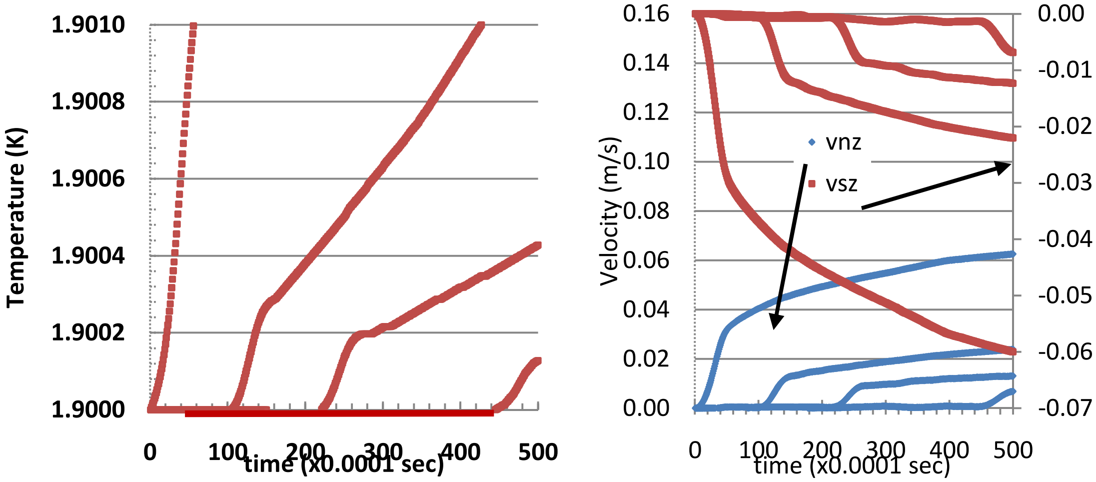

Figure 5.4b: Propagation of the temperature and velocities waves, for nodes located at the inlet, at 20 %, 40 % and 80 % of the total channel length. Bath temperature is 1.9 K. c_2=19.96 m/s

Numerical results can be compared to theoretical calculated values. The speed of the second sound in Helium II is defined as [2]: $c_2 = \left(\frac{\rho_s}{\rho_n}\frac{Ts^2}{C_v}\right)^{1/2}$.

Fig. 5.5 shows good correlation between results and expectation for second sound velocities. The error is smaller than 10 % for the range of bath temperatures 1.4 K–2.1 K.

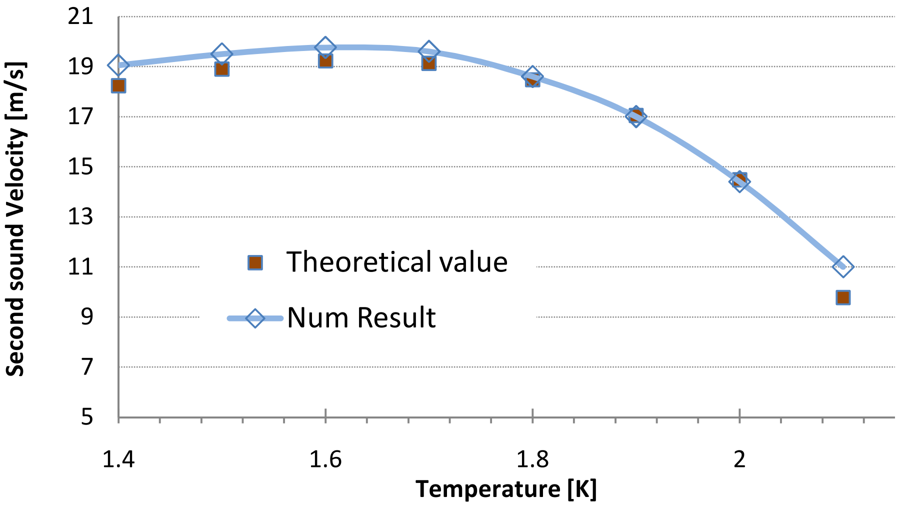

Figure 5.5: 2^{nd} sound: Comparison of numerical and theoretical prediction for different bath temperatures

Fig. 5.6 compares the normal component velocities of the first node for different bath temperatures (1.4 K to 2.15 K), while applying a constant heat flux to the inlet. The closer to T_λ the bath temperature is, the smaller the normal velocity component is.

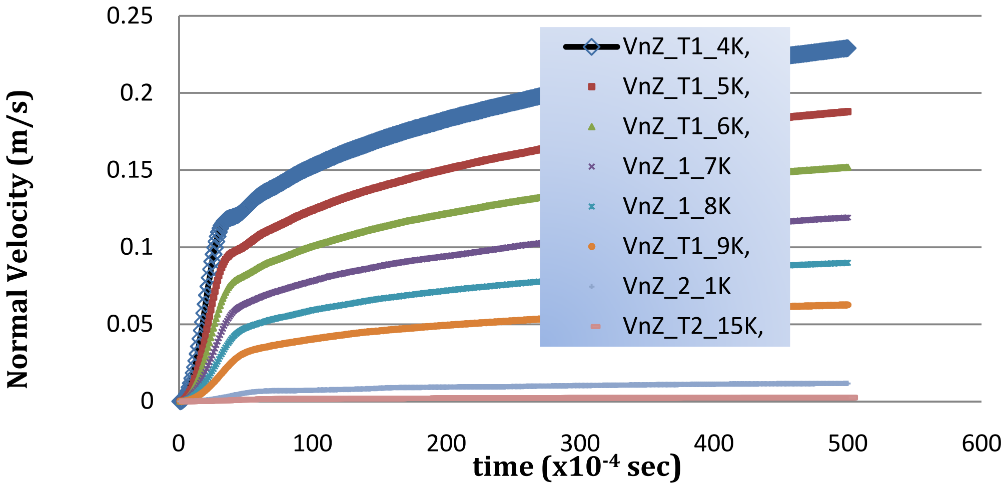

Figure 5.6: 2^{nd} sound: Comparison of normal velocities estimated

In the same way, we consider now a 2-D mesh, where we apply a heat flux to one face (x=0 m), while constant temperature and pressure are maintained on the other side. The mesh is defined with 1,728 quadrilateral finite elements (1,813 Nodes), providing the necessary space resolution to track the propagation of the wave. The time step used for the simulation is 10^{-6} sec. Results are stored every 10^{-6} sec. Fig. 5.7 a) shows the temperature wave propagating at 3 selected time steps (20 10^{-6}, 80 10^{-6} and 130 10^{-6} sec). The last two meshes Fig 5.7 b) show the normal and the superfluid component velocities after 0.13 msec. The main gradient is seen along the x-axis when a uniform heat flux is applied on the y-axis. The small existing gradient different appearing for y=0 m and y=0.05 m, is due to the boundary conditions set so that the bulk velocity along the y-axis is zero for both sides.

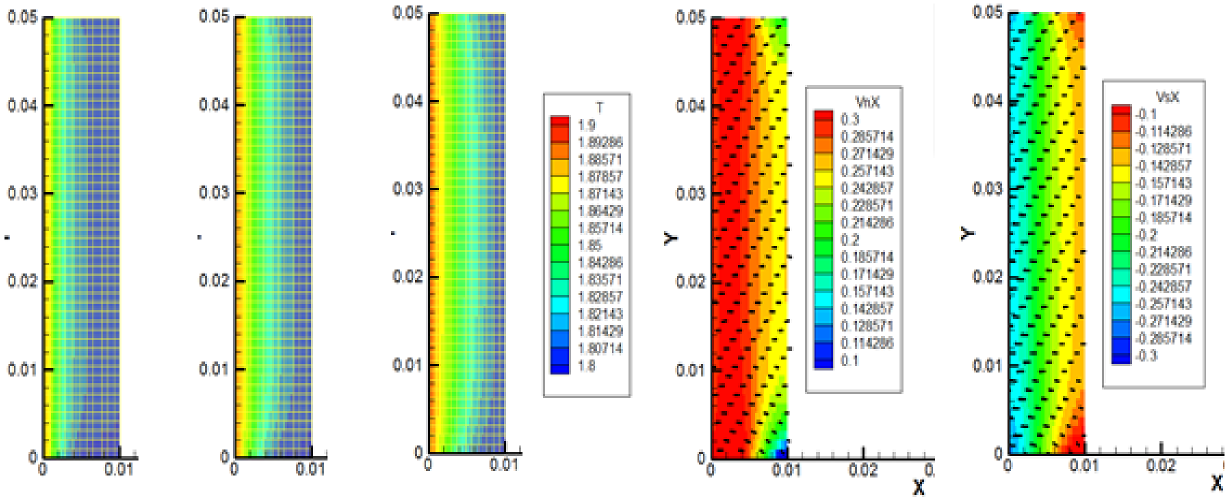

a) V_{nx} propagation for time steps (20 10^{-6}, 80 10^{-6} and 130 10^{-6} sec).

b) Resulting normal and superfluid component velocities after 0.13 msec.

Figure 5.7: Temperature evolution when the left side is heated. The initial bath temperature is 1.8 K

5.5 Thermal Counterflow in a 2-D and 3-D Channel

To illustrate a typical application, we consider thermal counterflow in a channel of Helium II. Three test cases are shown below:

1) 2-D channel modeling of a bath of Helium II. A temperature difference is applied between the inlet and the outlet of the channel. Boundary conditins are shown in table 5.9.

2) 3-D string of cubic Finite-Elements forms a long bar/channel. A temperature difference is applied between the inlet and the outlet of the channel. Such a mesh makes it possible to reduce the two dimensional problem to that of a 1-D problem, making possible comparisons to analytical solutions.

3) We reproduce experimental conditions at NHMFL, while using a 0.2 m long 1-D channel composed of 201 linear FEs. We compare the influence of the Helium II bath temperature at 1.62K, 1.68 K, 1.70 K, 1.77 K, 1.80 K, and 1.90 K.

First, a 2-D channel, 0.05 m long and 0.01 m wide, is modeled using 640 and 1,728 quadrilateral Finite Elements. The initial conditions and helium properties of the channel are set to simulate a bath of Helium II at 1.8 K, 0.1 MPa, We apply a constant temperature difference of 100 mK between the inlet, S3, and outlet, S4, of the 2-D channel. The largest acceptable time steps used to obtain stable numerical solutions at 640 FEs and 1,728 FEs, are 10^{-4} sec and 10^{-5} sec, respectively. This case is equivalent to imposing a heat flux of 27 kW/m^2 on a 1.8 K bath.

Table 5.9 lists the boundary conditions selected for the first test case. Fig. 5.8 a) shows the definition of the mesh and its sides.

Table 5.9: 2-D: thermal counterflow using a rectangular channel

	S1	S2	S3-inlet	S4-outlet
Initial conditions	p=0.1 MPa ; v_x=v_{sx}=v_y=v_{sy}=0 m/s; T=1.8 K			
Boundary conditions	v_x=v_{sx}=0	v_x=v_{sx}=0	T=1.9 K V_y=0	T=1.8 K v_y=0; p=0.1 MPa

Fig. 5.8 b) and c) show the resulting temperature gradient, and velocities. Arrows illustrate the trajectory of the normal (c) and superfluid velocities (b), endorsing the two-fluid thermal counterflow behavior (see Fig. 2.8). We recall that no bulk velocity is imposed. At steady-state, the temperature gradient is linear and the pressure is constant throughout the mesh, as expected for a 1-D symmetrical problem.

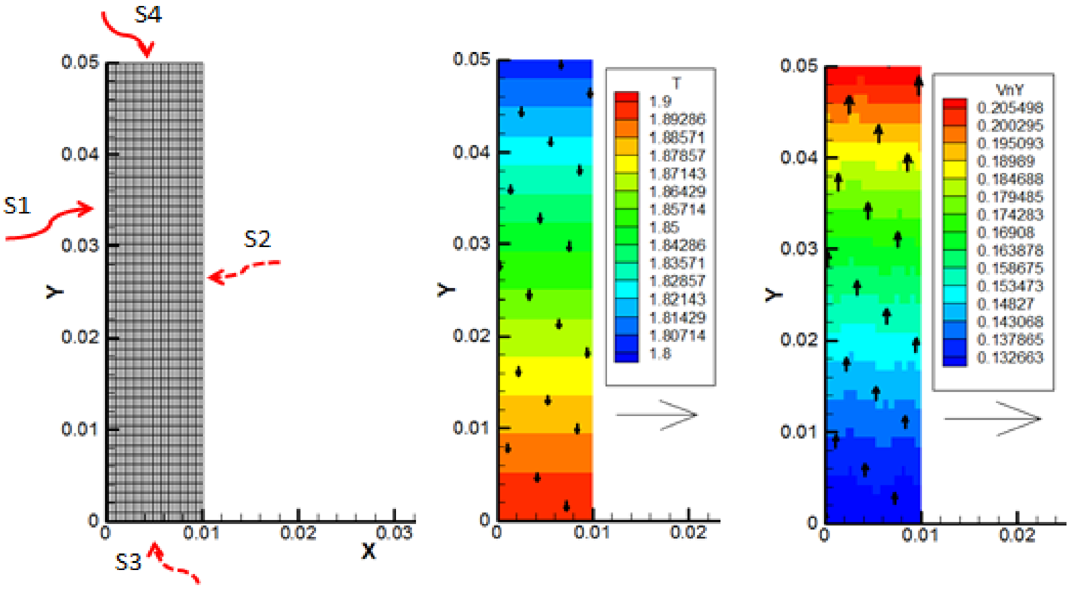

a) Geometry and boundary conditions **b) Temperature and v_{sy} (arrows)** **c) Normal component**

Figure 5.8: 2-D simulations of thermal counterflow in a Helium II channel after 1 sec

In the second illustration, a 3-D string of 100 cubic Finite-Elements is used to form a 1 meter long channel with a square cross-section. Each cubic FE has dimensions 0.01 x 0.01 x 0.01 m^3. We apply a temperature difference between the inlet and the outlet surfaces of the channel. Since the ratio of the channel length to its width is 100, we make the assumption that the results can be compared to analytical 1-D solution. According to chapter 2.2, in steady-state mode, the heat transported by Helium II can be approximated by :

$$\dot{q} = \frac{1}{L}\int_{Tout}^{Tin}\left(\frac{1}{f(T,p)}\frac{dT}{dx}\right)^{\frac{1}{3}} \qquad (5.6)$$

where T_{out} is the cold temperature applied to the outlet surface and T_{in} is the warm temperature applied to the inlet surface. The expected normal velocity is given by $v_n = \frac{\dot{q}}{\rho \cdot s \cdot T}$ and the resulting superfluid component velocity $v_s = \frac{-\rho_n \cdot v_n}{\rho_s}$.

In order to validate our results, we vary the temperature difference across the channel by imposing different inlet temperatures T_{in}, while the outlet temperature and pressure is fixed at T_{out} = 1.8 K and 10^5 Pa. Fig. 5.9 and Fig. 5.10 compare the expected values of v_n and v_S to the numerical results.

The error associated with the numerical approximation is less than 4 %. Larger discrepancies are observed in regions with strong non-linearity, i.e. close to T_λ where the approximation provided by Eq. 5.6 is most likely no longer fully consistent with the approximations of the fluid properties (see Fig. 4.1).

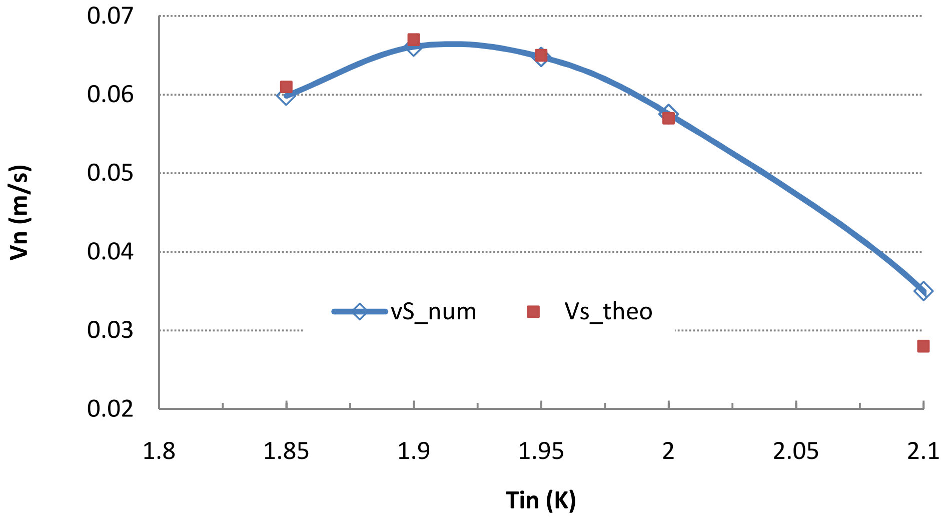

Figure 5.9: Normal component velocity at steady-state on the inlet

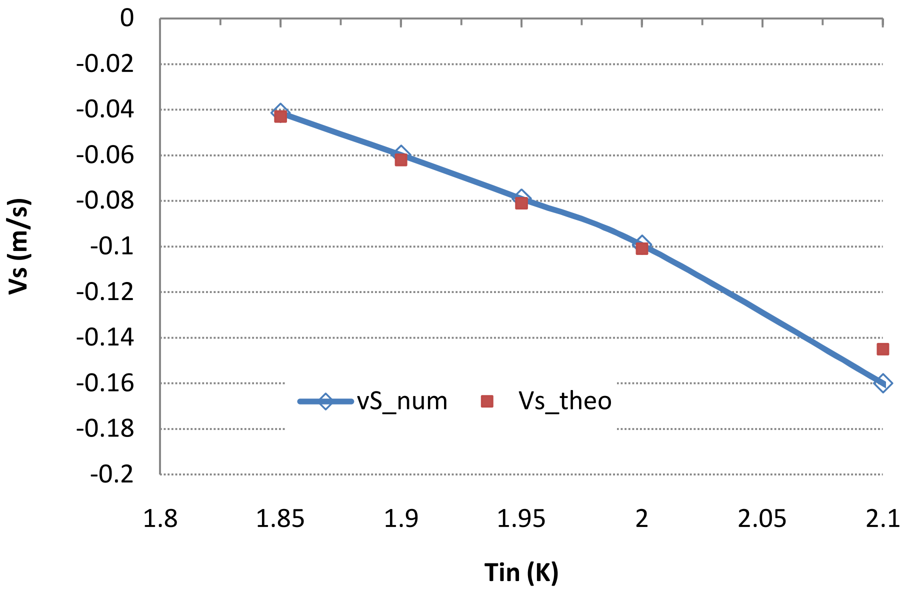

Figure 5.10: Superfluid component velocity at steady-state on the inlet

In the last illustration, we study a 1-D long model for which we maintain a constant outlet temperature and pressure while applying various different heat fluxes to the inlet. The choice of initial and boundary conditions aims to reproduce experimental data obtained using the PIV technique [72] [73] [1].

As shown on Fig. 5.11, a factor 2 between the measured velocity of the particle and the theoretical value of v_n was obtained in average. Hence the PIV technique doesn't allow a precise signature of the normal velocity component (the only one that carries entropy). Vp,a_1_8K, is the velocity measured by PIV techniques in NHMFL [1]. The numerical results show the velocity of the normal component of Helium II, obtained for the selected heat fluxes. The numerical values of v_n obtained at steady-state, are added and compared to NHMFL's published result [1]. The large discrepancies observed between the normal component and the particles' velocity during these PIV measurements were discussed elsewhere [76][77].

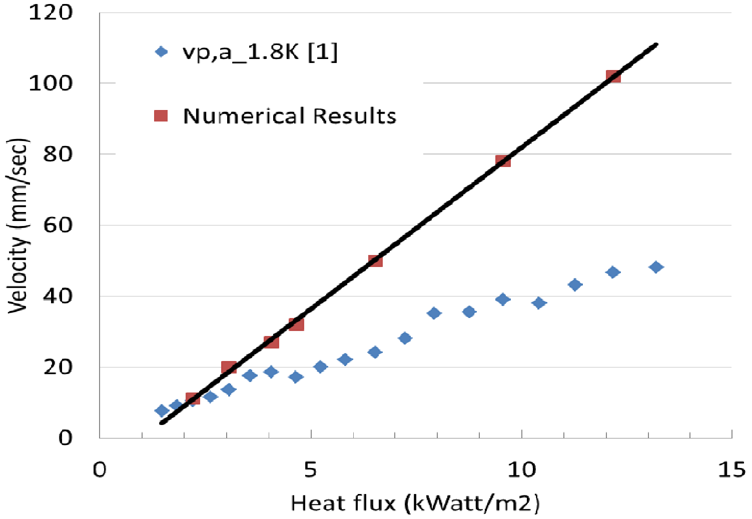

Figure 5.11: Comparison of the velocities resulting from thermal counterflow in a 3-D channel

Finally, all conditions experimentally tested in NHMFL were reproduced and compared to the analytical one expectation of v_n (Eq. 1.1). Numerical results fit theoretical values within 10 %.

5.6 2-D Simulation of Large Eddy Structure – Qualitative Approach

In this chapter we aim at demonstrating the existence of large eddy structure in a bath of Helium II, on which a localized heat flux is applied. This model represents an experimental setup [66][67]. This qualitative approach gives the particular behavior of the Helium II, as modeled through the PDE system. To illustrate these phenomena, we consider a 2-D mesh, composed of 640 quadrilateral FEs. We impose a heat flux on a portion of the inlet surface. Fig. 5.12 the initial and test cases studied. The initial and boundary conditions are displayed in Fig. 5.12 and in Table 5.10. A heat flux is applied to half of the bottom left side, (see Side 5, S5).

The time step is 10^{-4} sec leading to a Courant number, $^{c \cdot dt}/_{dx}$, equals to 0.4. The distributions of pressure, temperature and velocities can be traced over the time step for every node of the mesh. Similar conditions are applied on a second mesh composed of 1,728 FE. The results obtained are comparable. Fig. 5.12 and 5.13 illustrate the results for both meshes at the different conditions.

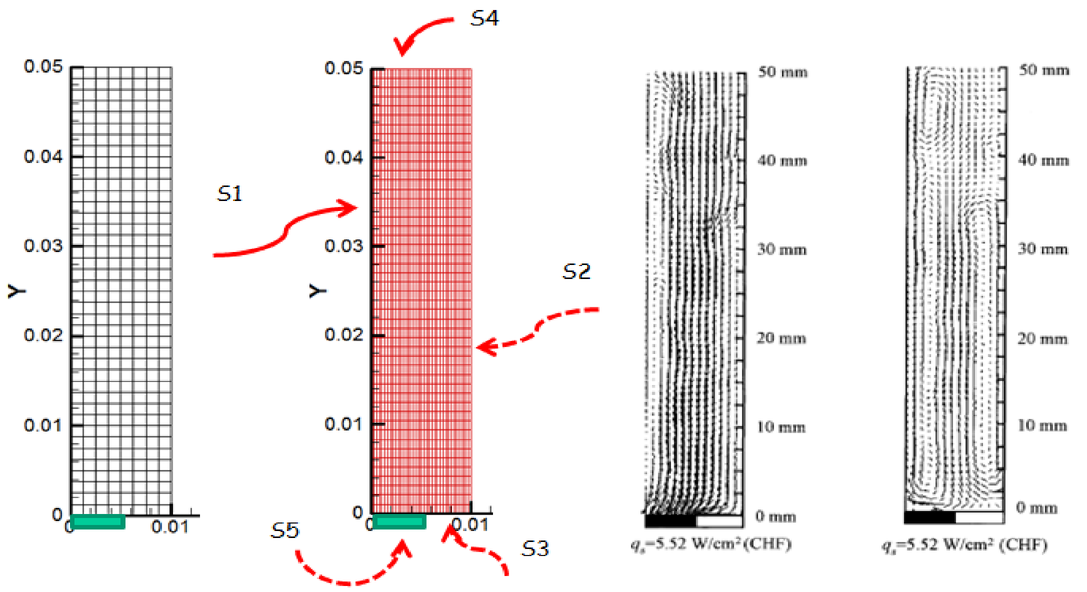

a) Mesh composed of 640 quadrilateral FE

b) Mesh composed of 1,728 quadrilateral FE

c) Bulk velocities (q=11.2 kW/m^2)

d) Superfluid velocities (q=11.2 kW/m^2)

Figure 5.12: Boundary conditions applied on the rectangular meshes and Kyoto's result [67]

Table 5.10: 2-D thermal counterflow using a heater: List of the conditions

	S1	S2	S3 – inlet (right)	S4 - outlet	S5 – heater(left)
Initial conditions	p =1e5 Pa ; v=0; v_s=0; T=1.8 K				
Boundary conditions	v_x=0; v_{sx}=0	$v_x = v_y$ =0; v_{sx}=0	v_y=0 v_{sy}=0	v_y=0 T=1.8 K	p=1e5 T=1.9 K

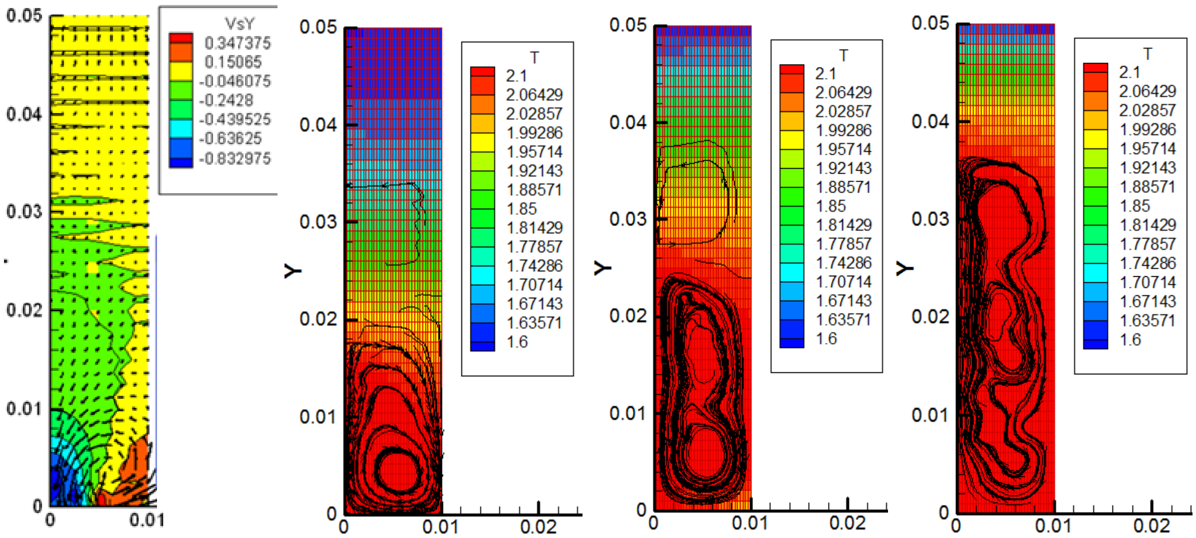

a) Superfluid component Velocity, v_s (640 FE)

b) Streamline for v_n and temperature (1,728 FE) (after 1.5, 3 and 60 msec, respectively)

Figure 5.13: Superfluid component velocity field and temperature gradient - heat applied to the bottom left side

In the transient mode, we observe the propagation of the temperature front along the vertical axis, y-axis. For a selected time step of 10^{-4} sec, the temperature distribution becomes stable after 100 msec and permanent eddy structures are observed. This is a signature pattern of the peculiar properties of Helium II. The rising normal component of fluid typically loses heat because it encounters a colder space; it also exchanges entropy and energy with the superfluid component traveling in the opposite direction, i.e. toward the warm source. The large structure moves. It was also observed elsewhere that the bulk velocity resulting from this type of condition The heat is only applied to half of the inlet section, provoking an asymmetrical condition on inlet side of the model. The mechanism can be interpreted using the significance of the terms in the governing equation. Indeed, although the convective term and the inertia term are neglected in the balance (i.e. the viscosity has been dropped from the governing equations), we observe the existence of “convective cells”. Hence, at steady-state only the mutual friction, coupled with the non-linear Helium II properties can cause entropy exchanges and the flow pattern. Energy dissipation based on the mutual friction between the two components generates variation in Helium II properties.

Similar numerical convection-like observations were obtained by the Kyoto team using an explicit finite difference method [67]. It is worth noting that they do not neglect viscosity or the convective term in the governing equations.

5.7 Qualitative Comparisons to NHMFL Experimental Results

5.7.1 Thermal Counterflow around a cylinder

Another exciting test case relates to the distinctive experimental work developed at NHMFL [5][74]. They show the thermal counterflow effect resulting from the implementation of a 3 mm and a 1 mm radius cylinder in a Helium II channel. Using the PIV technique, they were able to illustrate a surprising effect making allowance for thermal counterflow. We recall that the PIV technique is believed to follow the flow of the normal fluid, which carries the entropy. In this result a heat flux of the order 11 kW/m^2 was applied to the bottom of a 200 mm long channel, with a rectangular cross-section. The average polymer particle size is 1.7 μm (specific gravity = 1.1). The particle trajectory is visualized through the 0.018 x 0.018 m^2 square windows. Detailed descriptions of the conditions of the measurement are available elsewhere [5]. Fig. 5.14 a) shows the resulting streamlines reflecting the self-organizing non-linear recirculation. The explanation for these observations is by no means trivial. The two component velocities may generate a classical-like-vortex while traveling in the opposite direction to the cylinder [75].

Assuming that we can reproduce similar boundary conditions, it is of great interest to compare our numerical results with NMHFL's experimental observations. We simulated asymmetry conditions representative of the experimental set-up using a 3-mm radius cylinder. The conditions and geometry are shown in Table 5.11 and Fig. 5.15. Boundary conditions are applied to five sides, e.g. side 1, S1, is composed of nodes located along the y-axis when x equals 0. The selected time step for the simulation is 10^{-5} sec. Fig. 5.14 b) shows the numerical comparison to NHMFL results.

One fundamental result pertains to the observation flow features similar to the computed particle velocities [5]. At steady state condition, the numerical streamlines exhibit the formation of two large eddy structures above and below the 3-mm cylinder. Like for experimental results, the top circulating flow rotates counter-clock-wise, whereas the lower structure circulation is clock-wise. The pressure gradient is negligible, the temperature gradient is observed along the vertical direction of the channel (y-axis).

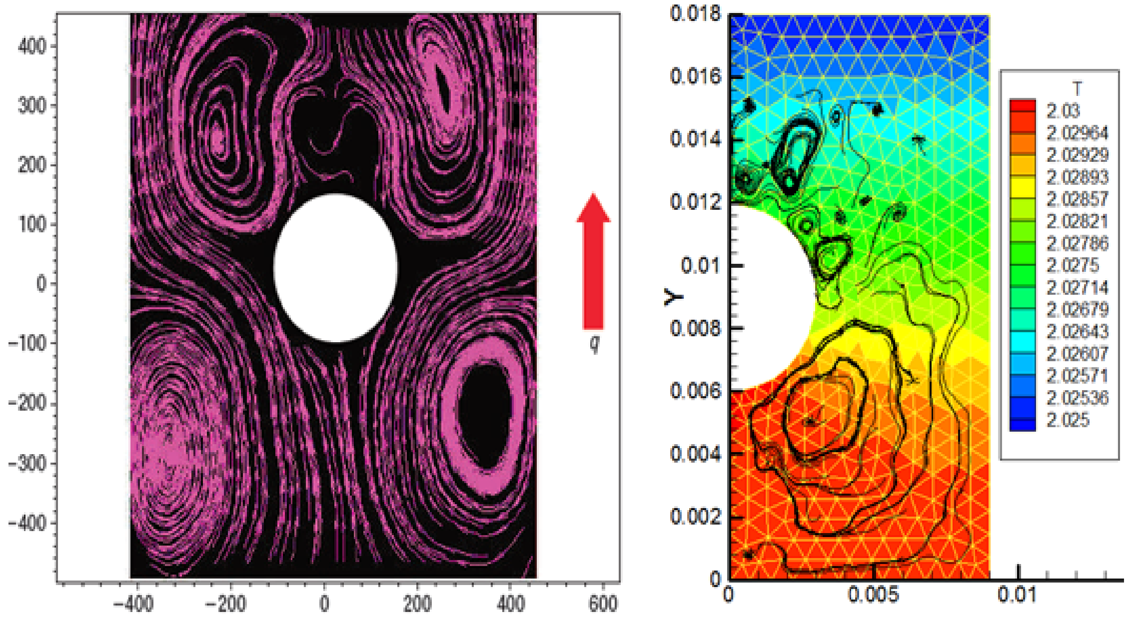

a) NHMFL experimental results [5]. Computed streamlines for particle motion.
b) Numerical results (644 FE). Temperature profile and streamlines.

Figure 5.14: Results for a heat flux, q=11.2 kW/m^2 applied on S3 and a bath temperature, T=2.025 K

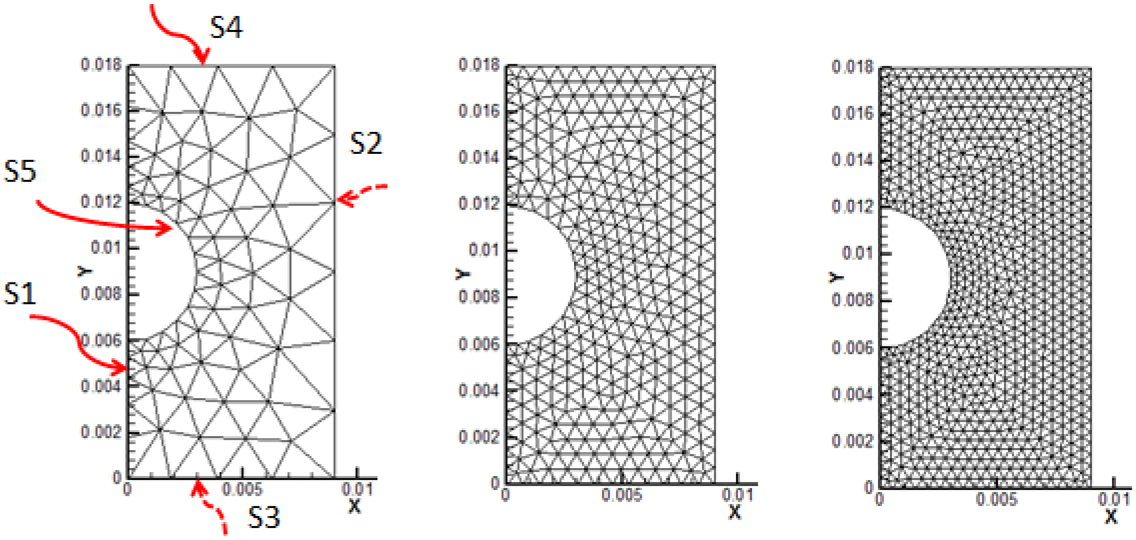

a) Coarse mesh (81 Nodes, 124 FE);

b) Medium mesh (363 Nodes, 644 FE);

c) Refined mesh (798 Nodes, 1471 FE);

Figure 5.15: 2-D Triangle FE meshes used to simulate NHMFL experimental set-up

Table 5.11: 2-D: thermal counterflow using cylinders: List of the conditions

	S1	S2	S3 - inlet	S4 - outlet	S5
Initial conditions	*p* =1e5 Pa ; v=0; v_s=0; *T*=2.025 K				
Boundary conditions	v_x=0; v_{sx}=0	v_x =0; v_y =0; v_{sx}=0	v_y=0 T=2.03 K (q=11.2 kW/m^2)	*T*=2. 025 K *p*=0.1 MPa	**v.n**=0 v_s.n=0

Using the same principle, several numerical models were tested to study the influence of the boundary conditions and the presence of the large eddy structures. For instance, the eddy structures are obviously shaped when large heat fluxes are applied. For those large heat fluxes, it is worth noticing that the upper large eddy structure is disappearing. The following two cases illustrate this observation.

Fig. 5.16 shows the temperature distribution and the normal velocity streamlines obtained if 25 kW/m^2 is applied on the side S3. For three different mesh sizes, we observe large eddy structures.

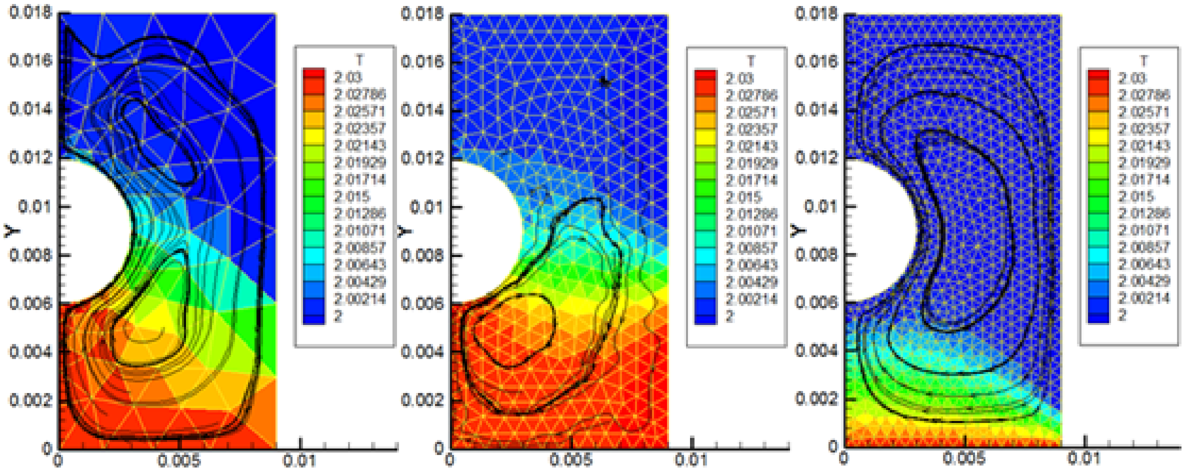

a) Coarse mesh (124 FE); b) Medium mesh (644 FE); c) Refined mesh (1471 FE);

Figure 5.16: Temperature distributions for the boundary condition: 2.00 K-2.03 K. The streamlines represent the normal velocity component (applied heat flux is 25 kW/m^2)

The top structure (rotating counterclock-wise) observed in the previous case (q=11 kW/m^2) is vanishing whereas the bottom structure grows and remains stable at steady-state. As a possible interpretation, we could speculate that the enhancement of the lower structure relates to the growing contribution of the superfluid component w.r.t the Gorter-Mellink turbulence.

The next example underlines the numerical results obtained if we inversed the temperature gradients between S3 and S4. Figure 5.17 shows the streamlines resulting of a 40 mK temperature difference applied across a mesh composed of quadrilateral finite elements. Intuitively, we expect to observe a symmetrical circulating flow pattern. The transient results show a different behavior. Actually, the results can be biased by the numerical technique, which is initialized by calculating solution for the nodes located on the x-axis (y=0). However, like for the previous example, we perceive two counter-rotating structures during the early development of the structures.

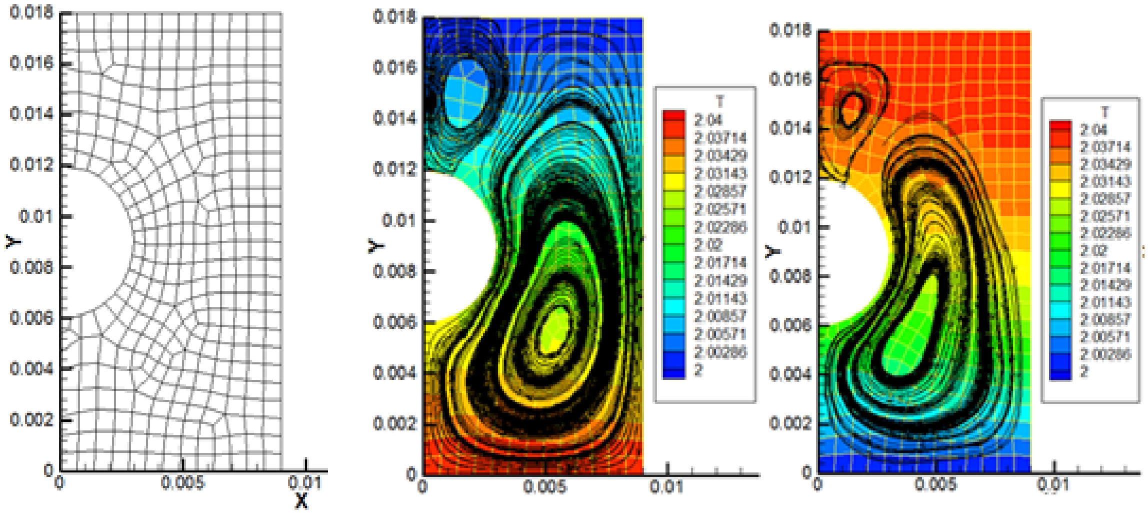

a) Quadrilateral mesh (315 FE); **b) Heat applied on S3;** **c) Heat applied on S4;**

Figure 5.17: Temperature distribution and streamlines (v$_n$) for inverted boundary conditions (2.00 K-2.04 K)

Let's now consider different temperature conditions and applied heat flux. Fig. 5.18 shows the existence of the upper and lower eddy structures, when 11 kW/m2 is applied across two different Helium II bath temperatures. Although the patterns are confirmed, the flow features are not very stable.

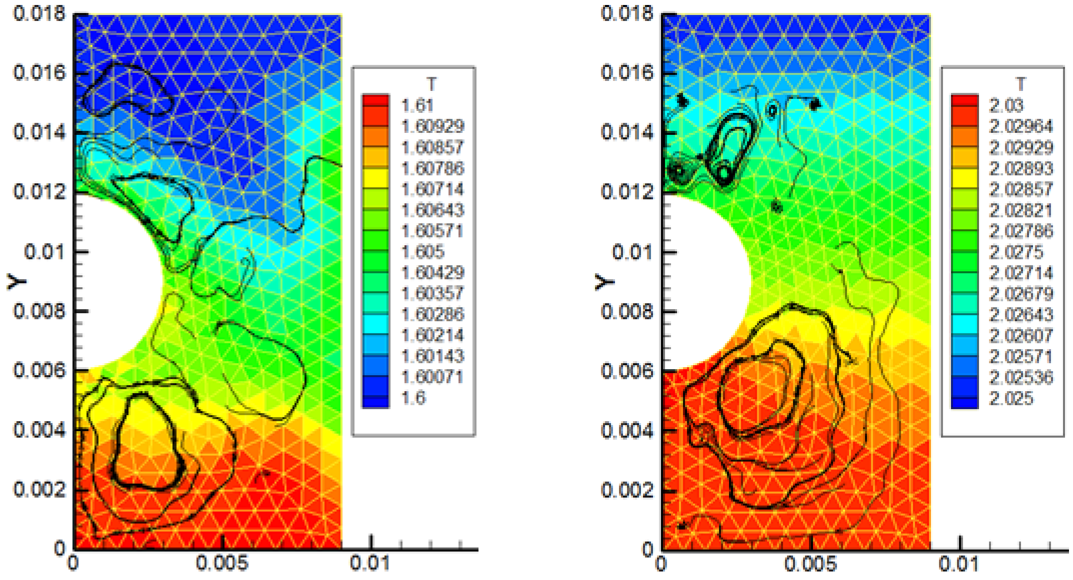

a) Bath temperature is 1.6 K (644 FE); **b) Bath temperature is 2.025 K (644 FE);**

Figure 5.18: Temperature gradients and streamlines for different temperature levels. q=11 kW/m^2

Finally, Fig. 5.19 presents a similar comparison for a larger heat flux, q=25 kW/m^2.

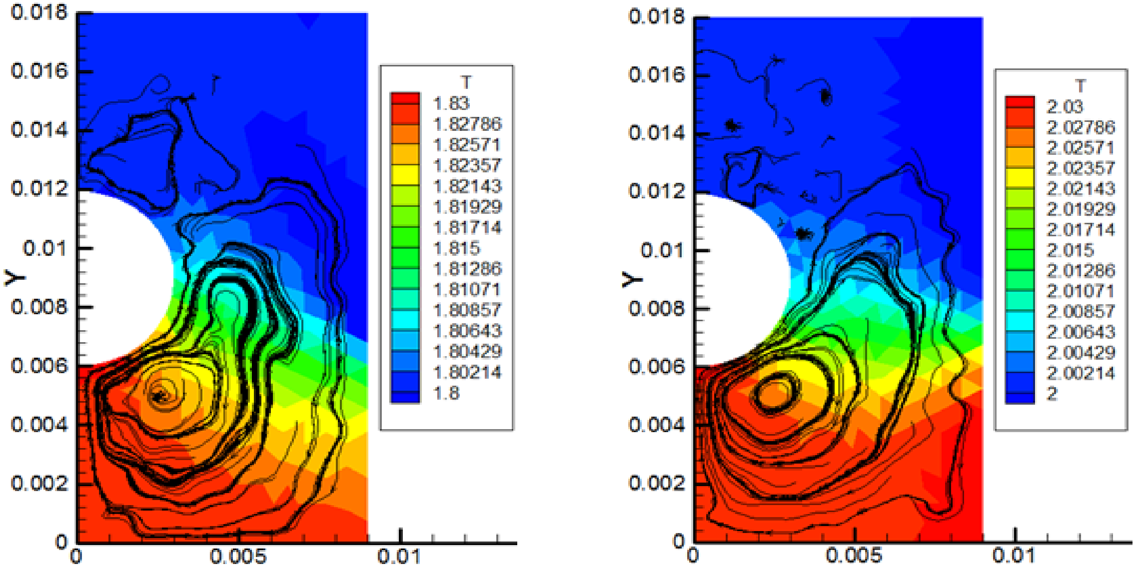

a) Bath temperature is 1.8 K; **b) Bath temperature is 2.0 K;**

Figure 5.19: Temperature gradients and streamlines for different temperature levels. q=25 kW/m^2

To conclude this section, we need to underline that for the given 2-D simulations, the numerical solutions show that the net mass flow exists in the Helium II bath. As expected, in most of the cases studies, the motion of the normal and superfluid components are related. This observation was also noted by other researchers [67] [66]. We also note that the large eddy structures are moving periodically and their position depend on the choice of the boundary conditions.

The mechanisms are similar to the one suggested in the previous chapter. The removal of the influence of the gravity from the PDE doesn’t affect the resulting velocity pattern. No classical turbulence can be referenced, since the inertia and viscous terms are dropped in the governing equations. Although no convective term is included in the governing equation, we nonetheless observe a convective cell-type structure. A laminar flow would appear if we were to consider a pure Euler flow. No diffusion is used.

Artificial diffusion is used to prevent oscillation of the quantities, but doesn't have any impact on the generation of the large eddy structure. According to the scaling analysis, this term is 3 orders of magnitude smaller than the mutual friction effect.

No precise quantitative analysis can be extracted from this model. Only a qualitative behavior of the flow is of interest. Three important considerations must be taken into account when comparing numerical to experimental data.

1- We assume that the streamlines obtained by the PIV technique display a combination of the two-fluid velocities. The particle follows the motion of the normal velocity. In reality we know that a slip velocity and/or the interaction between the particle, the normal and the superfluid component must be taken into account. From Section 5.5, measurements performed in a classical counterflow channel revealed a factor two difference between the expected ($\mathbf{v_n}$) and measured ($\mathbf{U_p}$) velocity of the particle. Several research groups have been investigating these dynamics [76][77].

2- Another limitation is that the mesh used is relatively coarse, due to the required computing capacity used to simulate relevant test cases using a basic PC. The current results make use of a basic computing capacity, e.g. dual core, Intel® processor, 2.2 GHz, 4 GB of installed memory (RAM). Note that the examples chose do not exhaust the code capabilities.

3- Finally the boundary conditions are only a best-guess of the exact experimental conditions, e.g. the mesh is limited to the observation windows in the PIV experiment. No temperature measurement was used to confirm the condition applied.

5.7.2 Applications using a Sphere in a 3-D mode – Drag Coefficient

The primary objective of this section is to introduce another potential application of using a 3-D fluid code able to solve the two-fluid equations. In practice, NHMFL conducted experimental test using a sphere immerged in a bath of Helium II [78]. They studied the drag coefficient for non-zero flow velocity.

We aim at completing this analysis in chapter 5.7.3. As a potential study related to the study of the drag coefficient in Helium II, we consider a 3-D rectangular mesh including a sphere at its center. A 0.018 x 0.009 x 0.009 m^3 mesh was created using 840 tetrahedral Fes, as shown in Fig. 5.20.

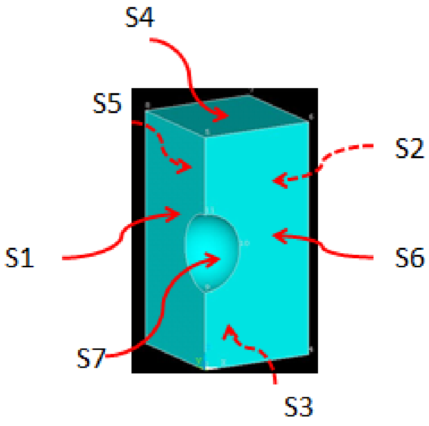

Figure 5.20: 3-D mesh representing a sphere in a rectangular channel.

Table 5.12: 3-D thermal counterflow using a sphere: List of the conditions

	S1	S2	S3 - inlet	S4 - outlet	S5	S6	S7
Initial conditions	p=0.1 MPa; $v=v_S=v_{sy}=v_y=(0,0,0)$; T=2.00						
Boundary conditions	$v_x=v_{sx}=0$	$v_x=v_{sx}=0$	T=2.03 K $v_z=v_{sz}=0$	T=2.00 K $v_z=v_{sz}=0$ p=0.1 MPa	$v_y=v_{sy}=0$	$v_y=v_{sy}=0$	v.n=0

A temperature gradient was applied between the top and bottom faces of the mesh. Fig. 5.21 shows the temperature distribution on a normal velocity distribution, resulting from thermal counterflow around the sphere. The normal and the superfluid velocity components are flowing in opposite direction. More refined meshes are needed to observe large eddy structures and we are unfortunately limited by current computing capacity.

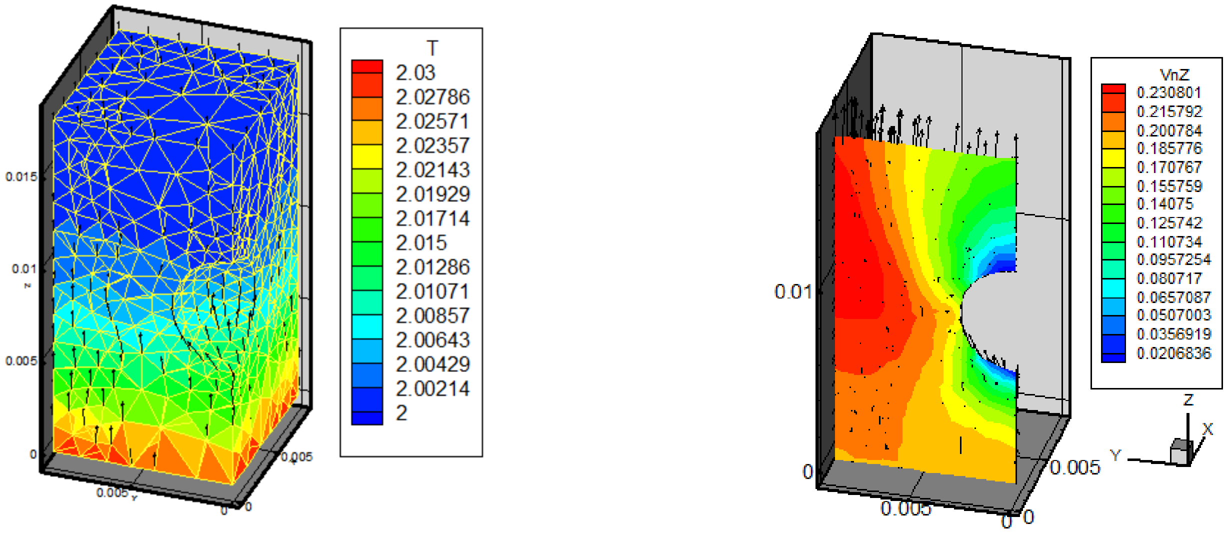

a) Temperature distribution for a 30 mK gradient (arrows represent v_n)

b) Normal component velocity distribution, v_{nz}, (one slice is displayed, picturing a 2-D map)

Figure 5.21: 3-D mesh (840 FE) of a 3 mm radius sphere in a Helium II bath, T bath=2.03 K, 0.01 MPa. The thermal counterflow is due to an applied temperature gradient (2.00 K – 2.03 K)

If we use a larger capacity computing system, the velocity fields of the two components can be more accurately simulated. Then, it would become possible to estimate the force due to the normal fluid drag, applied on the sphere. Hence we could propose a more accurate explanation of the drag in helium II on large obstacle.

5.7.3 Qualitative Expression of the Drag Coefficient

In the present Section, we study the expression of the drag coefficient on the small PIV particle itself. It is a complement to the previous Section. As the PIV technique maps out the velocity field of particles suspended in the fluid, it is not a trivial problem to relate the observed particle motion to the individual velocity fields of the normal and the superfluid components in Helium II [5]. Taking into consideration the numerical study of the phenomenological behavior of Helium II, we attempt to understand PIV measurements obtained by NHMFL.

On the one hand, the study of the particle dynamics in a classical fluid flow is detailed in Appendix 8.3. That subsection, therein is dedicated to study the influence of the drag coefficient in a normal Newtonian fluid. This earlier study allowed us to better identify the behavior of particles in PIV technique. This subsection has been dedicated to a mathematical formulation and numerical application to PIV results obtained in other laboratories, e.g. it has been supporting potential explanation to the experimental observations [1].

On the other hand, the use of the two-fluid model doesn't account for the microscopic behavior of the dynamics of Helium II, these qualitative results could reproduce large eddy structures as observed in nature. We propose a bridge between the experimental results and the numerical one, by using the Drag coefficient as a tool to communicate between the two.

Let's return to the fundamental experimental measurement involving the thermal counterflow. Fig. 5.23 to 5.24 are used to predict the difference in velocity between the particle and the fluid$\left(\mathrm{v_n}\text{-}\ \mathrm{U_p}\right)$. The particle may witness a slip velocity if the buoyancy is not ideal. In addition, the influence of "Gorter-Mellink turbulence" is important due to the fact that the small particles can be trapped in vortices and be driven away from the normal fluid trajectory. The force interacting between the particle, normal fluid and superfluid system can only be fully understood if we account for microscopic scale effects. Phenomenological explanations are being attempted elsewhere and encourage experimental measurement. Nevertheless, we can foresee that the general particle Drag can be approximated in the flow by simple equations. Typically, the Reynolds number reduces to the normal component velocity and its viscosity is used to characterize the degree of "excitation" of the fluid. Still, this dimensionless quantity refers to an inertia term, which is far from being the signature characteristic of superfluid behavior. Instead the degree of "excitation" of Helium II, as shown in PIV measurement can be described in a more empirical way.

To understand these surprising experimental results, a theory has been developed [77]. In this theory the relaxation time is expressed as follows :

$$\frac{d\mathrm{U_p}}{dt} = \frac{1}{\tau}\left(\mathrm{v_n} - \mathrm{U_p}\right) - \frac{1}{\rho}\nabla p + \frac{\mu_n}{\rho}\nabla^2 \mathrm{v_n} \tag{5.16}$$

where $\mathrm{U_p}$ is the velocity of the particle, τ the "viscous relaxation time" and μ_n the viscosity of Helium II. We complete the scaling analysis, using Eq. 5.16 and the quantity listed in Table 5.1.

$$\frac{\partial \mathrm{U}_\mathrm{p}^*}{\partial t^*} = \frac{t_o}{\tau_o}\left[\mathrm{v}_\mathrm{n}^* - \mathrm{U}_\mathrm{p}^*\right] - \frac{p_o}{\rho_o \mathrm{v}_\mathrm{o}^2}\left[\frac{\partial p^*}{\partial r^*}\right] + \frac{\tau_o}{\mathrm{v_o} r_o \rho_o}\cdot\frac{\tau^*}{\rho^*}\frac{\partial^2 \mathrm{v}_n^*}{\partial r^{*2}} \tag{5.17}$$

Table 5.13: Scaling of relaxation time - List of the dimensionless variables

Dimensionless quantity	$\frac{t_o}{\tau_o}$	$\frac{p_o}{\rho_o \mathrm{v}_\mathrm{o}^2}$	$\frac{\tau_o}{\mathrm{v_o} r_o \rho_o}$
Value	10^5	10^5	10^{-5}

The typical relaxation time is of the order $\tau_o = 10^{-5}$ s. For the sack of this analysis, if we consider steady-state regime, we can then drop the terms $\frac{\mu_n}{\rho}\nabla^2\mathrm{v_n}$ and $\frac{d\mathrm{U_p}}{dt}$.

Following this, we can express the general drag coefficient as :

$$Drag = \frac{1}{\tau} = \frac{\nabla p}{\rho(v_n - U_p)} \tag{5.18}$$

From the heat transport properties of Helium II, we consider the non-turbulent regime, where the pressure difference is applied proportional to the temperature difference. We make here the approximation of an ideal flow and use the London's equation :

$$\Delta p = \rho \cdot s \cdot \Delta T \tag{5.19}$$

We recall that the temperature gradient can also be expressed as a function of the heat flux and the Gorter-Mellink coefficient as follows :

$$\nabla T = \frac{\beta\,\eta_n}{d^2(\rho\, s)^2 T} q - \frac{A_{GM}\ \rho_n}{\rho_s^3\, s^4\, T^3} q^3 \tag{5.20a}$$

$$\nabla T = \frac{\beta \eta_n}{d^2 \rho s}\left|v_n\right| + \frac{A_{GM}\ \rho_n}{s}\left|v_s - v_n\right|^3 \qquad (5.20b)$$

where *d* is the characteristic length (e.g. pipe diameter or distance between plate), η_n is the normal fluid viscosity and β takes on values of 2 for parallel plates and 32 for tubes [3].

These equations are for a 1-D pipe flow. The general expression is divided in two terms :

- A linear term representative of the laminar regime , which includes the viscous effect
- The power-3 “turbulent” regime term, which is the signature of Gorter-Mellink mutual friction.

Using the same guiding principle, we want to express the Drag coefficient as a contribution of a linear term and a dominating power-3 term.

$$Drag = \frac{\beta n_n}{d^2 \rho^2 (v_n - U_p)}\left(\frac{q}{ST}\right) + \frac{A\rho_n}{\rho_S^3 (v_n - U_p)}\left(\frac{q}{ST}\right)^3 \qquad (5.21)$$

In practice, the heat fluxes considered in the experimental results are larger than the critical heat flux at the given bath temperatures. Indeed, the published “pseudo” Reynolds numbers are in excess of 10^4. For this reason the linear term in the above equations become negligible.

To (very) first order, the Drag can be interpreted by comparing the numerical and experimental data.

From experimental results, we know $(v_n - U_p)$ for large heat flux [1]. In those cases, the turbulent regime is established and the linear contribution of the Drag can be neglected. Therefore, we attempt to express the particle friction using experimental data :

$$Drag = \frac{1}{\tau} = \frac{A\rho_n}{\rho_S^3 (v_n - U_p)}\left(\frac{q}{ST}\right)^3 \qquad (5.22)$$

We can now plot the relaxation time, τ, as shown in Fig. 5.22.

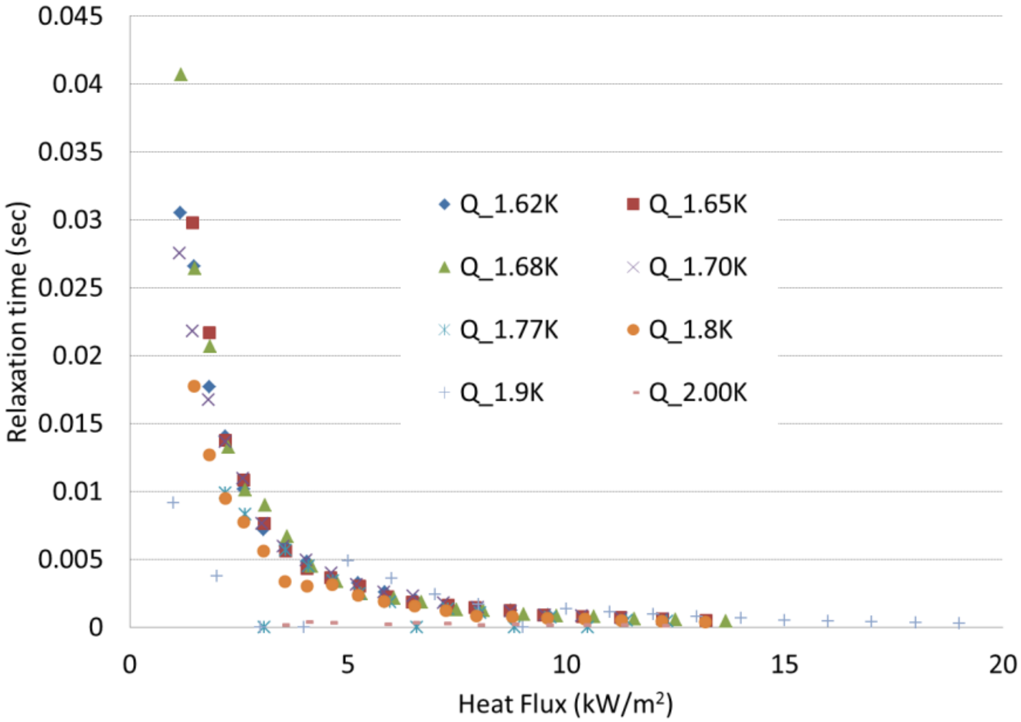

Figure 5.22: Relaxation time obtained from experimental measurement [1]

Providing that Eq. 5.22 expresses the Drag coefficient and is well described by the quantity $(Q/ST)^3$, we obtain Fig 5.22 using the same experimental results.

Fig. 5.23 shows that the proposed Drag coefficient is strongly depended on the helium II bath temperature.

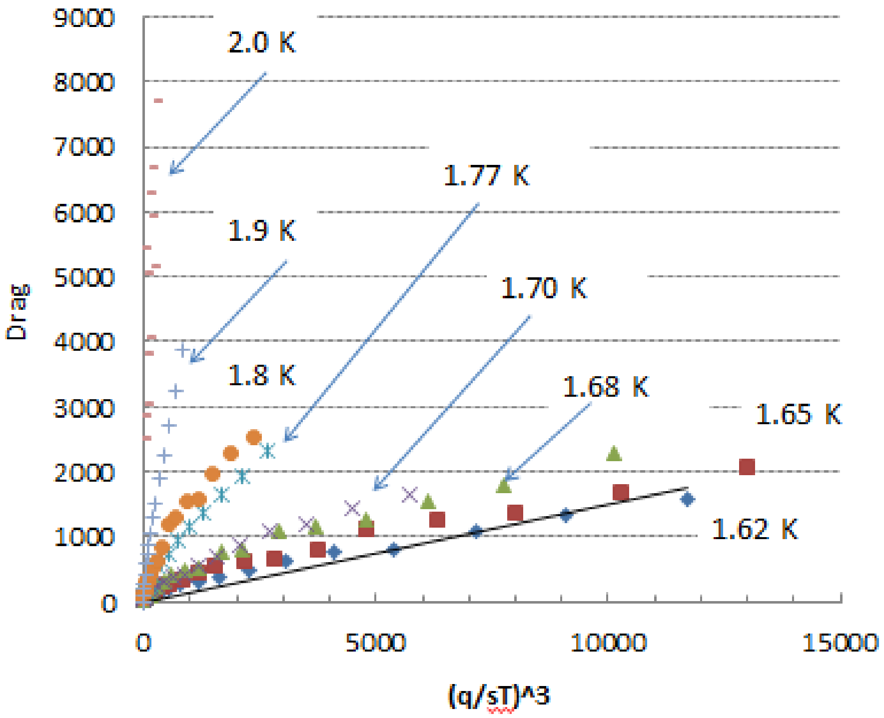

Figure 5.23: Drag expressed as a function of $(q/sT)^3$ and experimental measurement [1]

Using the fits obtained for the different bath temperatures; we can solve and express the Drag coefficient as a function of temperature. The coefficients, a, of the linear trend lines (Drag = a.T), obtained for the experimental temperature levels studied, are listed in Table 5.14.

Finally, using these values, we attempt to express the Drag coefficient as a simple function of the temperature. The best fit that we have obtained is shown below and the errors to the experimental results are compared in Table 5.14.

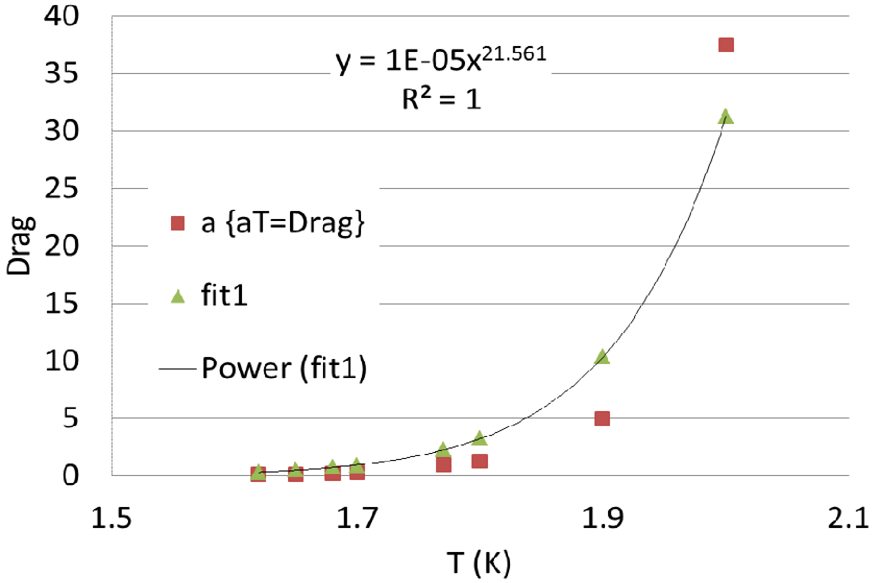

Figure 5.24: Drag coefficient expressed as a function of the temperature

Table 5.14: Data for solving the linear fit, Drag=a.T

T	a	fit	error
1.62	0.1495	0.333	0.18
1.65	0.1771	0.494	0.32
1.68	0.2526	0.729	0.48
1.7	0.334	0.941	0.61
1.77	0.968	2.246	1.28
1.8	1.2758	3.226	1.95
1.9	5.032	10.35	5.32
2	37.46	31.28	-6.18

fit {aT=Drag}	
Drag=c1*T^{c2}	
c1=	1.0109E-05
c2=	21.5613799

Numerical results expressing the normal velocity field and the above expression of the drag coefficient could be used to further analyze experimental results. Several approximations and assumptions have been considered in this section, e.g. according to the scaling analysis, we have neglected the viscous term in order to obtained Eq. 5.18; we assume an ideal flow in order to use the London's equation and obtained Eq. 5.20a and Eq. 5.20b. Providing that the above assumptions are corrects, the particle friction can be obtained as a Gorter-Mellink equivalent expression as shown in Eq. 5.22.

6 OPENING TO FUTURE STUDIES

The study presented in this dissertation offers a powerful numerical tool to analysis the hydro-dynamics behavior of Helium II up to a 3-D space. The test cases studied above make use of coarse meshes, hence allowing to use a simple PC with short computer time. For the sake of precision it would be interesting to compare those results with refined meshes obtained with supercomputers or larger computational capacity. e.g. Section 5.7.2. exhibits results of a 3-D mesh, which cannot describe large eddy structure in 3-D due to the resolution of the model. If a refined mesh was available, this study could enhance the understanding of the drag coefficient and the whole PIV measurement technique.

The qualitative results obtained in Section 5.7.3. need to be refined. If we assume that the phenomenological friction term introduced by Gorter and Mellink is appropriate for thermal counterflow in Helium II, we could express the drag coefficient as the sum of a viscous-like term and a Gorter-Mellink-like term. The scale of those two terms could be further analyzed w.r.t. experimental and numerical results. The final analysis could confirm the Gorter-Mellink equivalent expression for particle friction.

In other words, a deeper understanding of the influence of the drag coefficient would permit to model results of the PIV measurement using the macroscopic approximation of the two-fluid model.

Numerous additional subjects could be explored using the new 3DHeliumSolver, e.g.: one of the important tests is to include forced flow ($v > 0$) solutions. For that matter we would not neglect the viscous term in the governing equations.

7 CONCLUSION

A new derivation of Helium II hydrodynamics approximations based on the two-fluid model and the theory of Gorter-Mellink mutual friction was presented and summarized. Qualitative and quantitative examples were chosen to validate the 3DHeliumSolver. We were able to reproduce experimental results obtained in a 1-D, 2-D and 3-D spaces.

A new set of equations were developed to account for explicit variables; pressure, normal and super-fluid component velocities and temperature. The use of these variables has the advantage that the forcing terms in the equations are implicitly solved. Specifically, pressure is the driver of flow, while temperature drives heat flux. Using these as variables achieves a large degree of stabilization in the numerical solution without resorting to special techniques, or iterations. This can be used to increase the time step much beyond the Courant limit (by one to two orders of magnitude) and still achieve stable solutions, and can be applied if the scale of sound propagation is not of direct interest in the solution, which is the case for quasi-steady-state heat transfer in He-II. The governing equations involved are highly non-linear, implying challenging numerical analyses. The numerical implementation in the three-dimensional solver of the resulting system of partial differential equations converges based on the Finite Element technique.

The modeling principles necessitated transforming a portion of an existing one-dimensional code to a two- dimensional and three-dimensional code capable of solving hydro- and thermo-dynamics problems, e.g. convection-diffusion and Euler flow. A staged approach was used to construct the package 3DHeliumSolver assuring that the algorithms were sufficiently stable and robust to solve the generic PDEs. The most desired results to validate this code is a quantitative and qualitative modeling of the problem arising from experimental measurements exhibiting unique properties the Helium II. While optimizing the computing time, powerful algorithms permit the modeling conditions of Helium II flow based on the *Landau-Khalatnikov* two-fluid model.

Test cases were chosen to validate the new model, namely the calculation of the speed of second sound and heat transfer by thermal counterflow. Numerical results agree within 4 % with predictions in the temperature range of interest. We have shown that internal convection can be successfully simulated, and provide the opportunity to explore further experimental results in 2-D and 3-D spaces. A qualitative study includes the observation of a large eddy structure generated by thermal counterflow passing a cylinder. The 3DHeliumSolver can reproduce similar behavior of the Helium II dynamics observed using PIV technique. The 2-D simulation allows us to extract the temperature profiles and the distinct velocity fields and might be used as an additional diagnostic tool for analyzing the results of the experiment. Although the convective term and the viscous terms are neglected in the governing equation, the flow passing the cylinder doesn’t exhibit the behavior of the Euler flow; instead convective-type cells appear upstream or downstream of the cylinder. It is worth noticing that the choice of the boundary conditions impacts the position of the large structure. For large heat flux, we observe the enhancement of one of the two large structures, opening the queries to simulate various conditions in order to better understand the phenomenological behavior of Helium II.

The current results make use of a basic computing capacity, e.g. dual core, Intel® processor, 2.2 GHz, 4 GB of installed memory (RAM). The approximations elected for the development of the software allow its use on a simple PC with short computer time, making it the first user-friendly tool available to the whole applied cryogenics community.

8 REFERENCES

[1] T. Zhang, A Study of Thermal Counterflow in he II Using Particle Image Velocimetry (PIV) Technique, PhD dissertation, Florida State University, 2004.

[2] M. Raffel, C. Willert and Komenhans, Particle Image Velocimetry, Springer, 1998.

[3] S. W. van Sciver, Helium Cryogenics, The international cryogenics monograph series, editor: K.D. Timmerhaus and A. F. Clark, (1986), S.W. Van Sciver, Helium Cryogenics, Plenum Press, 1986.

[4] T. Zhang, D. Celik, Steven van Sciver, Application of PIV to Counterflow in Helium II, Advances in Cryogenic Engineering, 47B, pp. 1372-1379, 2001.

[5] T. Zhang, S. W. Van Sciver, Large-scale turbulent flow around a cylinder in counterflow superfluid 4He (He(II)), Nature, pp. 38-39, Sep. 2005.

[6] C. Darve, N.A. Patankar, S.W. Van Sciver, A 3-D model of superfluid helium suitable for numerical analysis Presented at the International Cryogenic Engineering Conference (ICEC 22) 2008. Proceeding of the ICEC-ICMC2008, ISBN 978-89-957138-2-2, Fermilab-conf-08-695-AD, 2008.

[7] C. Darve, L. Bottura, N.A. Patankar and S.W. Van Sciver, A method for the three-dimensional numerical simulation of Superfluid Helium; Presented at the international Low Temperature Physics conference (LT25) 2008. Journal of Physics: Conference Series; Volume 150, Fermilab-conf-08-696-AD, 2008.

[8] C. Darve, L. Bottura, N.A. Patankar and S.W. Van Sciver, A Method for Numerical Simulations of Superfluid Helium; Presented at the Cryogenic Engineering Conference, 2011.

[9] R. H. Donnelly , On the Hydrodynamics of Superfluid Helium, PhD thesis, Yale University, *1956*.

[10] Ph. Lebrun, Helium II cryogenics for the Large Hadron Collider project at CERN, Cryogenics 34 ICEC Supplement 1-8, 1994.

[11] L. Tisza, Transport Phenomena in Helium II, Nature, 141, 913, 1938.

[12] L.D. Landau, The Theory of Superfluidity of Helium II, J. Phys. U.S.S.R., 5, 71, 1941.

[13] I.M. Khalatnikov, An Introduction to the Theory of Superfluidity, Frontiers in Physics Series, Benjamin, 1965.

[14] C.J. Gorter, J.H. Mellink, On the Irreversible Processes in Liquid Helium II, Physica, XV, three-4, 285-304, 1949-[Gorter-1949] C.J. Gorter, J.H. Mellink, On the Irreversible Processes in Liquid Helium II, Physica, XV, 3-4, 285-304, 1949.

[15] P.H. Roberts, R.J. Donnelly, Superfluid Mechanics, Ann. Rev. Fluid. Mechanics, 6, 179-225, 1974.

[16] V. Arp, Heat Transport Though Helium II, Cryogenics, 10, pp. 96-105, 1970.

[17] L. Bottura, THEA 1.3 User’s Guide, Cryosoft, 2003.

---

[18] C. Hirsch, Numerical Computation of Internal and External Flows, 1 & 2, A. Wiley International Publication, 1988.

[19] D.R Poole, C.F. Barenghi, Y.A Sergeev and W.F. Vinen, The motion of tracer particles in helium II, to be submitted to Cryogenics, 2005.

[20] H. Kamerlingh Onnes, The liquefaction of helium, Communications from the Physical Laboratory at the University of Leiden 108, 1908.

[21] H. Kamerlingh Onnes, Further Experiments with Liquid Helium. G. On the Electrical Resistance of Pure Metals, etc. VI. On the Sudden Change in the Rate at which the Resistance of Mercury Disappears, Communications from the Physical Laboratory at the University of Leiden 124, p. 21, 1911.

[22] P. Kapitza, Nature, vol. 141, p. 74, 1938.

[23] Collected Papers of P.L. Kapitza, vol. 3, Pergamon Press, Oxford, 1967.

[24] G.G. Haselden, Cryogenic Fundamentals, Academic Press, London, 1971.

[25] G. Claudet, R. Aymar, Tore Supra and Helium II cooling of large high-field magnets, Adv. Cryo. Eng. , vol. 35A, pp. 55-67, 1990.

[26] C.H. Rode, CEBAF cryogenic system, paper presented at PAC'95, Dallas, 1995.

[27] C. Darve et al., Commissioning and First Operation of the Low-Beta Triplets and its Electrical Distribution Feed-Boxes at the Large Hadron Collider (LHC), Presented at the CEC 2009.Advances in Cryogenic Engineering, vol 54, 2009.

[28] W. Soyars, C. Darve, T. Nicol, A. Rowe Design, Fabrication, and Test of an SRF Cryomodule Prototype at Fermilab — Published in *Advances in Cryogenic Engineering* 51B, edited by J. Weisend II et al., Melville, New York, 2006, pp. 1172-1180– AIP ISBN 0-7354-0317-1, 2006.

[29] M. Lindroos et al., The ESS Accelerator, submitted to the SRF 2011 conference, Chicago, 2011.

[30] R.P Feynman, Application of quantum mechanics to liquid helium, Progress in Low Temperature Physics, 1, 17-53, 1955.

[31] D.R. Tilley, J. Tilley, Superfluidity and Superconductivity, Third Edition, Institute of Physics Publishing, Bristol, 1990.

[32] C. Kittel and H. Kroemer, Thermal physics, second edition, San Francisco, 1980.

[33] R. Abusaidi et al., Exclusion Limits on the WIMP-Nucleon Cross-Section from the Cryogenic Dark Matter Search, CWRU-P5-00/UCSB-HEP-00-01, 2001.

[34] S. Fuzier, B. Baudouy and S. W. Van Sciver, Steady-state pressure drop and heat transfer in Helium II forced flow at high Reynolds number, Cryogenics, vol. 41, pp. 453-458, 2001.

[35] R.B. Dingle, The Hydrodynamics of Helium II, Proc. Phys. Soc. 10-A, 62, 648-655, 1949.

[36] C. Darve, E. Blanco, Y. Huang, T. Nicol, T. Peterson, R. van Weelderen, Helium II heat exchanger test unit for the LHC inner triplet, Adv. Cryo. Eng., vol. 47B, pp. 147-154, 2001.

[37] G. Bon Marion et al., Practical data on steady state heat transport in superfluid helium at atmospheric pressure, Cryogenics, vol. 19,pp. 45-47, 1979.

[38] B. Hebral et al., Cryogenie, ses applications en supraconductivite, Techniques de l'Ingenieur, Institut International du Froid, Paris, 1995.

[39] A. Kashani, S.W. Van Sciver, Steady State Forced Convection Heat Transfer in Helium II, Adv. Cryo. Eng., vol. 31, p. 489, 1986.

[40] W. F. Vinen and J. J. Niemela, Quantum Turbulence, Journal of Low Temp. Phys., 128, 167, 2002.

[41] C. Darve, Y. Huang, T. H. Nicol and T. J. Peterson, Experimental Investigations of Helium II Heat Transfer through a Short Section of LHC inner triplet Quadrupole Heat Exchanger, IEEE transactions on Applied Superconductivity, vol. 11, pp 1629-1632, 2000.

[42] R.J. Donnelly, Cryogenic Fluid Dynamics, J. Phys: Condens. Matter, 11, 7783-7834, 1999.

[43] D.V. Osborne, The Rotation of Liquid Helium II, Proc. Phys. Soc., A63, 909, 1950.

[44] W. F. Vinen, Classical character of turbulence in a quantum liquid, Phys. Rev. B, 61, 1410, 2000.

[45] G.A. Williams and R. E. Packard, Photographs of Quantized Vortex Lines in Rotating He II, Phys. Rev. Lett., 33, 280, 1974.

[46] S. K. Nemirovskii and W. Fiszdon, Chaotic quantized vortices and hydrodynamic processes in superfluid helium, Rev of Modern Physics, 67, 37, 1995.

[47] V. Arp, Heat transport though helium II, Cryogenics, vol., pp. 10-96, 1970.

[48] S. van Sciver, Heat and mass transfer processes in two phase He II/vapor, Cryogenics, 1039-1046, 1999.

[49] N.H. Ramadan, R.J. Witt, Natural Convection in Large He II Baths, Cryogenics, 7, 563-577, 1994.

[50] Y.F. Rao, et al., A Two-Fluid-Model Analysis on Transient, Internal-Convection Heat Transfer of He II in a Vertical Gorter-Mellink Duct Heated at the Bottom Surface, Cryogenics, 36, 457-464, 1997.

[51] L. Dresner Transient Heat Transfer in Superfluid Helium- Part II, Advances in Cryogenic Engineering, 29, pp. 323-333, 1984.

[52] Y.F. Rao, K. Fukuda and H. Horie, A two-fluid-model analysis on transient, internal-convection heat transfer of He II in a vertical Gorter-Mellink duct heated at the bottom surface, Cryogenics, 36, pp. 457-464, 1996.

---

[53] Y.F. Rao, Y. Inada, T.Noda and K. Fukuda, Transient characteristics of He II forced flow heated at the center of a pipe line, Cryogenics, 36, pp. 219-224, 1996.

[54] R. Srinivasan and A. Hofmann, Investigations on cooling with forced flow of He II. Part I, Cryogenics, 25, pp. 641-651, 1985 and , Investigations on cooling with forced flow of He II. Part II, Cryogenics, 25, pp. 652-657, 1985.

[55] L. Bottura, A Numerical Model for the Simulation of Quench in the ITER Magnets, Jour. Comp. Phys., 125, pp. 26-41, 1996.

[56] L. Bottura and C. Rosso, Finite Element Simulation of Steady-State and Transient Forced Convection in Superfluid Helium, Int. Jour. Num. Methods in Fluids, 30, pp. 1091-1108, 1999.

[57] F. Richard, J. Schneider, D. Trines, A. Wagner, TESLA Technical Design Report, DESY, 2001.

[58] Y. Xiang, N.N. Filina, S.W. van Sciver, J.G. Weisend II and S.Wolff, Numerical Study of Two-phase Helium II Stratified Channel Flow, Advances in Cryogenic Engineering, 45, pp. 1001-1008, 2000.

[59] G. Horlitz, B. Petersen, D. Sellmann, S.W. van Sciver, J.G. Weisend II, S. Wolff, The TESLA 500 Cryogenic System and helium II Two-phase Flow: Issues and Planned Experiments, Cryogenics, 37, pp. 719-725, 1999.

[60] S. van Sciver, J.S. Panek and D. Celik, Flow in horizontal two-phase He II / vapor, Applied in Cryogenic Engineering, 45, pp. 99three-1000, 2000.

[61] Y. Xiang, B. Peterson, S. Wolff, S. vanSciver, J. Weisend II, Numerical Study of Two-phase Helium II Stratified Channel Flow with Inclination, IEEE Transactions on Applied Superconductivity, 10 no. 1, 2000.

[62] N.H. Ramadan and R.J.Witt, Natural convection in large He II baths, Cryogenics, 34, pp. 563-577, 1994.

[63] R.J. Witt, Toward a self-consistent solution of the He II Mass momentum and energy equations, Advances in Cryogenic Engineering, 37A, pp. 63-71, 1992.

[64] T. Kitamura, et al., A Numerical Model on Transient, Two-dimensional Flow and Heat Transfer in He II, Cryogenics, 37, 1-9, 1997.

[65] T. Kitamura, K. Shiramizu, N. Fujimoto, Y.F. Roa and K. Fukuda, A Numerical Model on transient, two-dimensional flow and heat transfer in He II, Cryogenics, 37, pp. 1-9, 1997.

[66] H. Tatsumoto, K. Fukuda and M. Shiotsu, Numerical analysis for two-dimensional transient heat transfer from a flat plate at one-side of a duct containing pressurized He II, Cryogenics, 42, pp. 19-28, 2002.

[67] H. Tatsumoto, K. Fukuda and M. Shiotsu, Numerical analysis for steady-state two-dimensional heat transfer from a flat plate at one-side of a duct containing pressurized He II, Cryogenics, 42, pp. 9-17, 2002.

[68] D. Doi, Y. Shirai, andM. Shiotsu, 3D Numerical analysis for heat transfer from a flat plate in a duct with contractions filled with pressurized He II, Advances in Cryogenic Engineering, 53 648-655, 2007.

[69] V. Arp, New forms of state equations for helium, Cryogenics, 14, pp. 593-599.

[70] Alain Herve, Etude des Transferts thermiques dans les milieux poreux en hélium superfluide, PhD dissertation, February 2010.

[71] C. T. Lane, H. A. Fairbank, and W. M. Fairbank, Second Sound in Liquid Helium II, Phys. Rev. 71, 600–605, 1947.

[72] G. Amberg and H.P. Greenspan, Boundary layers in a sectioned centrifuge, Journal of Fluids Mechanics, vol. 181, 1987.

[73] C.E. Willert and M. Ghari, Digital particle image velocimetry, Experiments in Fluids, vol. 10, pp. 181-193, 1991.

[74] S.W. Van Sciver · S. Fuzier · T. Xu, ,Particle Image Velocimetry Studies of Counterflow Heat Transport in Superfluid Helium II, J Low Temp Phys 148: 225–233, DOI 10.1007/s10909-007-9375-0, 2007.

[75] T. Zhang and S. W. Van Sciver, The motion of micron-sized tracer particles in He II thermal counterflow as observed by the PIV technique, J. Low Temp. Phys., Vol. 138, p. 865, 2005

[76] M. Paoletti, Experimental Characterization of Turbulent Superfluid Helium, PhD dissertation, University of Maryland, 2010.

[77] D. R. Poole, C. F. Barenghi, Y. A. Sergeev, and W. F. Vinen, Motion of tracer particles in He II, PHYSICAL REVIEW B 71, 064514 s2005d, 2005.

[78] Choi, Y.S.; Smith, M.R. and Van Sciver, S.W., A Study on the Temperature Dependent Drag Coefficient on a Sphere in Flowing Helium II, Adv. Cryog. Eng., 47B, 1335-1342, 2002.

APPENDICES

1.1 Notation for the Differential Operators

The following convention has been used for operator application ∇ to a scalar *s*, a vector **v** and a matrix $\overline{\overline{\mathbf{m}}}$:

$$\nabla s = \begin{bmatrix} \dfrac{\partial s}{\partial x} \\ \dfrac{\partial s}{\partial y} \\ \dfrac{\partial s}{\partial z} \end{bmatrix} \text{(gradient)} \tag{AI.1}$$

$$\nabla \cdot \mathbf{v} = \frac{\partial v_x}{\partial x} + \frac{\partial v_y}{\partial y} + \frac{\partial v_z}{\partial z} \text{ (divergence)} \tag{AI.2}$$

$$\nabla \cdot \overline{\overline{\mathbf{m}}} = \begin{bmatrix} \dfrac{\partial m_{xx}}{\partial x} + \dfrac{\partial m_{xy}}{\partial y} + \dfrac{\partial m_{xz}}{\partial z} \\ \dfrac{\partial m_{yx}}{\partial x} + \dfrac{\partial m_{yy}}{\partial y} + \dfrac{\partial m_{yz}}{\partial z} \\ \dfrac{\partial m_{zx}}{\partial x} + \dfrac{\partial m_{zy}}{\partial y} + \dfrac{\partial m_{zz}}{\partial z} \end{bmatrix} \tag{AI.3}$$

$$s\nabla \cdot \mathbf{v} = s\frac{\partial v_x}{\partial x} + s\frac{\partial v_y}{\partial y} + s\frac{\partial v_z}{\partial z} \tag{AI.4}$$

$$\mathbf{v} \cdot \nabla s = \mathbf{v_x}\frac{\partial \mathbf{s}}{\partial \mathbf{x}} + \mathbf{v_y}\frac{\partial \mathbf{s}}{\partial \mathbf{y}} + \mathbf{v_z}\frac{\partial \mathbf{s}}{\partial \mathbf{z}} \tag{AI.5}$$

$$\mathbf{v}\nabla \cdot \mathbf{v} = \begin{bmatrix} v_x\dfrac{\partial v_x}{\partial x} + v_y\dfrac{\partial v_x}{\partial y} + v_z\dfrac{\partial v_x}{\partial z} \\ v_x\dfrac{\partial v_y}{\partial x} + v_y\dfrac{\partial v_y}{\partial y} + v_z\dfrac{\partial v_y}{\partial z} \\ v_x\dfrac{\partial v_z}{\partial x} + v_y\dfrac{\partial v_z}{\partial y} + v_z\dfrac{\partial v_z}{\partial z} \end{bmatrix} \tag{AI.6}$$

$$\overline{\overline{\mathbf{m}}}\nabla \cdot \mathbf{v} = \mathrm{m}_{xx}\frac{\partial v_x}{\partial x} + \mathrm{m}_{xy}\frac{\partial v_x}{\partial y} + \mathrm{m}_{xz}\frac{\partial v_x}{\partial z} + \mathrm{m}_{yx}\frac{\partial v_y}{\partial x} + \mathrm{m}_{yy}\frac{\partial v_y}{\partial y} + \mathrm{m}_{yz}\frac{\partial v_y}{\partial z} + \mathrm{m}_{zx}\frac{\partial v_z}{\partial x} + \mathrm{m}_{zy}\frac{\partial v_z}{\partial y} + \mathrm{m}_{zz}\frac{\partial v_z}{\partial z}$$

(AI.7)

1.2 Artificial Diffusion detailed study

If we add a classical isotropic diffusion in the pressure, velocities and temperature equations of our PDE system, the coefficient will be expressed as

$$c_{art} = \delta_{id} h|\beta| \qquad \text{(AII.1)}$$

where δ_{id} is the tuning parameter, equal to 0.5 by default, h is the mesh size and β is the convective velocity vector.

The characteristic parameter of such a fluid flow is the Peclet number, which can then be expressed as

$$Pe = \frac{h|\beta|}{2(c + c_{art})} = \frac{h|\beta|}{2c + h|\beta|} \qquad \text{(AII.2)}$$

For our third study of 3DHeliumSolver integration and modeling abilities w.r.t. convection-diffusion we yet again turn our attention to the general convection-diffusion equation:

$$\frac{\partial u}{\partial t} + v\frac{\partial u}{\partial x} - \alpha\frac{\partial^2 u}{\partial x^2} = 0 \qquad \text{(AII.3)}$$

This is the well-known trouble maker which has kept numericists active for several years [18]. The model chosen could represent the propagation of a temperature wave (*u* is the unknown, i.e. temperature) in a fluid that moves with velocity *v* and has diffusivity α, under the assumption that any source term (volume heating, heat transfer at wetted walls) is negligible. Alternatively it could represent convection and diffusion of the density (*u*) of a species in a moving fluid. The structure of the model equation is that of a parabolic partial differential equation (PDE), reducing to first order pure convection when α=0. We call this case the hyperbolic limit of the equation (in analogy with the wave propagation phenomena in hyperbolic second order equations). In the case that the fluid is at rest, i.e. $v = 0$, the model equation reduces to second order pure diffusion. Depending on the values of v and α the wave propagation will be of *diffusive* type or *convective* type. In correspondence, the value of the Peclet number *Pe* , defined as

$$Pe = \frac{\mathrm{v}L}{\alpha} \qquad \text{(AII. 4)}$$

ranges from 0 (for pure diffusion) to ∞ (for pure convection). An example of a solution of a convective diffusive problem is given in Fig. AII.1 (below) for various values of *Pe*. From the mathematical point of view, a real change in the character of the solution to the Eq. AII.3 is seen only at the limiting case of $Pe=\infty$, where the order of the PDE decreases and the solution changes functional class. In practice, numerical solution of the equation above will be increasingly difficult at increasing Peclet number, i.e. tending from pure diffusion to pure convection. This is the reason why special numerical techniques must be used to deal with convection diffusion problems.

To gain insight in the more fundamental reasons for the difficulties, we look at the general properties of the exact solutions of Eq. AII.3. The solution of a PDE of the type of Eq. AII.3 in the general case of finite diffusivity belongs to the Hilbert space[78] H^1, meaning that it is continuous and that its derivative belongs to L_2. In fact, in most of the cases, the solution belongs to H^2, (i.e. both the first and second derivatives of the solution belong to L_2). This fact expresses the fundamental *regularity* of the diffusion process. In the hyperbolic limit, however, the solution lies in the Hilbert space H^0 meaning that it belongs to L_2, but that its derivative in general does not. The physical phenomenon indicating this loss of regularity is the appearance of *shocks* (discontinuities) in the solution, as often encountered in inviscid and viscous fluid flow simulations [18].

Let us now take the model problem, Eq. A. AII.3 above, and, following normal practice in the frame of Finite differences [18], substitute a second order approximation in space and time of the derivatives. We can then solve numerically for the same conditions presented in Fig. AII.1 (in the case of Pe=∞). The results are shown in Fig. AII.2. Evidently, the exact solution is strongly deformed, oscillations appear at the front and the sharp front itself is smeared.

With the intention of curing some of these problems, the concept of *upwind* differencing was introduced. Upwinding consists in taking one-sided differences for the first-order space derivative, biased along the velocity direction, justifying this approximation with the fact that a moving fluid can only be affected by what is coming along the characteristic lines (i.e. what is *upstream*). The use of one-sided differences results in a strong damping of the oscillations, but also in a further deformation of the shape of the front, a smearing in the space profile, as shown in Fig. AII.3. This is caused by the fact that this upwind method can only be accurate to first order in space. Physically, this corresponds to adding a spurious second order space derivative term to the equation, i.e. a diffusion. We saw in Fig. AII.1 that the effect of a diffusion in Eq. AII.3 is the front smearing, exactly as observed in the numerical simulation of Fig. AII.3.

With similar reasoning, we expect a second order numerical scheme to be free from spurious diffusion in the solution. However in this case the error appears as a third order space derivative, which is equivalent to a *dispersion*, a scattering in the modes into which the solution can be decomposed. For the initial condition of a step function the mode decomposition has a very high frequency content, so that a dispersion generates significant wiggles around the front.

Although the model problem Eq. AII.3 is very simple, it generates the full spectrum of problems associated with hyperbolicity. A general conclusion that can be drawn from the above observations is that while second order methods provide a better definition of the front sharpness, compared to the first order upwind methods, they will result inevitably in wiggles in the solution. So far, however, a pure phenomenological explanation is given. The deeper question is why first order hyperbolic equations pose such difficulties, in contrast e.g. to second order, parabolic problems where standard second-order differencing results in fully satisfactory algorithms.

Such a question can be explained elegantly in the context of finite elements (FE). The Galerkin weighted approach generates a nodal equation which is identical to that obtained by finite difference (FD) central differencing. It follows that the properties of a FE approximation can be directly extended to the corresponding FD approximation. Generally the FE solution of a differential equation consists of functions belonging to H^1, e.g. piecewise continuous polynomials, with discontinuous but integrable derivatives over the discretized domain. But as we noted above the general solution to a first order hyperbolic problem is in a wider class of function, namely H^0. This means that both centered FD and Galerkin FE look for a solution in a class of functions that does not necessarily contain the exact solution to the problem. In other words, both methods try to approximate the problem as best as they can do, but using functions that are not *discontinuous* enough to represent the real solution. As it is the case for an unstable interpolation of a set of points, the interpolating function fails, wiggles are generated (trailing/leading waves) and the solution can indeed become unstable.

On the other hand, it can be proven that the use of the FD upwinding in the context of a more general class of FE approximations (Petrov-Galerkin weighting) corresponds to a transformation of the equation to be solved into a *better behaved* system[78], which, in particular steady-state cases, can be solved exactly by FE (and proper FD upwinding). Again, in other words, the functional class to which the solution belongs is lowered so that a well-behaved approximation can be found. This procedure, however, is applicable only to the steady-state limit, and so far no general *optimal* procedure could be found for the transient case.

For the moment we conclude that a standard solution of a first-order hyperbolic problem implies fundamental difficulties in the definition of moving fronts, where these are either affected by spurious diffusion (which makes the solution monotonous) or by oscillations, however, various techniques can be employed to address this situation.

Figure AII.1. Solution to the convection-diffusion model problem Eq. AII. 3 in the domain x=[-∞...∞] for a step in the unknown at x=0 and different values of the Pe number. Pe=0 corresponds to pure diffusion, Pe=∞ to pure convection. Constant properties are assumed in the solution. The arrow marks the increasing time direction.

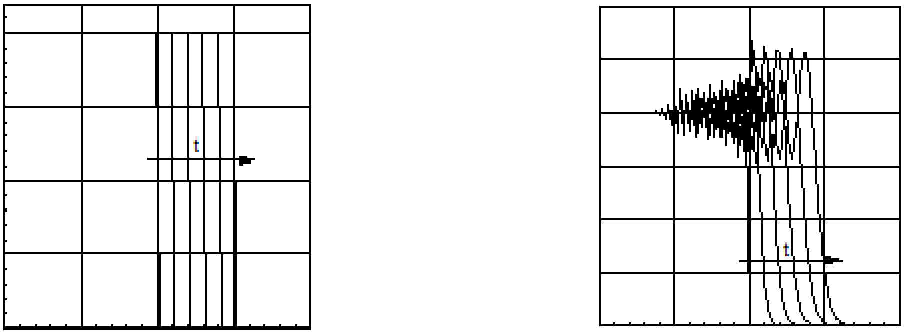

Figure AII.2. Numerical solution of the convection-diffusion model problem Eq. AII. 3 obtained with a FD scheme of second order accuracy in space and time (central differences). The arrow marks the increasing time direction.

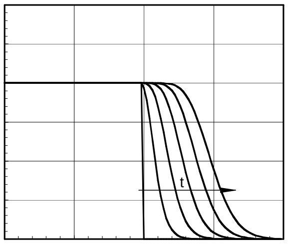

Figure AII.3. Numerical solution of the convection-diffusion model problem Eq. AII. 3 obtained with a FD scheme of first order accuracy in space (upwind differences) and time (backward differences). The arrow marks the increasing time direction.

1.3 Particle Dynamics in a Fluid Flow

A necessary condition for the PIV measurement to yield accurate results is that the particle motion imaged is as close as possible to the fluid motion to be measured [78][78]. This condition is usually expressed in terms of the maximum slip velocity [78]. To assess the dependence of the slip velocity on the particle characteristics and on the flow conditions we need to examine in some detail the dynamics of a particle in a fluid flow.

In general the particle motion is determined by the equilibrium of the particle inertial force, the drag force $\mathbf{F}_D$ exerted by the fluid on the particle, the body force $\mathbf{F}_B$ due to the density difference between fluid and particle, and the force $\mathbf{F}_A$ caused by pressure gradients due to fluid acceleration [78]. For simplicity, in the following we consider the case of rigid spheres floating in a 1-D flow field, so that the vector force and velocity fields reduce to scalars.

The drag force F_D on a particle moving in a fluid can be written in general as

$$F_D = \frac{1}{2} C_D Area \rho_f (U - X')^2 \qquad \text{(AIII.1)}$$

where C_D is the drag coefficient, *Area* is the projected area of the particle and ρ_f is the fluid density. In general the drag coefficient can be obtained using experimental correlations.

In the limit of small flow Reynolds number (Re < 0.1), the drag coefficient is given by

$$C_D = \frac{24}{\mathrm{Re}} \qquad \text{(AIII.2)}$$

and the Reynolds number of the relative flow of the fluid around the particle is defined as

$$\mathrm{Re} = \frac{\rho_f (U - X') D}{\mu} \qquad \text{(AIII.3)}$$

where D is the particle diameter and μ is the fluid viscosity. In the case of higher Reynolds number, Re > 0.1, various correlations can be found in literature. Several of them can be cast in the following form

$$C_D = \frac{24}{\mathrm{Re}}\left(1 + f\left(\mathrm{Re},\mathrm{Kn}\right)\right) \qquad \text{(AIII.4)}$$

which is a correction of Eq. AIII.1 through a simple function *f* of the Reynolds number and of the Knudsen number Kn (the Knudsen number is the non-dimensional ratio of the molecular free path and a characteristic length of the flow, and is a measurement of the rarefaction of the flow).

The body force F_B is computed in general as follows

$$F_B = aV(\rho_p - \rho_f) \qquad \text{(AIII.5)}$$

where *a* is the acceleration, *V* is the particle volume and ρ_p is the particle density. Note that with the convention chosen in Eq. 6 a positive acceleration along x will result in a positive force in the case of particles heavier than the fluid.

In an unsteady flow an additional force F_A arises on the particle

$$F_A = V\rho_f \frac{dU}{dt} + \frac{1}{2}V\rho_f \frac{d\left(U - X'\right)}{dt} \qquad \text{(AIII.6)}$$

where the first term is due to the pressure gradient due to the flow acceleration, while the second term is the acceleration force of the *virtual mass* of fluid, equal to half of the mass displaced by the particle.

The equilibrium condition for a particle can be finally written as follows

$$\rho_p V \frac{dX'}{dt} = F_D + F_B + F_A \qquad \text{(AIII.7)}$$

or, using Eqs. AIII.1, AIII.6 and AIII.7.

$$\rho_p V \frac{dX'}{dt} = \frac{1}{2} C_D Area \rho_f (U - X')^2 + aV(\rho_p - \rho_f) + V\rho_f \frac{dU}{dt} + \frac{1}{2}V\rho_f \frac{d\left(U - X'\right)}{dt} \text{(AIII.8)}$$

Eq. AIII.8 is the general equation governing the motion of a particle in a flow field, and is usually referred to as the Basset-Boussinesq-Oseen (BBO) equation [18]. Note that in the form reported above we have neglected the Basset history term (tracing the effect of drag in the case of unsteady flow). We can finally group terms and substitute for the expression of the drag coefficient Eq. AIII.4 and the Reynolds number Eq. AIII.3 to derive the equation for the particle velocity:

$$\overline{\rho}\frac{dX'}{dt}=\frac{18\mu}{D^2}\left[1+f(\mathrm{Re},\mathrm{Kn})\right](U-X')+\frac{3}{2}\rho_f\frac{dU}{dt}+a(\rho_p-\rho_f) \qquad \text{(AIII.9)}$$

where we have introduced for convenience an *effective* particle density, given by

$$\overline{\rho}=\rho_p+\frac{1}{2}\rho_f \qquad \text{(AIII.10)}$$

Eq. AIII.10 determines the evolution of the particle velocity in a known flow field, and can hence be used to study the dependence of the slip velocity on the various parameters and measurement conditions. This is done in the following sections, where we will consider some special, relevant cases for which analytical solutions are found easily.

Negligible body forces, small Reynolds number

We start our analysis by making the assumption that the effect of the acceleration field (gravitational, centrifugal) is negligible, i.e. the body force on the particle is much smaller than the force due to drag, pressure gradients and the particle acceleration in the flow field [78]. This is the case when the acceleration field is small compared to the particle acceleration in the flow, or when the particle density is identical to that of the fluid. We consider in addition that the Reynolds number is small, below 0.1, so that the drag is given by Eq. AIII.2. In this case the equation for the particle motion AIII.9 can be simplified as follows

$$\frac{dX'}{dt}+\frac{1}{\tau_{slip}}X'\approx\frac{1}{\tau_{slip}}U+\frac{3}{2}\frac{\rho_f}{\overline{\rho}}\frac{dU}{dt} \qquad \text{(AIII.11)}$$

The time constant τ_{slip}, appearing in Eq. 11) governs the relaxation of the slip velocity and is given by

$$\tau_{slip}\approx\frac{D^2\overline{\rho}}{18\mu}=\left(1+\frac{1}{2}\frac{\rho_f}{\rho_p}\right)\tau_0 \qquad \text{(AIII.12)}$$

where the time constant τ_0 is defined as

$$\tau_0=\frac{D^2\rho_p}{18\mu} \qquad \text{(AIII.12a)}$$

and represents the limit obtained for particle density much larger than the fluid density.

The analytic solution of Eq. AIII.11 is obtained as the sum of two functions: the general solution of the homogeneous equation X'_H (i.e. without forcing term) and a solution for the non-homogeneous equation X'_{NH}

$$X' = X'_H + X'_{NH} \tag{AIII.13}$$

The homogeneous solution X'_H is independent of the forcing term, and is given by

$$X'_H = C_1 e^{-\frac{t}{\tau_{slip}}} \tag{AIII.14}$$

where C_1 is an integration constant. The non-homogeneous solution, on the other hand, depends on the specific fluid flow velocity $U(t)$ considered. We consider here two conditions that are useful to study the slip velocity and the velocity error in a PIV measurement:

- sinusoidal fluid velocity fluctuations $U = U_o \sin(\omega t)$, representative of changes in the fluid flow at a given frequency $f=\omega/2\pi$ that we wish to follow accurately;
- injection of particle at rest in a steady flow (step response), providing an estimate of the time and displacement necessary for the particles to reach steady-state conditions.

1.3.1.1 Sinusoidal flow oscillation

The forcing term in the particle equation is given by an oscillating fluid flow [78]

$$U = Uo \sin(\omega t) \tag{AIII.15}$$

and we choose as initial condition to have the particles at rest (as the fluid) at t=0

$$X'(0) = U(0) = 0 \text{ (particle at rest)} \tag{AIII.16}$$

The non-homogeneous solution for this case is

$$X'_{NH} = C_2 \sin(\omega t + \phi) \tag{AIII.17}$$

where C_2 is the amplitude of the particle response in regime conditions (i.e. for long times compared to the time constant τ_{slip}) and ϕ is the phase lag. The general solution for the particle velocity is then

$$X' = C_1 e^{-\frac{t}{\tau_{slip}}} + C_2 \sin(\omega t + \phi) \quad \text{(AIII.18)}$$

The integration constants *C₁* and *C₂* and the phase ϕ lag are determined using the initial condition Eq. AIII.16) and by requesting that Eq. AIII.18 is a solution of Eq. AIII.11. The first of these two conditions is written as follows

$$C_1 + C_2 \sin(\phi) = 0 \quad \text{(AIII.19)}$$

while the second condition results in

$$\omega C_2 \cos(\omega t + \phi) + \frac{C_2}{\tau_{slip}} \sin(\omega t + \phi) = \frac{1}{\tau_{slip}} U_0 \sin(\omega t) + \frac{3}{2}\frac{\rho_f}{\overline{\rho}} \omega U_0 \cos(\omega t) \quad \text{(AIII.20)}$$

The two conditions can be used to compute an explicit expression for the integration constants and the phase lag, resulting after some algebra in

$$C_1 = \frac{St \dfrac{1-a}{1+aSt^2}}{1 + St^2 \dfrac{1-a}{1+aSt^2}} U_0 \quad \text{(AIII.20a)}$$

$$C_2 = \frac{\sqrt{1 + St^2 \left(\dfrac{1-a}{1+aSt^2} \right)^2}}{1 + St^2 \dfrac{1-a}{1+aSt^2}} U_0 \quad \text{(AIII.20b)}$$

$$tg(\phi) = -St \frac{1-a}{1+aSt^2} \quad \text{(AIII.20c)}$$

where we have introduced the Stokes number of the particle as the ratio of the particle slip time constant to the characteristic time of the flow

$$St = \omega \tau_{slip} = \omega \frac{D^2 \overline{\rho}}{18\mu} \quad \text{(AIII.21)}$$

and the dimensionless group a that is a function of the fluid density and the particle effective density

$$a = \frac{3}{2}\frac{\rho_f}{\overline{\rho}} \quad \text{(AIII.21a)}$$

The closed form analytical solution is obtained substituting Eqs. AIII.20a, AIII.20b and AIII.20c in Eq. AIII.13.

Details of the derivation of the integration constants and phase are shown below.

Use the formulae for the sum of arguments in the *sin* and *cos* functions to obtain from AIII.20.

$$\omega C_2\left[\cos(\omega t)\cos(\phi)-\sin(\omega t)\sin(\phi)\right]+\frac{C_2}{\tau_{slip}}\left[\sin(\omega t)\cos(\phi)+\cos(\omega t)\sin(\phi)\right]= \quad \text{(N1)}$$

$$\frac{1}{\tau_{slip}}U_0\sin(\omega t)+\frac{3}{2}\frac{\rho_f}{\bar{\rho}}\omega U_0\cos(\omega t)$$

group terms in sin(wt) and cos(wt)

$$C_2\left[\omega\cos(\phi)+\frac{1}{\tau_{slip}}\sin(\phi)\right]\cos(\omega t)+C_2\left[\frac{1}{\tau_{slip}}\cos(\phi)-\omega\sin(\phi)\right]\sin(\omega t)=$$

$$\frac{1}{\tau_{slip}}U_0\sin(\omega t)+\frac{3}{2}\frac{\rho_f}{\bar{\rho}}\omega U_0\cos(\omega t) \quad \text{(N2)}$$

from (N2) derive two independent equations to be satisfied for the term in sin and the term in cos (sin and cos are two orthogonal functions and the two conditions must be satisfied independently)

$$C_2\left[\omega\cos(\phi)+\frac{1}{\tau_{slip}}\sin(\phi)\right]=\frac{3}{2}\frac{\rho_f}{\bar{\rho}}\omega U_0 \quad \text{(N3)}$$

$$C_2\left[\frac{1}{\tau_{slip}}\cos(\phi)-\omega\sin(\phi)\right]=\frac{1}{\tau_{slip}}U_0 \quad \text{(N4)}$$

the two Eqs. N3 and N4 can be modified as follows (normalization)

$$C_2\left[\omega\tau_{slip}\cos(\phi)+\sin(\phi)\right]=\frac{3}{2}\frac{\rho_f}{\bar{\rho}}\omega\tau_{slip}U_0 \quad \text{(N5)}$$

$$C_2\left[\frac{1}{\omega\tau_{slip}}\cos(\phi)-\sin(\phi)\right]=\frac{1}{\omega\tau_{slip}}U_0 \qquad \text{(N6)}$$

and added to eliminate the term in sin

$$C_2\left[\omega\tau_{slip}+\frac{1}{\omega\tau_{slip}}\right]\cos(\phi)=\left(\frac{3}{2}\frac{\rho_f}{\bar{\rho}}\omega\tau_{slip}+\frac{1}{\omega\tau_{slip}}\right)U_0 \qquad \text{(N7)}$$

Take again the two Eqs. N3 and N4 and modify them as follows (normalization)

$$C_2\left[\cos(\phi)+\frac{1}{\omega\tau_{slip}}\sin(\phi)\right]=\frac{3}{2}\frac{\rho_f}{\bar{\rho}}U_0 \qquad \text{(N8)}$$

$$C_2\left[\cos(\phi)-\omega\tau_{slip}\sin(\phi)\right]=U_0 \qquad \text{(N9)}$$

and subtract them to eliminate the term in cos

$$C_2\left[\frac{1}{\omega\tau_{slip}}+\omega\tau_{slip}\right]\sin(\phi)=\left(\frac{3}{2}\frac{\rho_f}{\bar{\rho}}-1\right)U_0 \qquad \text{(N10)}$$

the ratio of Eqs (N10) and (N7) yields the relation for the tg(ϕ)

$$tg(\phi)=\frac{\frac{3}{2}\frac{\rho_f}{\bar{\rho}}-1}{\frac{3}{2}\frac{\rho_f}{\bar{\rho}}\omega\tau_{slip}+\frac{1}{\omega\tau_{slip}}} \qquad \text{(N11)}$$

To make the notation more compact we introduce a parameter a given by:

$$a=\frac{3}{2}\frac{\rho_f}{\bar{\rho}} \qquad \text{(N12)}$$

and Eq. (N11) can be written as follows:

$$tg(\phi)=-\omega\tau_{slip}\frac{1-a}{1+a\omega^2\tau_{slip}^2} \qquad \text{(N11a)}$$

Using now the trigonometric relation $\cos(\phi)=\frac{1}{\sqrt{1+tg^2(\phi)}}$

in Eq. (N9)

$$C_2 \frac{1-\omega\tau_{slip} tg(\phi)}{\sqrt{1+tg^2(\phi)}} = U_0 \tag{N13}$$

we obtain the following value for the constant C_2

$$C_2 = \frac{\sqrt{1+tg^2(\phi)}}{1-\omega\tau_{slip} tg(\phi)} U_0 \tag{N14}$$

that can be solved explicitly by inserting the result of Eq. (N11)

$$C_2 = \frac{\sqrt{1+\omega^2\tau_{slip}^2 \left(\frac{1-a}{1+a\omega^2\tau_{slip}^2}\right)^2}}{1+\omega^2\tau_{slip}^2 \frac{1-a}{1+a\omega^2\tau_{slip}^2}} U_0 \tag{N15}$$

To compute C_1 we use the trigonometric relation

$$\sin(\phi) = \frac{tg(\phi)}{\sqrt{1+tg^2(\phi)}} \tag{N16}$$

and combine Eqs. (N14), (N16) and the initial condition Eq.(19a), resulting in

$$C_1 = -\frac{tg(\phi)}{1-\omega\tau_{slip} tg(\phi)} U_0 \tag{N17}$$

We finally substitute Eq. (N11) to obtain the explicit solution:

$$C_1 = \frac{\omega\tau_{slip} \frac{1-a}{1+a\omega^2\tau_{slip}^2}}{1+\omega^2\tau_{slip}^2 \frac{1-a}{1+a\omega^2\tau_{slip}^2}} U_0 \tag{N18}$$

A simple expression can be derived in the limit of large particle density, i.e. $\rho_p >> \rho_f$, in which case $a \approx 0$.

In this case the analytical solution is given by:

$$X' = \frac{U_0 St}{1+St^2} e^{-\frac{t}{\tau_0}} + \frac{U_0}{\sqrt{1+St^2}} \sin(\omega t + \phi) \qquad \text{(AIII.22)}$$

and the phase angle is determined by

$$tg(\phi) = -St \qquad \text{(AIII.23)}$$

The physical significance of the results reported in Eqs. AIII.22 and AIII.23 is obvious. After a time large enough compared to the time constant τ_0 the exponential term in Eq. AIII.23 is negligible and a regime oscillation condition is reached. The particle oscillation has a phase lag ϕ and a reduced amplitude compared to the fluid flow. The phase lag and the amplitude reduction increase as the Stokes number increases. This is shown in the two examples reported in Fig. AIII.1, where the instantaneous fluid and particle velocity (normalized with respect to the maximum fluid velocity U_0) are plotted as a function of time (normalized to the oscillation period).

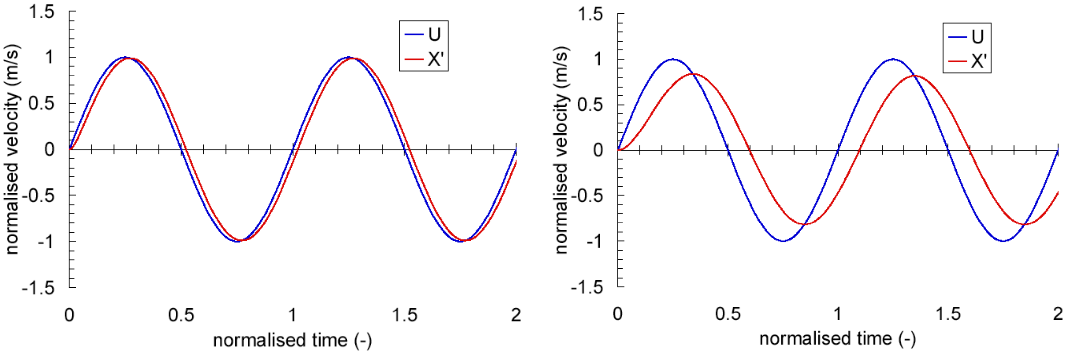

Figure AIII.1: Normalized particle and fluid velocity as a function of normalized time in case of an oscillating flow starting from rest conditions, computed for negligible fluid velocity and for a Stokes number of 0.14 (left) and 0.7 (right).

A useful measure of the slip velocity between particle and fluid is given by the amplitude error for oscillating flow ε, given by

$$\varepsilon = \frac{U_0 - \max\{X'\}}{U_0} = \frac{U_0 - \frac{U_0}{\sqrt{1+St^2}}}{U_0} = 1 - \frac{1}{\sqrt{1+St^2}} = 1 - \frac{1}{\sqrt{1+\omega^2\tau_0^2}} \qquad \text{(AIII.24)}$$

Both the amplitude error, and the phase lag are only a function of the Stokes number. Hence the results above can be summarized as in Figure AIII.2, where the amplitude error of the particle velocity Eq. AIII.24 and the phase lag of the particle with respect to the fluid Eq. AIII.23, normalized to $\pi/2$) are plotted as a function of the Stokes number of the particle motion in the flow. A 1 % amplitude error between fluid and particle velocities corresponds to a Stokes number of 0.143. At this Stokes number the phase lag is approximately 8 degrees.

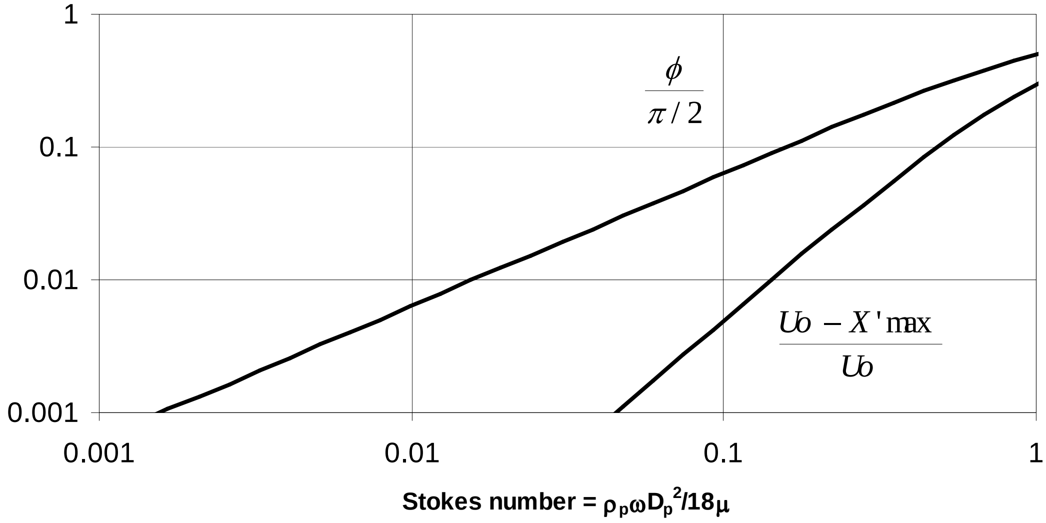

Figure AIII.2: Amplitude error and phase lag for particle motion dominated by drag and particle inertia (negligible body force), plotted as a function of the Stokes number for oscillating flow at angular speed ω.

From Eq. AIII.24 we can derive useful design limits on the cut-off frequency f_c (and the cut-off angular frequency $\omega_c = 2\pi f_c$) of the flow that can be tracked with a given amplitude error, once the particle characteristics (and hence the time constant τ_0) are fixed

$$f_c = \frac{1}{2\pi\tau_0}\sqrt{\frac{1}{(1-\varepsilon)^2} - 1} \qquad \text{(AIII.24a)}$$

The maximum particle diameter D_c that can be used to track a flow at a specified cut-off frequency f_c with a given amplitude error can be derived from Eq. AIII.24a substituting the time constant τ_0 in terms of the particle characteristics, as given by Eq. AIII.12a.

$$D_c = \sqrt{\frac{1}{2\pi}\frac{18\mu}{\rho_p f_c}\sqrt{\frac{1}{(1-\varepsilon)^2}-1}} \qquad \text{(AIII.24b)}$$

Injection of particles initially at rest (step response)

If we consider a steady flow in which particles are injected with initial zero velocity, Eq. AIII.11 simplifies

$$\frac{dX'}{dt} + \frac{1}{\tau_{slip}} X' = \frac{1}{\tau_{slip}} U_0 \qquad \text{(AIII.11a)}$$

and the initial condition is

$$X'(0) = 0$$

The non-homogeneous solution for this case is obvious

$$X'_{NH} = U_0$$

and the general solution for the particle velocity (the constant C_1 is determined through trivial algebra) is

$$X' = U_0\left(1 - e^{-\frac{t}{\tau_{slip}}}\right)$$

This result can be used directly to estimate the time needed to attain a given slip velocity. Using the same definition as in Eq. AIII.24 for the normalized amplitude error, we obtain that in the case of particle injection at rest

$$\varepsilon = \frac{U_0 - X'}{U_0} = \frac{U_0 - U_0\left(1 - e^{-\frac{t}{\tau_{slip}}}\right)}{U_0} = e^{-\frac{t}{\tau_{slip}}} \qquad \text{(AIII.24c)}$$

As for the case of oscillating flow, in the case that $\rho_p \gg \rho_f$ the relaxation time τ_{slip} becomes identical to τ_0. To attain a slip of 1 % or less after injecting particles initially at rest the time needed t_c is

$$t_c = 4.6\tau_{slip} \tag{AIII.24d}$$

During this time the particle travels a distance L_c

$$L_c = 4.6\tau_{slip}U_0 \tag{AIII.24e}$$

Shorter relaxation times and distances can be obtained injecting particles with a velocity closer to that of the fluid.

1.3.1.2 *Dominating body forces, small Reynolds number*

Another case of interest for design and sizing purposes is obtained assuming that the particle dynamics is dominated by the drag and body force, neglecting the effect of the force due to the particle and fluid acceleration. This is for instance the case of a 1-D flow that has reached steady-state, so that the time variation of the particle velocity magnitude and direction is negligible. For simplicity we consider the body force is a constant in the equilibrium equation. Relevant examples are particle settling in a gravitational field, for which $a=-g$, or centrifugal settling at angular frequency ω, for which $a = \omega X_0^2$, where the coordinate X_0 is a characteristic radius of the centrifuge [4-5]. Finally, also in this case we make the assumption of small Reynolds, so that the drag coefficient is given by Eq. AIII.2. In this case the equation for the particle motion AIII.9 can be written in the following form

$$0 \approx \frac{18\mu}{D^2}(U - X') + a(\rho_p - \rho_f) \tag{AIII.25}$$

and the analytical solution for the slip velocity is straightforward

$$|U - X'| = a\frac{|\rho_p - \rho_f|}{\rho_p}\frac{\rho_p D^2}{18\mu} = a\frac{|\rho_p - \rho_f|}{\rho_p}\tau_0 \tag{AIII.26}$$

As evident from Eq. AIII.26, the slip velocity due to particle settling in the acceleration field is larger at increasing difference between particle and fluid density. This effect is minimized matching the two densities so that particles become buoyancy neutral.

1.3.1.3 Summary of relevant expressions for particle dynamics

The most relevant expressions necessary to choose the seed particles based on slip velocity considerations are summarized below [78].

Relaxation time for slip velocity (comparable particle and fluid density):

$$\tau_{slip} = \left(1 + \frac{1}{2}\frac{\rho_f}{\rho_p}\right)\frac{D^2 \rho_p}{18\mu} \qquad \text{(AIII.12-bis)}$$

Relaxation time for slip velocity (negligible fluid density):

$$\tau_0 = \frac{D^2 \rho_p}{18\mu} \qquad \text{(AIII.12a-bis)}$$

Relative velocity error for oscillating flow at angular frequency ω (negligible fluid density and body forces):

$$\varepsilon = 1 - \frac{1}{\sqrt{1 + \omega^2 \tau_0^2}} = 1 - \frac{1}{\sqrt{1 + (2\pi f)^2 \tau_0^2}} \qquad \text{(AIII.24-bis)}$$

Phase error between particle and fluid oscillation (negligible fluid density and body forces):

$$tg(\phi) = -\omega \tau_0 = -2\pi f \tau_0 \qquad \text{(AIII.23-bis)}$$

Critical (maximum) frequency tracked by a particle of given relaxation time and for specified relative velocity error (negligible fluid density and body forces):

$$f_c = \frac{1}{2\pi\tau_0}\sqrt{\frac{1}{(1-\varepsilon)^2} - 1} \qquad \text{(AIII.24a-bis)}$$

Critical (maximum) diameter of a particle that tracks the critical frequency with specified relative velocity error (negligible fluid density and body forces):

$$D_c = \sqrt{\frac{1}{2\pi}\frac{18\mu}{\rho_p f_c}\sqrt{\frac{1}{(1-\varepsilon)^2} - 1}} \qquad \text{(AIII.24b-bis)}$$

Time needed to track a constant fluid velocity with a given relative velocity error, for particles injected at rest in the flow (negligible body forces):

$$t_c = -\ln(\varepsilon)\tau_{slip} \qquad \text{(AIII.24d-bis)}$$

Travel length needed to reach the desired tracking accuracy (negligible body forces):

$$L_c = -\ln(\varepsilon)\tau_{slip}U_0 \qquad \text{(AIII.24e-bis)}$$

Settling speed in an acceleration field (negligible inertial forces):

$$\left|U - X'\right| = a\frac{\left|\rho_p - \rho_f\right|}{\rho_p}\tau_0 \qquad \text{(AIII.26-bis)}$$

BIOGRAPHICAL SUMMARY

Christine Darve was born in Chambery (France). She is a cryogenic engineer at the Fermi National Accelerator Laboratory (Illinois, USA) and will start her new assignment in November 2011 with the European Spallation Source (Lund, Sweden). She received her diploma in "Thermo-Mechanics of Systems and Materials" from the "Institut Polytechnique de Sevenans" (UTBM), France in 1996 and she has completed a PhD degree at Northwestern University, Evanston.

She has obtained a fellowship at the European Laboratory for Nuclear Research (CERN) from 1996-1999. She left CERN to become a staff member at the Fermi National Accelerator Laboratory (Fermilab), where she has been working at the forefront of thermal measurement developments and analysis of accelerator components and utilities. At Fermilab, she has participated in the design, installation and commissioning of the cryogenic activities related to the Large Hadron Collider (LHC) cryo-magnets, the liquid hydrogen absorber for the prospective muon accelerator collider and currently for the superconducting Radio Frequency cavities R&D program for future linear colliders. In parallel to those activities, she has coordinated the Tevatron cryogenic operations and the new SRF test areas at Fermilab. From September 2007 to July 2010, she has supported the hardware commissioning of the LHC at CERN laboratory by being responsible for the cryogenic activities pertaining to the low-beta magnets systems.

Beyond her professional assignments, Christine Darve has been the main organizer of the first edition of the African School on Fundamental Physics and its Applications hold in South Africa in August 2010 (~100 participants including 65 MSc and PhD students). The mission of this biennial 3-weeks school is to build capacity in the Least Developed Countries and to increase proficiency in sciences.

She has been appointed in a sub-committee of the American Standard of Testing and Materials (ASTM - C16 Thermal Insulation). She is a member of the American Physical Society and African Physical Society. She has written more than 50 publications in engineering conference proceedings and scientific journals.

JOURNAL ARTICLES AND CONFERENCE PROCEEDINGS

[1] A Method for Numerical Simulations of Superfluid Helium - C. Darve, N. A. Patankar, L. Bottura, S. W. Van Sciver; Presented at the CEC 2011.

[2] SRF Cavity Testing Status and Operational Experience - B. Soyars et al; Presented at the CEC 2011.

[3] Dynamic PID loop control - L. Pei et al.; Presented at the CEC 2011.

[4] First High Power Pulsed Tests of a Dressed 325 MHz Superconducting Single Spoke Resonator at Fermilab – R.Leigh Madrak et al.; Submitted to PAC 2011.

[5] Cryogenic Safety Aspects of the Low-□ magnet systems at the Large Hadron Collider (LHC) - Darve C. Presented at the International Cryogenic Engineering Conference (ICEC) 2010.

[6] Instrumentation of the Low-□ magnet systems at the Large Hadron Collider (LHC) - Darve C., Balle C., Casas-Cubillos J., Perin A. and Vauthier N.; Presented at the ICEC 2010.

[7] Commissioning and First Operation of the Low-Beta and its Electrical Distribution Feed-boxes at the Large Hadron Collider (LHC) - C. Darve, S. Feher, J. Kerby, T. Peterson, R. Rabehl, C. Balle, J. Casas-Cubillos, S. Claudet, G. Ferlin, L. Metral, A. Perin, H. Prin, N. Vauthier, U. Wagner and R. van Weelderen; Presented at the CEC 2009.

[8] Commissioning and First Operation of Superconducting Links at the Large Hadron Collider (LHC) - T. Goiffon, A. Perin, R. van Weelderen, C. Darve, R.S. Doohan and R.S. Sharma; Presented at the CEC 2009.

[9] Commissioning of the cryogenics of the LHC Long Straight Sections - J. Casas-Cubillos, S. Claudet, C. Darve, G. Ferlin, F. Millet, C. Parente, A. Perin, R. Rabehl, M. Soubiran, R. van Weelderen and U. Wagner; Presented at the CEC 2009.

[10] Commissioning of the low-beta Triplets of the Large Hadron Collider – J. Kerby, C. Darve, S. Feher and R. Ostojic; Applied Superconductivity Conference (ASC 2008).

[11] A method for the three-dimensional numerical simulation of Superfluid Helium – L. Bottura, C. Darve, N.A. Patankar and S.W. Van Sciver; Presented at the international Low Temperature Physics conference (LT25) 2008.

[12] A 3-D model of superfluid helium suitable for numerical analysis - C. Darve, N.A. Patankar and S.W. Van Sciver; Presented at ICEC 2008.

[13] Superconducting Radio-Frequency Modules Test Facility Operating Experience - W. Soyars, A. Klebaner R. Bossert, C. Darve, B. Degraff, A. Martinez, L. Pei and J. Theilacker; Presented at Cryogenic Engineering Conference (CEC/ICMC) 2007; Published in AIP Conf.Proc.985:127-134,2008 and Advances in Cryogenic Engineering 51B, pp. 1060-1068– AIP ISBN 0-7354-031.

[14] Cryogenics for the MuCool Test Area (MTA) - C. Darve, B. Norris and L. Pei; Presented at COOL'05; Published in AIP Conf.Proc.821:448-452,2006 and Eagle Ridge 2005, Beam cooling and related topics 448-452; AIP ISBN 0-7354-0314-7; fermilab-conf-05-468-ad.

[15] *An Update for the MuCool Test Area – A. Bross, M.A. Cummings, C. Darve, S. Ishimoto, A. Klebaner, A. Martinez, B. Norris and L. Pei; Presented at CEC/ICMC 2005; Published in AIP Conf.Proc.823:1060-1067,2006 and Adv. in Cryo. Eng. 51B, pp. 1060-1068– AIP ISBN 0-7354-0317-1.*

[16] *Design, Fabrication, and Test of an SRF Cryomodule Prototype at Fermilab – W. Soyars, C. Darve, T. Nicol and A. Rowe; CEC/ICMC 2005; Published in AIP Conf.Proc.823:1172-1178,2006 and Adv. in Cryo. Eng. 51B, pp. 1172-1180– AIP ISBN 0-7354-0317-1; fermilab-conf-05-638-ad.*

[17] *Convection-Type LH2 Absorber R&D for Muon Ionization Cooling – S. Ishimoto et al.; NUFACT'01; Published in Nucl.Instrum.Meth.A503:396-400,2003.*

[18] *The Liquid Hydrogen System for the MuCool Test Area - C. Darve et al.; Presented at CEC/ICMC 2003; Published in AIP Conf.Proc.710:48-55,2004 and Adv. in Cryo. Eng. Vol. 49A, pp. 48-55– AIP ISBN 0-7354-0186-1; fermilab-conf-03-499-ad.*

[19] *Report on the First Photon Stop Cryogenic design Experiment – M. Geynisman, P. Bauer, R. Bossert, C. Darve, K. Ewald, A. Klebaner, P. Limon and A. Martinez; CEC/ICMC 2003 and published in Adv. in Cryo. Eng. 49A, pp.379-487– AIP ISBN 0-7354-0186-1;fermilab-conf-03-244-e.*

[20] *Recent progress in neutrino factory and muon collider research within the Muon Collaboration - M. M. Alsharo'a et al.; Published in Phys.Rev.ST Accel.Beams 6:081001, 2002; FERMILAB-PUB-02-149-E, JLAB-ACT-03-07. 103pp.*

[21] *Cryogenic design for a liquid hydrogen absorber system – C. Darve, D. Allspach, E. Black, M.A. Cummings, C. Johnstone, D Kaplan., A. Klebaner, A. Martinez, B. Norris and M. Popovic; Presented at ICEC19, 2002; Published in the ICEC19 Proceeding, pp. 593-596; AIP ISBN 81-7319-508-0.*

[22] *Performance characterization of perforated multilayer insulation blankets – J. Fesmire, S. Augustynowicz and C. Darve; ICEC19; Published in the ICEC19 Proceeding, pp. 843-846, 2002-AIP ISBN 81-7319-508-0.*

[23] *Current LH2-Absorber R&D in MuCool– M. Cummings et al.; Presented at NUFACT'02; Published in J.Phys.G29:1689-1692, 2003.*

[24] *Synchrotron Radiation Absorbers for Hadron Colliders - P. Bauer et al.; Presented at EPAC 2002.- (06/2002); Published in Paris 2002, EPAC 02 2541-2543.*

[25] *Status of Neutrino Factory and Muon Collider Research and Development and Future Plans– PACS number 13.10– (02/2002).*

[26] *LHC Interaction Region Quadrupole Cryostat Design and Fabrication - T. Nicol et al; Presented at Magnet Technology 17; Published in the MT17 Proceeding- CERN - (09/2001).*

[27] *Synchrotron Radiation Issues in Future Large Hardron Colliders - P. Bauer, C. Darve and I. Terechkine; Presented at SNOWMASS 2001; Published in the Proceedings of APS / DPF / DPB Summer Study on the Future of Particle Physics (Snowmass 2001), Snowmass, Colorado, 30 Jun - 21 Jul 2001, pp T203.1; fermilab-conf-01-434.*

[28] *Progress in Energy Absorber R&D 2: windows - D. Kaplan et al.; PAC 2001; Published in IIT-HEP-01-2, PAC-2001-FPAH090, Aug 2001. 3pp. PAC 2001 Proceeding - Chicago – (06/2001); fermilab-conf-01-461.*

[29] *Progress in Absorber R&D for Muon Cooling- D. Kaplan et al.; IIT-HEP-01/1; Published in Nucl.Instrum.Meth.A503:392-395,2003; fermilab-conf-01-462.*

[30] *Failure Metrology using Projected target Videogrammetry – J. Greenwood, C. Darve, R. Bernstein and E. Black; CMSC 2001; Published in the Proceeding of the Coordinate Measurement Systems Committee (CMSC) conference in Albuquerque.*

[31] *He II Heat Exchanger Test Unit for the LHC Inner Triplet - C. Darve, E. Blanco, Y. Huang, T. Nicol, T. Peterson and R. van Weelderen; Presented at CEC/ICMC 2001; Published in AIP Conf.Proc.613:147-154,2002. Also in Adv. in Cryo. Eng. 47A, pp. 147-154– AIP ISBN 0-7354-0059-8; CERN-LHC-PROJECT-REPORT-505; fermilab-conf-01-488-ad.*

[32] *LHC Interaction Region Quadrupole Cryostat Design - T. Nicol, C. Darve, Y. Huang and T. Page CEC/ICMC 2001; Published in AIP Conf.Proc.613:391-398,2002.and in Adv. in Cryo. Eng. 47A, pp. 391-398– AIP ISBN 0-7354-0059-8.*

[33] *Synchrotron Radiation issues in the VLHC – P. Bauer, C. Darve, P. Limon, N. Solyak, I. Terechkine, M. Pivi, W.C. Turner and S. Sharma; Presented at PAC 2001; Published in PAC 2001 Proceeding - Chicago – (7/ 2001); fermilab-conf-01-113.*

[34] *Measurements of temperature on LHC thermal models - C. Darve and J. Casas; Presented at Conf: US-Japan workshop at NHMFL" Innovative Measurement Techniques in Cryogenics" - Published in Cryogenics vol. 41:319-326,2001.*

[35] *Experimental Investigations of He II Heat Transfer through a Short Section of LHC Inner Triplet Quadrupole Heat Exchanger- Ch. Darve, Y. Huang, T. H. Nicol and T. J. Peterson; Presented at the Applied Superconductivity Conference 2000; Published in IEEE Trans. Appl. Supercond. 2000; Vol. 11. pp. 1629; FERMILAB-TD-00-066.*

[36] *Status of the LHC Inner Triplet Quadrupole Program at Fermilab- J. Kerby et al.; Presented at ASC 2000; Published in the ASC 2000 proceeding, Virginia Beach, USA - FERMILAB-TD-00-065.*

[37] *A HE II heat exchanger test unit designed for the LHC interaction region magnets – C. Darve; Y. Huang; J. Kerby; T. Nicol and T. Peterson; Presented at CEC/ICMC 1999; Published in Adv.Cryog.Eng.45B:977-984, 2000.*

[38] *Thermal performance of insulating cryogenic pin spacers – C. Darve and G. Vandoni; Presented at ICEC17; proceeding of the 17th International Cryogenic Engineering Conference, Bournemouth, UK; 14 - 17Jul 1998; LHC-Project-Report-220.*

[39] Report on the First Photon Stop Cryogenic design Experiment – P. Bauer et al. .– (05/2003); FERMILAB TD-03-021.

[40] Concept of the first VLHC photon stop cryogenic design experiment - P. Bauer et al. – (05/2002); FERMILAB-TD-02-17.

[41] Design study for a staged very large hadron collider – G. Ambrosio et al.; SLAC-R-591, FERMILAB-TM-2149, Jun 2001 pp. 271.

[42] LHC IRQ Cryostat Slide Material - Test Report - C. Darve, Y. Huang, J Legner, T. Nicol, T. Wokas and G. Zielbauer – (06/2001); FERMILAB-TD-01-060.

[43] Preliminary design of the magnets for the muon cooling channel- V. Balbekov, E. Black, C. Darve, D. Elvira and J-M Rey - (06/2001); MUC-NOTE-COOL_EXP-0216.

[44] Design study for a staged Very Large Hadron Collider - Chapters 6_2_2 and 6_2_3 (06/2001); FERMILAB-TM-2149.

[45] VLHC Thermal shield Cooling – C.Darve, P.Bauer, and T.Nicol (05/2001);FERMILAB-TD-01-035.

[46] A photon stop for the VLHC2 Engineering design - Part 1- P. Bauer, K. Ewald, C. Darve, P. Limon, J.M. Rey, I. Terechkine and L. Imbasciati (04/2001); FERMILAB-TD-01-023.

[47] VLHC Beam Screen Cooling– C.Darve, P.Bauer, and P.Limon (02/2001); FERMILAB-TD-01-005.

[48] He II Heat Transfer through a Corrugated Tube - Test report - C. Darve; Y. Huang; T. Nicol, and T. Peterson - (11/1999); FERMILAB-TD-99-064.

[49] Heat Flow Measurements on Beam Screens with and without Supports – D. Bozzini; P. Cruikshank; C. Darve; B. Jenninger; N.Kos and D.Willems - (09/1999); LHC-PROJECT-NOTE-200.

[50] LHC IRQ Cryostat support mechanical performance – C. Darve; T.Nicol - (09/1999); FERMILAB-TM-2093.

[51] Very Large Hadron Collider Beam Screen Design Preliminary Investigation of Space Requirements- P. Bauer; C. Darve; T. Peterson and B. Jenninger - (07/1999); FERMILAB-TD-99-032; fermilab-vlhcpub-177.

[52] CTM3, the latest evolution of the cryostat thermal model: thermal performance measurements of the first run from March to May 1998 - C. Darve; A. Poncet and D. Willems - (03/99); LHC-CRI Technical Note 98-19.

[53] Mesure des pertes thermiques nominales du CTM – C. Darve - (11/1998); LHC-CRI TN 98-15.

[54] Influence de la couche extérieure de protection (Vitrulan) sur les matelas de superisolation - V. Benda; C. Darve and T. Wikberg - (12/1997); CERN Technical Note 97-07.

[55] Thermal performance measurements for a 10 meter LHC dipole prototype (Cryostat Thermal Model 2) - C. Darve; G. Ferlin; M. Gautier and L. R. Williams; LHC-Project-Note-112.

SOME PRESS CLIPPINGS

- *"The First African School on Fundamental Physics and its Applications (ASP2010)", by C. Darve, Forum on International Physics Newsletter March 2011, American Physical Society.*
- *"Into Africa – a school in fundamental physics. Students discover fundamental physics and its applications in Stellenbosch", (CERN Courier – feature of the November 2010 edition).*
- *"First African School of Physics empowers students" (Fermilab Today – August 2010).*
- *"The Rainbow School of Physics" (CERN Bulletin – August '10) + Press Release (July 2010).*
- *"The African School of Physics" (CERN Bulletin, May 2010).*
- *"LHC Reawakens,Sending Proton Beams Running at the Speed of Light" (Popular Science, Oct. 2009).*
- *"Women in Cryogenics and Superconductivity" (Cold Facts - Winter 2007).*
- *"LHC Magnets: From model to prototype" (FermiNews - October 2000).*
- *"International Collaboration" (CERN Courier - June 2000).*
- *"First hardware from the US-LHC collaboration comes to CERN" (CERN bulletin - April 2000).*
- *"Back to the future" (FermiNews - September 1999).*
- *Physique-sans-frontieres – Sarajevo, "The www: A window to Sciences and Technology" (ARTE TV show - December 1998).*